# HARNESSING THE PHYSICAL PROPERTIES OF ZNO NANOPARTICLES FOR BIOLOGICAL APPLICATIONS AND FACTORS THAT IMPACT ZNO NANOPARTICLE TOXICITY

by

Joshua Eixenberger

A dissertation

submitted in partial fulfillment

of the requirements for the degree of

Doctor of Philosophy in Biomolecular Sciences

Boise State University

December 2018

BOISE STATE UNIVERSITY GRADUATE COLLEGE

# DEFENSE COMMITTEE AND FINAL READING APPROVALS

of the dissertation submitted by

Joshua Eixenberger

Dissertation Title: Harnessing the Physical Properties of ZnO Nanoparticles for Biological Applications and Factors that Impact ZnO Nanoparticle Toxicity

Date of Final Oral Examination: 29 November 2018

The following individuals read and discussed the dissertation submitted by student Joshua Eixenberger, and they evaluated his presentation and response to questions during the final oral examination. They found that the student passed the final oral examination.

| | |
|---|---|
| Denise G. Wingett, Ph.D. | Chair, Supervisory Committee |
| Daniel Fologea, Ph.D. | Member, Supervisory Committee |
| Dmitri Tenne, Ph.D. | Member, Supervisory Committee |
| Juliette Tinker, Ph.D. | Member, Supervisory Committee |

The final reading approval of the dissertation was granted by Denise G. Wingett, Ph.D., Chair of the Supervisory Committee. The dissertation was approved by the Graduate College.

# DEDICATION

I dedicate this in memory of the two-special people that I lost during my PhD endeavor. Dr. Alex Punnoose was a great teacher, amazing scientist and exceptional mentor. He provided me with my first opportunity to conduct research and I would not be where I am today without him. My father-in-law Patrick Gibbons was a good friend, a loving grandfather and always showed the highest interest in my research. Both of you will be missed and my life is better from having shared it with you.

ACKNOWLEDGEMENTS

There are so many people that gave me their support and encouragement during this undertaking. I would first like to thank Dr. Alex Punnose for the years of experience and mentoring he provide to me. He was an amazing scientist and I really appreciate the opportunity to have worked with him over the years. I would like to thank Dr. Denise Wingett for her time, dedication and for putting up with my banter. We have been through a lot over the last few years and I appreciate her efforts. Dr. Daniel Fologea has always been around to field my numerous questions and to take the time to listen to my unending list of ideas. I really appreciate the time and support you gave me, especially with the number of students you are always juggling. I would also like to thank the last two members of my committee; Dr. Dmitri Tenne for the help in my research and the hours of teaching, Dr. Juliette Tinker for always putting up with my interruptions in her office and her time spent on this dissertation. I would also like to give a special thanks to Dr. Catherine Anders and Dr. Madhu Kongara for the hours of debate, venting, laughter and help with all my projects. I am glad you were part of the lab and having others to help me work on such an interesting and complex topic was more enjoyable with you there. To Beth Gee, I really appreciate all the hard work and dedication you provide to this program and especially with the support you personally gave me during my PhD. You are an essential part of this program and we all appreciate your dedication. I would also like to thank the Biomolecular Research Center for the years of support as a graduate

student and a special thanks to Raquel Brown for the countless hours she spent helping me with my projects and numerous hours of laughter.

To my friends and family, this journey would not have been possible without you. Tami you are a great mother, loving wife and most importantly you have been willing to put up with me over the years. Words cannot express how grateful I am for allowing me to pursue my passion and offering your continued support all these year. I love you more than you know and cherish every day we get to spend with each other. This journey would not have been possible without you by my side. Asher and Bryson, you are loud, stressful, mischievous but most importantly you bring joy to my life. I love you and I wouldn't trade the time we have together for anything. Dad, you are always there with your support and interest in my research. Mom, thank you for always telling me to not "waste my brain and do something with it". I really appreciate both of you and all the help and love you have given me over the years. To Teri and Pat, I really appreciate all the support you have given our family and I am truly happy to have been welcomed into your lives. To everyone else that has been with me through this endeavor, I am sorry for not personally acknowledging each of you that have offered their support over the years but there aren't enough words to express my gratitude to all.

ABSTRACT

The production of materials at the nanoscale leads to novel properties and has made the field of nanotechnology a part of everyday life. Numerous applications of nanomaterials have led to their use in electronics, optics, and medicine. However, creating materials at such a small size brings them on the same scale as many biomolecules and cellular components, altering their interactions with biological systems. This can lead to unintended biological impacts as many nanomaterials are considerably more toxic than their bulk counterpart material. ZnO nanoparticles (nZnO) are particularly interesting in this context. The FDA classifies ZnO as a generally recognized as safe substance, but numerous reports have demonstrated that they are inherently toxic when produced in the nanoscale. Much research has been conducted on understanding what makes them toxic in order to modify their properties for specific applications. While this would seem to impede their commercial use, many of the properties that make nZnO toxic have been exploited for the treatment of various diseases.

A wealth of knowledge has been generated about the physicochemical properties of nZnO that contribute to their toxicity, yet controversy remains about the toxicity mechanism. Numerous factors contribute to the toxicity of nZnO and the mechanism can vary greatly between cell types and the properties of the nanoparticles (NPs) under study. Even with all the data available, more work is needed to understand the complex interplay of nZnO with cells to fully exploit their commercial use and development as a potential therapeutic. In this regard, studies described in this dissertation were conducted

to help further the understanding of what aspects contribute to the cytotoxicity of nZnO and how different properties of the material can be utilized for biological applications.

The first chapter demonstrates that biological buffers can significantly impact the dissolution property of nZnO and may influence the conclusions that have been drawn from previously reported studies. All the biological buffers tested, including HEPES and MOPS that are routinely utilized in cellular media and biological imaging solutions, induced the rapid dissolution of nZnO. This observation extended to other experiments that demonstrate the inclusion of biological buffers in commonly used RPMI media, impacted the conversion of nZnO to other chemical species and altered its structural morphology. As dissolution has been implicated as one of the primary sources of nZnO toxicity, cellular viability experiments were conducted and the inclusion of HEPES in the media was found to significantly increase the toxicity of nZnO towards leukemic Jurkat T cells. These results highlight the fact that environmental factors need to be carefully considered when assessing the toxicity of nZnO.

Ion channels are critical to a cell's ability to maintain homeostasis and are imperative for the correct functionality of many cells. Therefore, the second chapter focused on what effects nZnO may have on transmembrane transport. For these assessments, lysenin, a pore forming toxin that mimics ions channels with respect to ionic transport and regulation, was utilized to investigate potential interactions of protein channels with nZnO. The conductance of lysenin was greatly diminished in the presence of nZnO and is believed to depend on electrostatic interactions. Lysenin's conductance can be inhibited from zinc ions, but the dissolution of nZnO was ruled out as being responsible for the modulation of the transport capabilities of the protein. We concluded

that the positively charged nZnO interacts with negative residues within lysenin to alter the conductance and these observations may translate to a potential contributor to the cytotoxicity of nZnO.

Many of the assessments on nZnO toxicity have relied on end-point observations. This is due, in part, to the fact that their small size makes it extremely difficult to track their interplay with cells in real-time and fluorescent labeling of the NPs may alter how unmodified nZnO interacts with cells. Direct fluorescence imaging of the NPs could substantially help in tracking the complex interactions of nZnO with cells. However, the band gap of nZnO is 3.37 eV which correlates to 368 nm and therefore requires the use of UV excitation sources to generate photo emissions. Unfortunately, UV excitation sources and detectors are generally absent in most conventional fluorescence microscopes making this approach difficult. The third study of this project sought to modulate certain physical properties of nZnO to create a way to fluorescently track the NPs in living cells without changing the composition of the material. To achieve this goal, a systematic control of defects in the crystal of nZnO was carried out to alter its properties. By producing a relatively high number of defects in nZnO, the band gap of the material was lowered to ~3.1 eV (400 nm) and produced a narrow emission in the visible spectra, with a peak at 425 nm. These changes allowed for the use of a 405 nm laser, generally available on fluorescent microscopes, to image the nZnO with confocal microscopy. Initial live-cell imaging experiments were conducted to demonstrate the feasibility of utilizing these new nZnO to track their interactions with cells.

The final piece of this dissertation sought to utilize the ability of nZnO to generate ROS when photo irradiated for a new drug delivery platform. Towards this end, the nZnO

were encapsulated within a lipid coating and in vitro studies demonstrated that the encapsulation of the NPs essentially removed the toxicity at concentrations up to 10 times the $IC_{50}$ of bare nZnO. This feature could be extremely helpful in preventing off-target effects when treating patients with nZnO but requires reestablishing the toxicity when the NPs reach the cancerous environments. To this end, the cancer cells that were treated with the encapsulated nZnO were exposed to irradiation and the cytotoxicity of the NPs was restored. To further expand upon this strategy, a fluorescent dye was co-encapsulated with the nZnO to simulate hydrophilic drug loading and allow for evaluations on the ability to trigger the release of the dye. Studies on the release kinetics demonstrated a rapid release of the dye upon irradiation and gave insights into optimizing the encapsulation of the NPs. To demonstrate that this strategy is not just a novelty of fluorescent dyes, the hydrophobic chemotherapy drug Paclitaxel was co-encapsulated with nZnO. Both Jurkat T cell leukemia and T47D breast cancer cells were treated with the co-encapsulated nZnO and Paclitaxel. In both cases, the triggered release groups showed improved toxicity towards the cells with the most pronounced difference noted for the breast cancer cells. Taken together, the cumulation of this dissertation helps further the progress in understanding the cytotoxicity of nZnO, offers a new way to study the interactions of essentially pure nZnO with cells and provides a novel strategy for the use of nZnO as a therapeutic and potential diagnostic tool.

TABLE OF CONTENTS

LIST OF TABLES

LIST OF FIGURES

# LIST OF ABBREVIATIONS

| | |
|---|---|
| Aso | Asolectine |
| BLM | Bilayer Lipid Membrane |
| Chol | cholesterol |
| CPS | counts per second |
| CT | computed tomography |
| DEG | diethylene glycol |
| DI | deionized |
| DiPhytPC | diphytanoyl phosphatidylcholine |
| DLS | dynamic light scattering |
| DMEM | RPMI |
| EDTA | Ethylenediaminetetraacetic acid |
| FBS | fetal bovine serum |
| FITC | fluorescein isothiocyanate |
| FT-IR/FTIR | Fourier transformed infrared spectroscopy |
| HDS | hydrodynamic size |
| HEPES | 4-(2-hydroxyethyl)-1piperazineethanesulfonic acid |
| ICP-MS | inductively coupled plasma mass spectrometry |
| MOPS | 3-(N-morpholino)propanesulfonic acid |
| MRI | magnetic resonance imaging |
| NMs | Nanomaterials |

| | |
|---|---|
| NPs | Nanoparticles |
| nZnO | Zinc Oxide Nanoparticles |
| PBS | phosphate-buffered saline |
| PIPES | piperazine-N,N′-bis(2-ethanesulfonic acid) |
| PL | Photoluminescence |
| PPH free | phenol red, phosphate, and HEPES free |
| PTFE | polytetrafluoroethylene |
| PVP | polyvinylpyrrolidine |
| ROS | Reactive Oxygen Species |
| SM | sphingomyelin |
| TEM | transmission electron microscopy |
| TGA | Thermogravimetric Analysis |
| UV | ultraviolet |
| w/w | weight to weight |
| XPS | X-ray photoelectron spectroscopy |
| XRD | X-ray diffraction |
| ZnAc | zinc acetate |
| ZP | zeta potential |

# CHAPTER ONE: INTRODUCTION

## Overview of Nanomaterials and ZnO

The field of nanotechnology is growing at an extraordinarily fast pace with industries and governments spending billions of dollars per year in basic research and development. Producing materials in the nanoscale (0-100 nm) creates novel properties that are not observed in bulk (micron sized or larger) material of identical composition. The changes in the material properties can be largely attributed to the small size, where a relatively large fraction of the atoms comprise the surface compared with the atoms found within the volume of the material. Not only do new properties emerge, but the reduction of the material size brings them on the same scale as many cellular components and biomolecules. These features alter the material's interactions within biological systems and have been exploited for numerous applications.

ZnO nanoparticles (nZnO), in particular, are mass produced and used worldwide with an estimated market valued at $2.099 billion in 2015 with an expected market value of $7.677 billion by 2022.[1] The novel properties of nZnO have led to their use in cosmetics, electronics, an anti-bacterial and anti-fungal agents, as well as a potential cancer therapeutic.[2-8] While their production at the nanoscale offers much promise in numerous fields, there is also concern about their unintended biological impacts. The FDA classifies ZnO as a generally recognized as safe substance, but when produced in the nanoscale, many reports have demonstrated a relatively high toxicity towards various cell types.[9-12] This underscores the reason why many researchers have sought to

understand what makes nZnO toxic with the hopes of tailoring its properties to reduce its toxicity or manipulate these features for the treatment of various infections and diseases.

## Toxicity Mechanisms of nZnO

The inherent cytotoxicity of nZnO has been studied with numerous cell types including mammalian primary and cancer cells, bacteria and fungi.[5, 13-16] Studies have extended to *in vivo* systems in various mammals, zebra fish and crustaceans.[17-20] Even though numerous reports on nZnO toxicity have been published, the mechanism(s) of toxicity still remains controversial. There are two mechanisms that have been identified as the important sources of toxicity; reactive oxygen species (ROS) generation and dissolution of the nanoparticle.

Dissolution of nZnO results in the release of ionic zinc, which can disrupt homeostasis and eventually lead to cell death.[21, 22] Even within this context there is controversy in regards to how dissolution leads to cytotoxicity. One proposed route is that large amounts of ionic zinc are released in the extracellular environment and are then internalized by the cells. This can occur through zinc specific transporters called the ZIP (SLC39) family, via non-specific ion transporters, or through endocytosis.[23-25] For example, Johnson et al. demonstrated that up to 37% of available zinc from the nZnO under study was released after suspension in the cellular media DMEM.[26] Treatment of the cells with the NP suspension induced cell death and the authors concluded that uptake of extracellular zinc ions was responsible for the toxicity. This was supported by two different experiments. Pre-treatment with EDTA, a known zinc chelator, abolished the toxicity, and treatment with levels of $CaCl_2$ that inhibit calcium channels, which are partially responsible for zinc uptake, reduced the toxicity of nZnO.

In contrast, other researchers have proposed that the large increases of intracellular zinc stem from endocytosis or passive transport of nZnO into the cell. Once internalized, the nZnO that passively entered can shed the zinc ions within the cytoplasm directly. For the endocytic route, the endocytosed vesicles fuse with lysosomes, which contain a low pH, and rapidly dissolve the nZnO which subsequently releases the free zinc ions within the cell. A report on nZnO interactions with human colon carcinoma cells showed extensive nanoparticle entry into the cells after just one hour.[27] The entry of the nZnO was believed to be from both passive entry and endocytosis. After the first hour, the number of nanoparticles inside the cells apparently decreased. However, a complementary study showed that the levels of free zinc inside the cells correlated well with the decrease in the number of intact nZnO from a sustained dissolution process. Similarly, a report that treated human bronchial epithelial cells with nZnO showed high levels of intracellular ionic zinc but the large concentrations of ionic zinc were recorded after just one hour.[28] To try to determine how the intracellular zinc entered the cell, they treated the same cells with nZnO doped with iron, as it had a much slower dissolution rate. From the slower dissolution rate, they were able to track that the doped nZnO were internalized into the cells and concluded the undoped nZnO internalized first, but rapidly dissolved to cause the increased ionic zinc concentrations.

Regardless of how zinc ions enter the cell, disruption of zinc homeostasis can quickly lead to cellular death. Chevallet et al. investigated how human liver-derived cells (HepG2) responded to treatment with nZnO and zinc acetate.[29] At non-lethal doses, the cells tried to regulate the influx of zinc ions through large increases in Metallothionein 1X, a protein that chelates zinc ions to combat metal toxicity, and Znt1, a protein

responsible for the efflux of zinc from the plasma membrane. The authors provided evidence that the cells transport and store the excess zinc in the mitochondria. At critical levels, the excess zinc leads to mitochondrial injury and can eventually lead to the triggering of apoptosis.

The other strongly argued mechanism of toxicity is due to the generation of ROS, although some controversy regarding the precise mechanism of ROS generation remains. Some argue that the dissolution process of nZnO triggers apoptosis, as discussed above, that in turn creates the heightened levels of ROS found within the cell. Supporting evidence for this model utilized the mouse macrophage Ana-1. The authors measured the amount of free zinc ions in the media and concluded that the zinc ions were responsible for the observed increases in ROS levels due to the cytotoxic response.[30] Shen et al. similarly concluded that ROS generation was a consequence of high intracellular ionic zinc levels but that this only occurred after nanoparticle entry into the cell.[31] While there is certainly evidence that points to this route of ROS generation, other researchers have demonstrated that nZnO can produce ROS intrinsically.

The inherent ability of nZnO to produce ROS is related to the band structure of the material. The valence band is the highest energy level that an electron occupies when bound to the material. In metals, the valence band overlaps with the conduction band allowing electrons to act as free charge carriers. For semiconductors such as ZnO, the minimum energy required to excite an electron from the valence band to the conduction band is termed the band gap. When enough energy is supplied to the electron, it can move into the conduction band and becomes a “free” electron. However, the free electron can become bound to the hole left in the valence band and these electron hole-pairs are

termed excitons. Due to the small size of nZnO and surface defects, a relatively large number of excited electrons and excitons can be stabilized in the material.[32, 33] The conduction band electrons and valence band holes are proposed to be responsible for the ability of nZnO to catalyze the production of ROS.

The ability to intrinsically produce ROS stems from two different processes.[34] The excited conduction band electrons are thought to react with adsorbed $O_2$ molecules and form superoxide anions. The holes left in the valence band react with locally adsorbed $OH^-$ ions to produce hydroxyl radicals. In the context of cytotoxicity, superoxide anions ($O_2^-$) can then be converted by the enzyme superoxide dismutase to form hydrogen peroxide. Due to the stabilization of excitons from the small size of the particles, nZnO can catalyze ROS production leading to cytotoxic effects. These ROS generating capabilities of nZnO are further enhanced by irradiation with UV light, as it provides more energy than the band gap of the material.[34] Photoirradiation excites the valence band electrons into the conduction band, thus rapidly accelerating the intrinsic ROS production of the nanoparticles.

Dissolution and ROS production from nZnO are considered two of the primary mechanisms of nZnO cytotoxicity. As previously discussed, there are obviously conflicting reports about the toxicity mechanism of nZnO and even within the context of a specific mechanism, there is no clear consensus. These mechanisms are not necessarily independent and are all likely to contribute to the interactions of nZnO with cells. A recent report investigated how variously synthesized nZnO generated different toxicity profiles.[35] Many key physical properties of the nanoparticles were similar such as crystal size, band gap and lattice parameters but other factors such as hydrodynamic size,

dissolution potential and ROS generation were different. This report highlights that even though the same material, nZnO, is utilized in the various studies, variations in the physicochemical properties impact the nZnO interactions with cells and may alter the toxicity mechanism.

## Factors that Impact Toxicity

With all the reports regarding nZnO toxicity, it has become apparent that the physicochemical properties of the material can impact nZnO interactions with cells. Making matters more complex is the fact that different cell lines will also interact with nZnO in unique ways. As discussed previously, even in the context of dissolution there remains controversy. Researchers utilizing RAW 246.7 macrophages, a phagocytic cell line, concluded the uptake of the nanoparticles is largely responsible,[36] and yet other researchers using non-phagocytic cell lines suggest that extracellular dissolution induces cell death.[29] While extreme differences between cell lines will impact interactions with nanoparticles, more basic cell growth characteristics have also been shown to impact cell viability.

Cho et al. demonstrated that sedimentation of nanoparticles impacts the uptake of the particles by cells.[37] The sedimentation of the NPs to the bottom of the cell culture well creates higher concentrations of the particles on the cell surface compared with the initial bulk concentration introduced into the media.[37] To illustrate this point for nZnO, a study was conducted that created a more stable dispersion of nZnO in media by first coating the particles with serum proteins.[38] When an adherent cell line was treated with the particles, the more stable suspension resulted in increased viability, presumably by reducing the amount of nanoparticles settling on top of the cells. In contrast, Jurkat T

cells, a suspension cell line, showed the opposite trend. The more stable solution increased the interaction of the nanoparticles with the suspended cells, thereby reducing the viability. This study demonstrates how other factors can influence the viability studies of nZnO and the coating of NPs with serum proteins highlights another factor that plays a role when determining nanoparticle toxicity.

One well known factor that alters nanoparticles in biological studies is the formation of a protein corona around the particles. Much work has been done to understand how biological media (e.g. plasma) interacts with nanoparticles. Studies have shown that regardless of the nanomaterial's bulk composition, the particle surface properties and size influence the corona formation.[39] The corona can be categorized into two sub-classes; the hard corona, comprised of biomolecules with a high affinity for the nanoparticle surface, and a soft corona that is made of molecules that rapidly exchange from the surface back into the media. This corona formation likely impacts the interaction of nanoparticles with cells, and depending on the attached biomolecules, may alter endocytic or passive transport mechanisms. As different cellular media compositions utilize various serum proteins, this fact also highlights the importance of the environment the study is being conducted in.

Not only do serum proteins interact with nanoparticles, but certain components in cellular media used for *in vitro* studies have also been shown to play a role. As nZnO are prone to dissolution, the zinc ions that are released interact with the carbonate in media, forming insoluble zinc carbonate species.[40] Phosphate is another common component in cellular media and varies in concentration between different media formulations. This is important as it has been shown to react with nZnO. Over time, phosphates induce the

transformation of crystalline ZnO to porous structures comprised of both crystalline and amorphous zinc oxide and zinc phosphate species.[41, 42] As these studies are more recent, only a few evaluations have considered how these new chemical species impact the toxicity of nZnO. Additionally, when drawing conclusions on the impact dissolution of nZnO has on the toxicity, the formation of insoluble precipitants from various concentrations of phosphates and carbonates impact the "free" zinc ion concentration in the extracellular environment. This fact may be a common reason why conflicting reports exist regarding the toxicity mechanism of nZnO. Taken together, it is apparent that the complex nature of deciphering the toxicity of nZnO needs to take into account the physicochemical properties of the nanoparticle and also how the various components in the study environment alter their interactions with various cell types.

## Bioimaging

Fluorescent and luminescent imaging have helped to produce a wealth of knowledge about cell structure, dynamic cellular processes and trafficking. The development of quantum dots, inorganic nanoparticles that are fluorescent due to changes in their physical properties, have emerged as an exciting new technology for bioimaging studies. When compared to traditional fluorescent organic dyes, quantum dots have many superior properties such as the ability to alter the excitation and emissions based on the crystal size, resistance to photobleaching, high fluorescent quantum yields and broad absorptions.[43, 44] Other properties such as large cross sections for two photon microscopy studies make them beneficial for specific types of studies.[43,44]

Many of the currently used quantum dots are semiconductors comprised of cadmium chalcogenides and are well known for the emission tuning through control of

their size and narrow emission spectra. Since quantum dots have many beneficial optical properties, they have been used for various imaging applications. However, numerous reports have also shown that they are highly toxic to cells, reportedly in the nanomolar range.[45] To overcome this limitation, numerous strategies have been employed to reduce their toxicity. The most common way to reduce the toxicity of quantum dots has been to coat their surface. However, in a review on quantum dot toxicity, some researchers have demonstrated that the coating significantly reduces the toxicity of the quantum dots, whereas others have contributed the toxicity to the coating material that was used to stabilize the particles in solution.[46] While these modifications have allowed for their use in imaging, researchers have sought out other less toxic semiconducting nanoparticles for use in bio-imaging.

ZnO nanoparticles have been regarded as a promising candidate for imaging. This is in part due to their low cost of manufacturing and relatively low toxicity compared to cadmium-based quantum dots. However, various challenges are present when trying to use nZnO for bio-imaging. Since the band gap of nZnO is ~3.37 eV, UV light is required to excite the nanoparticles and they generally emit light in the UV region (~370 nm) from near band edge emissions and a surface defect related broad green emission (500-700 nm). This broad green region has been targeted by researchers as it is in the visible spectrum but, unfortunately, its emission can overlap with various other fluorophores traditionally used in fluorescence imaging studies. On top of this, as discussed above, ZnO is prone to modifications when introduced into biological medial, such as formations of zinc phosphate/carbonate species that can quickly quench the fluorescence generated due to surface defects.

Many of these challenges have been overcome through various modifications of nZnO. These modifications include coating the nanoparticles with polymers, encapsulating fluorescent dyes within nZnO, or doping of various other metals into the crystal lattice.[47-49] While these approaches have created novel fluorescent particles, when trying to assess the toxicity mechanisms of nZnO, these modifications can alter the properties of the nanoparticles. Therefore, the conclusions drawn from these particles may not accurately reflect how unmodified nZnO interacts with cells.

In addition to fluorescence imaging, nZnO have been used for other bio-imaging applications such as MRI and CT scans.[48, 50] In order to accomplish this, one approach has been to dope nZnO with different lanthanides such as gadolinium as it has a relatively high number of unpaired electrons and most of the currently used MRI contrast agents are gadolinium based. Liu et al. demonstrated that Gd doped nZnO particles can fluorescently label HeLa cells and that $T_1$-weighted MR images of the same cells were significantly brighter and therefore have potential to be used as a MRI contrast agent.[48] Others have shown similar results when testing Gd doped nZnO for MRI purposes and have also assessed their ability as a possible CT contrast agent.[50] Since there have been recent concerns about side effects from more traditionally used contrast agents, nZnO holds promise as a viable alternative.

## nZnO as a Potential Therapeutic

The selective destruction of cancerous cells is the primary goal for cancer therapy. In this regard, nZnO are very promising. Numerous reports have not only demonstrated the toxicity of nZnO to cancer, but have shown high selectivity. For example, one report demonstrated that nZnO was 33-fold more toxic to Jurkat T cell leukemia than normal T

cells.[10] Others have shown the selectivity of nZnO for cancerous cells of the lungs, glioma, prostate, breast, blood, nasopharynx and cervix.[51-54] Not only has the selectivity of nZnO been demonstrated with multiple cancer cell lines, but importantly, the selectivity of nZnO has been demonstrated for cancers such as squamous cell lung cancer and pancreatic adenocarcinoma in mouse models.[17, 55]

The selective nature of nZnO is very interesting yet the specific reason for its high selectivity is still currently unclear. A proposed reasoning for this selectivity has to do with the fact that ROS is found at higher concentrations in cancerous cells.[56] When cancer cells are challenged with nZnO, the cells tends to generate more ROS than normal cells. The relatively lower amounts of ROS found in normal cells may allow for them to mitigate the increase in ROS production when exposed to nZnO and, therefore, protect them from the cytotoxic effects. Regardless if ROS production stems from nZnO directly or is a consequence of nZnO dissolution, this may be a possible explanation for why nZnO are selectively toxic to cancer.

The natural selective nature of nZnO makes it a promising candidate in the treatment of cancer by itself. However, many researchers have developed strategies to further utilize certain properties of nZnO and expand its use as a potential therapeutic option. As nZnO produce more ROS when irradiated with UV light, some have used this feature to enhance nZnO toxicity towards cancer cells. For example, Hackenberg et al. showed significant improvement in the ability of nZnO to kill human squamous cell carcinoma when irradiated with UVA-1 light at concentrations that didn't affect cell viability with no light exposure.[57] Others have also shown similar increases in toxicity of cancer cells when exposed to nZnO and irradiated.[58, 59] Another strategy has been to co-

treat drug resistant cancer cells with daunorubicin, nZnO, and expose them to UV irradiation. Guo et al. demonstrated synergistically enhanced toxicity of the drug and nanoparticles when exposed to photoirradiation.[60] To expand upon this even further, one group doped lanthanides into nZnO and demonstrated that instead of UV light, X-rays could be used to stimulate ROS production from nZnO.[50] Not only have the ROS generating capabilities of nZnO been utilized in the treatment of cancer, but others have taken advantage of the high dissolution potential of nZnO.

To utilize the dissolution of nZnO in the treatment of cancer, Manshian et al. optimized the dissolution potential of nZnO by doping iron into the particle.[17] They found that doping nZnO with 2% iron was the optimal concentration and caused selective cancer cell death both *in vitro* and in a mouse model. An entirely different strategy that took advantage of the dissolution potential of nZnO was to utilize it in a drug delivery platform. The chemotherapy drug doxorubicin was loaded in $SiO_2$ nanoparticles and then encapsulated with ZnO.[61] When exposed to lower pH environments, which is often found in many tumor microenvironments, the nano-ZnO layer rapidly dissolved and released the chemotherapy drug. The high dissolution of nZnO at a lower pH has also been used with porous nZnO as a means to deliver doxorubicin.[62] The porous nZnO allowed for higher drug loading capabilities and the particle was further modified by conjugation of folate to the surface to actively target breast cancer cells that over express this receptor. When the drug-loaded particle was exposed to a pH of 5, nearly double the amount of the drug was released at every evaluated time point when compared to the release profile at physiological pH (pH=7.4).

Collectively, the attributes of nZnO have many potential uses as a cancer therapeutic. With numerous physical properties that can be exploited for drug delivery applications coupled with the intrinsic cancer cell selectivity, there is exciting potential for nZnO to be used as a nanomedicine. Additionally, the potential to use nZnO for bio-imaging purposes may allow for the creation of novel strategies involving nZnO to treat patient's cancer while simultaneously monitoring tumor regression/progression.

## Future Directions

The controversy over the toxicity mechanism of nZnO highlights the need to understand what factors influence the cytotoxic effects. Numerous studies with different formulation of nZnO and various cell types make arriving at a single conclusion very difficult. Most likely, multiple modes of action are responsible for the toxicity of nZnO and is not limited to one factor. Obvious difference in the materials physicochemical properties, the properties of the cell line and the environment the nanoparticles are being studied in, can all influence the interactions of the particles with the cells.

Other more modest, yet potentially relevant factors may impact the dynamic behavior of nZnO within biological systems. To arrive at the point where we can reasonably predict how the nanoparticles will interact within a specific study would be an amazing accomplishment, yet, is highly unlikely to occur in the near future with such a complex system. However, understanding what factors may influence or alter their interactions is imperative to achieving the safe and effective use of nZnO for its multiple applications. To achieve these goals, more simplified systems that can isolate one aspect that influences the nanoparticle toxicity may help in arriving to a more thorough understanding. With the wealth of knowledge that has already been collected, many of

the factors that modulate the interactions of nZnO within biological systems have led to their use in numerous novel ways.

The various attributes of nZnO such as their cancer cell selectivity, low cost of manufacturing and multiple physical properties that can be harnessed for specific applications make this an interesting material to research and utilize. The overall goals of this dissertation sought to further the understanding and use of nZnO within biological systems. These objectives were to i) understand what factors within biological media can impact the observed toxicity of nZnO, ii) utilize a simplified model system to understand the interaction of nZnO with ion channels, iii) develop a way to use unmodified nZnO for bioimaging studies, and iv) to harness the physicochemical properties of nZnO to be used in a new therapeutic device. The first two objectives advance our understanding of the factors that influence the interactions of nZnO with cells and point to a potential new mechanism that contributes to the cytotoxicity of nZnO. The third objective can conceivably help in deciphering the complex interplay of nZnO with cells by providing a means to perform live cell imaging experiments to track the interactions in real-time. It may also further expand into other potential uses of nZnO, such as its use as a relatively safer bio-label than more traditionally used quantum dots. The last objective, sought to exploit the ROS generating properties of nZnO when irradiated to trigger the release of the nanoparticles and chemotherapeutic drugs. This system provides a potential new way to simultaneously expose cancer cells to nZnO and chemotherapeutics on demand, while reducing overall systemic toxicity. All of these studies help the progression of developing a more thorough understanding of the interplay of nZnO with cells and potentially further its use as a therapeutic option.

## References

1. Sahu, Y. S., Nano Zinc Oxide Market by Application (Paints & Coatings, Cosmetics, and Others) - Global Opportunity Analysis and Industry Forecast, 2014-2022. 09-28-2018 ed.; Research, A. M., Ed. 2016; pp https://www.alliedmarketresearch.com/nano-zinc-oxide-market.

2. Lu, P. J.; Huang, S. C.; Chen, Y. P.; Chiueh, L. C.; Shih, D. Y. C., Analysis of titanium dioxide and zinc oxide nanoparticles in cosmetics. Journal of Food and Drug Analysis 2015, 23 (3), 587-594.

3. Vidor, F. F.; Wirth, G. I.; Hilleringmann, U., Low temperature fabrication of a ZnO nanoparticle thin-film transistor suitable for flexible electronics. Microelectronics Reliability 2014, 54 (12), 2760-2765.

4. Feris, K.; Otto, C.; Tinker, J.; Wingett, D.; Punnoose, A.; Thurber, A.; Kongara, M.; Sabetian, M.; Quinn, B.; Hanna, C.; Pink, D., Electrostatic Interactions Affect Nanoparticle-Mediated Toxicity to Gram-Negative Bacterium Pseudomonas aeruginosa PAO1. Langmuir 2010, 26 (6), 4429-4436.

5. Xie, Y. P.; He, Y. P.; Irwin, P. L.; Jin, T.; Shi, X. M., Antibacterial Activity and Mechanism of Action of Zinc Oxide Nanoparticles against Campylobacter jejuni. Applied and Environmental Microbiology 2011, 77 (7), 2325-2331.

6. He, L. L.; Liu, Y.; Mustapha, A.; Lin, M. S., Antifungal activity of zinc oxide nanoparticles against Botrytis cinerea and Penicillium expansum. Microbiological Research 2011, 166 (3), 207-215.

7. Rasmussen, J. W.; Martinez, E.; Louka, P.; Wingettt, D. G., Zinc oxide nanoparticles for selective destruction of tumor cells and potential for drug delivery applications. Expert Opinion on Drug Delivery 2010, 7 (9), 1063-1077.

8. Djurisic, A. B.; Ng, A. M. C.; Chen, X. Y., ZnO nanostructures for optoelectronics: Material properties and device applications. Progress in Quantum Electronics 2010, 34 (4), 191-259.

9. Ng, C. T.; Yong, L. Q.; Hande, M. P.; Ong, C. N.; Yu, L. E.; Bay, B. H.; Baeg, G. H., Zinc oxide nanoparticles exhibit cytotoxicity and genotoxicity through oxidative stress responses in human lung fibroblasts and Drosophila melanogaster. International Journal of Nanomedicine 2017, 12, 1621-1637.

10. Hanley, C.; Layne, J.; Punnoose, A.; Reddy, K. M.; Coombs, I.; Coombs, A.; Feris, K.; Wingett, D., Preferential killing of cancer cells and activated human T cells using ZnO nanoparticles. Nanotechnology 2008, 19 (29), 10.

11. Xia, T.; Kovochich, M.; Liong, M.; Madler, L.; Gilbert, B.; Shi, H. B.; Yeh, J. I.; Zink, J. I.; Nel, A. E., Comparison of the Mechanism of Toxicity of Zinc Oxide and Cerium Oxide Nanoparticles Based on Dissolution and Oxidative Stress Properties. Acs Nano 2008, 2 (10), 2121-2134.

12. Sharma, V.; Anderson, D.; Dhawan, A., Zinc oxide nanoparticles induce oxidative DNA damage and ROS-triggered mitochondria mediated apoptosis in human liver cells (HepG2). Apoptosis 2012, 17 (8), 852-870.

13. Xu, X. L.; Chen, D.; Yi, Z. G.; Jiang, M.; Wang, L.; Zhou, Z. W.; Fan, X. M.; Wang, Y.; Hui, D., Antimicrobial Mechanism Based on H2O2 Generation at Oxygen Vacancies in ZnO Crystals. Langmuir 2013, 29 (18), 5573-5580.

14. Hanley, C.; Thurber, A.; Hanna, C.; Punnoose, A.; Zhang, J. H.; Wingett, D. G., The Influences of Cell Type and ZnO Nanoparticle Size on Immune Cell Cytotoxicity and Cytokine Induction. Nanoscale Research Letters 2009, 4 (12), 1409-1420.

15. Taccola, L.; Raffa, V.; Riggio, C.; Vittorio, O.; Iorio, M. C.; Vanacore, R.; Pietrabissa, A.; Cuschieri, A., Zinc oxide nanoparticles as selective killers of proliferating cells. International Journal of Nanomedicine 2011, 6, 12.

16. Arciniegas-Grijalba, P. A.; Patino-Portela, M. C.; Mosquera-Sanchez, L. P.; Guerrero-Vargas, J. A.; Rodriguez-Paez, J. E., ZnO nanoparticles (ZnO-NPs) and their antifungal activity against coffee fungus Erythricium salmonicolor. Applied Nanoscience 2017, 7 (5), 225-241.

17. Manshian, B. B.; Pokhrel, S.; Himmelreich, U.; Tamm, K.; Sikk, L.; Fernandez, A.; Rallo, R.; Tamm, T.; Madler, L.; Soenen, S. J., In Silico Design of Optimal

Dissolution Kinetics of Fe-Doped ZnO Nanoparticles Results in Cancer-Specific Toxicity in a Preclinical Rodent Model. Advanced Healthcare Materials 2017, 6 (9), 11.

18. Kteeba, S. M.; El-Adawi, H. I.; El-Rayis, O. A.; El-Ghobashy, A. E.; Schuld, J. L.; Svoboda, K. R.; Guo, L. D., Zinc oxide nanoparticle toxicity in embryonic zebrafish: Mitigation with different natural organic matter. Environmental Pollution 2017, 230, 1125-1140.

19. Heinlaan, M.; Ivask, A.; Blinova, I.; Dubourguier, H. C.; Kahru, A., Toxicity of nanosized and bulk ZnO, CuO and TiO2 to bacteria Vibrio fischeri and crustaceans Daphnia magna and Thamnocephalus platyurus. Chemosphere 2008, 71 (7), 1308-1316.

20. Vandebriel, R. J.; De Jong, W. H., A review of mammalian toxicity of ZnO nanoparticles. Nanotechnology, Science and Applications 2012, 5, 61-71.

21. Kao, Y. Y.; Chen, Y. C.; Cheng, T. J.; Chiung, Y. M.; Liu, P. S., Zinc Oxide Nanoparticles Interfere With Zinc Ion Homeostasis to Cause Cytotoxicity. Toxicological Sciences 2012, 125 (2), 462-472.

22. Bozym, R. A.; Chimienti, F.; Giblin, L. J.; Gross, G. W.; Korichneva, I.; Li, Y. A.; Libert, S.; Maret, W.; Parviz, M.; Frederickson, C. J.; Thompson, R. B., Free zinc ions outside a narrow concentration range are toxic to a variety of cells in vitro. Experimental Biology and Medicine 2010, 235 (6), 741-750.

23. Eide, D. J., Zinc transporters and the cellular trafficking of zinc. Biochimica Et Biophysica Acta-Molecular Cell Research 2006, 1763 (7), 711-722.

24. Gyulkhandanyan, A. V.; Lee, S. C.; Bikopoulos, G.; Dai, F. H.; Wheeler, M. B., The Zn2+-transporting pathways in pancreatic beta-cells - A role for the L-type voltage-gated Ca2+ channel. Journal of Biological Chemistry 2006, 281 (14), 9361-9372.

25. Liu, J.; Kang, Y.; Zheng, W.; Song, B.; Wei, L.; Chen, L.; Shao, L., From the Cover: Ion-Shedding Zinc Oxide Nanoparticles Induce Microglial BV2 Cell Proliferation

via the ERK and Akt Signaling Pathways. Toxicological Sciences 2017, 156 (1), 167-178.

26. Johnson, B. M.; Fraietta, J. A.; Gracias, D. T.; Hope, J. L.; Stairiker, C. J.; Patel, P. R.; Mueller, Y. M.; McHugh, M. D.; Jablonowski, L. J.; Wheatley, M. A.; Katsikis, P. D., Acute exposure to ZnO nanoparticles induces autophagic immune cell death. Nanotoxicology 2015, 9 (6), 737-748.

27. Condello, M.; De Berardis, B.; Ammendolia, M. G.; Barone, F.; Condello, G.; Degan, P.; Meschini, S., ZnO nanoparticle tracking from uptake to genotoxic damage in human colon carcinoma cells. Toxicology in Vitro 2016, 35, 169-179.

28. Gilbert, B.; Fakra, S. C.; Xia, T.; Pokhrel, S.; Madler, L.; Nel, A. E., The Fate of ZnO Nanoparticles Administered to Human Bronchial Epithelial Cells. Acs Nano 2012, 6 (6), 4921-4930.

29. Chevallet, M.; Gallet, B.; Fuchs, A.; Jouneau, P. H.; Um, K.; Mintz, E.; Michaud-Soret, I., Metal homeostasis disruption and mitochondrial dysfunction in hepatocytes exposed to sub-toxic doses of zinc oxide nanoparticles. Nanoscale 2016, 8 (43), 18495-18506.

30. Song, W. H.; Zhang, J. Y.; Guo, J.; Zhang, J. H.; Ding, F.; Li, L. Y.; Sun, Z. T., Role of the dissolved zinc ion and reactive oxygen species in cytotoxicity of ZnO nanoparticles. Toxicology Letters 2010, 199 (3), 389-397.

31. Shen, C. C.; James, S. A.; de Jonge, M. D.; Turney, T. W.; Wright, P. F. A.; Feltis, B. N., Relating Cytotoxicity, Zinc Ions, and Reactive Oxygen in ZnO NanoparticleExposed Human Immune Cells. Toxicological Sciences 2013, 136 (1), 120-130.

32. Applerot, G.; Lipovsky, A.; Dror, R.; Perkas, N.; Nitzan, Y.; Lubart, R.; Gedanken, A., Enhanced Antibacterial Activity of Nanocrystalline ZnO Due to Increased ROS-Mediated Cell Injury. Advanced Functional Materials 2009, 19 (6), 842-852.

33. Yang, Q. B.; Lin, T. S.; Burton, C.; Park, S. H.; Ma, Y. F., Physicochemical insights of irradiation-enhanced hydroxyl radical generation from ZnO nanoparticles. Toxicology Research 2016, 5 (2), 482-491.

34. Galush, W. J.; Shelby, S. A.; Mulvihill, M. J.; Tao, A.; Yang, P. D.; Groves, J. T., A Nanocube Plasmonic Sensor for Molecular Binding on Membrane Surfaces. Nano Letters 2009, 9 (5), 2077-2082.

35. Anders, C. B.; Eixenberger, J. E.; Franco, N. A.; Hermann, R. J.; Rainey, K. D.; Chess, J. J.; Punnoose, A.; Wingett, D. G., ZnO nanoparticle preparation route influences surface reactivity, dissolution and cytotoxicity. Environmental Science-Nano 2018, 5 (2), 572-588.

36. Wang, B.; Zhang, Y. Y.; Mao, Z. W.; Yu, D. H.; Gao, C. Y., Toxicity of ZnO Nanoparticles to Macrophages Due to Cell Uptake and Intracellular Release of Zinc Ions. Journal of Nanoscience and Nanotechnology 2014, 14 (8), 5688-5696.

37. Cho, E. C.; Zhang, Q.; Xia, Y. N., The effect of sedimentation and diffusion on cellular uptake of gold nanoparticles. Nature Nanotechnology 2011, 6 (6), 385-391.

38. Anders, C. B.; Chess, J. J.; Wingett, D. G.; Punnoose, A., Serum Proteins Enhance Dispersion Stability and Influence the Cytotoxicity and Dosimetry of ZnO Nanoparticles in Suspension and Adherent Cancer Cell Models. Nanoscale Research Letters 2015, 10, 22.

39. Lundqvist, M.; Stigler, J.; Elia, G.; Lynch, I.; Cedervall, T.; Dawson, K. A., Nanoparticle size and surface properties determine the protein corona with possible implications for biological impacts. Proceedings of the National Academy of Sciences of the United States of America 2008, 105 (38), 14265-14270.

40. Mu, Q. S.; David, C. A.; Galceran, J.; Rey-Castro, C.; Krzeminski, L.; Wallace, R.; Bamiduro, F.; Milne, S. J.; Hondow, N. S.; Brydson, R.; Vizcay-Barrena, G.; Routledge, M. N.; Jeuken, L. J. C.; Brown, A. P., Systematic Investigation of the

Physicochemical Factors That Contribute to the Toxicity of ZnO Nanoparticles. Chemical Research in Toxicology 2014, 27 (4), 558-567.

41. Lv, J. T.; Zhang, S. Z.; Luo, L.; Han, W.; Zhang, J.; Yang, K.; Christie, P., Dissolution and Microstructural Transformation of ZnO Nanoparticles under the Influence of Phosphate. Environmental Science & Technology 2012, 46 (13), 7215-7221.

42. Herrmann, R.; Garcia-Garcia, F. J.; Reller, A., Rapid degradation of zinc oxide nanoparticles by phosphate ions. Beilstein Journal of Nanotechnology 2014, 5, 2007-2015.

43. Resch-Genger, U.; Grabolle, M.; Cavaliere-Jaricot, S.; Nitschke, R.; Nann, T., Quantum dots versus organic dyes as fluorescent labels. Nature Methods 2008, 5 (9), 763-775.

44. Biju, V.; Itoh, T.; Anas, A.; Sujith, A.; Ishikawa, M., Semiconductor quantum dots and metal nanoparticles: syntheses, optical properties, and biological applications. Analytical and Bioanalytical Chemistry 2008, 391 (7), 2469-2495.

45. Chen, N.; He, Y.; Su, Y. Y.; Li, X. M.; Huang, Q.; Wang, H. F.; Zhang, X. Z.; Tai, R. Z.; Fan, C. H., The cytotoxicity of cadmium-based quantum dots. Biomaterials 2012, 33 (5), 1238-1244.

46. Hardman, R., A Toxicologic Review of Quantum Dots: Toxicity Depends on Physicochemical and Environmental Factors. Environmental Health Perspectives 2006, 114 (2), 165-172.

47. Wang, H.; Wingett, D.; Engelhard, M. H.; Feris, K.; Reddy, K. M.; Turner, P.; Layne, J.; Hanley, C.; Bell, J.; Tenne, D.; Wang, C.; Punnoose, A., Fluorescent dye encapsulated ZnO particles with cell-specific toxicity for potential use in biomedical applications. Journal of Materials Science-Materials in Medicine 2009, 20 (1), 11-22.

48. Liu, Y. L.; Ai, K. L.; Yuan, Q. H.; Lu, L. H., Fluorescence-enhanced gadolinium-doped zinc oxide quantum dots for magnetic resonance and fluorescence imaging. Biomaterials 2011, 32 (4), 1185-1192.

49. Xiong, H. M., Photoluminescent ZnO nanoparticles modified by polymers. Journal of Materials Chemistry 2010, 20 (21), 4251-4262.

50. Ghaemi, B.; Mashinchian, O.; Mousavi, T.; Karimi, R.; Kharrazi, S.; Amani, A., Harnessing the Cancer Radiation Therapy by Lanthanide-Doped Zinc Oxide Based Theranostic Nanoparticles. Acs Applied Materials & Interfaces 2016, 8 (5), 3123-3134.

51. Premanathan, M.; Karthikeyan, K.; Jeyasubramanian, K.; Manivannan, G., Selective toxicity of ZnO nanoparticles toward Gram-positive bacteria and cancer cells by apoptosis through lipid peroxidation. Nanomedicine-Nanotechnology Biology and Medicine 2011, 7 (2), 184-192.

52. Ostrovsky, S.; Kazimirsky, G.; Gedanken, A.; Brodie, C., Selective Cytotoxic Effect of ZnO Nanoparticles on Glioma Cells. Nano Research 2009, 2 (11), 882-890.

53. Sasidharan, A.; Chandran, P.; Menon, D.; Raman, S.; Nair, S.; Koyakutty, M., Rapid dissolution of ZnO nanocrystals in acidic cancer microenvironment leading to preferential apoptosis. Nanoscale 2011, 3 (9), 3657-3669.

54. Akhtar, M. J.; Ahamed, M.; Kumar, S.; Khan, M. A. M.; Ahmad, J.; Alrokayan, S. A., Zinc oxide nanoparticles selectively induce apoptosis in human cancer cells through reactive oxygen species. International Journal of Nanomedicine 2012, 7, 845-857.

55. Ye, D. X.; Ma, Y. Y.; Zhao, W.; Cao, H. M.; Kong, J. L.; Xiong, H. M.; Mohwald, H., ZnO-Based Nanoplatforms for Labeling and Treatment of Mouse Tumors without Detectable Toxic Side Effects. Acs Nano 2016, 10 (4), 4294-4300.

56. Bisht, G.; Rayamajhi, S., ZnO Nanoparticles: A Promising Anticancer Agent. Nanobiomedicine 2016, 3, 9.

57. Hackenberg, S.; Scherzed, A.; Kessler, M.; Froelich, K.; Ginzkey, C.; Koehler, C.; Burghartz, M.; Hagen, R.; Kleinsasser, N., Zinc oxide nanoparticles induce photocatalytic cell death in human head and neck squamous cell carcinoma cell lines in vitro. International Journal of Oncology 2010, 37 (6), 1583-1590.

58. Li, J. Y.; Guo, D. D.; Wang, X. M.; Wang, H. P.; Jiang, H.; Chen, B. A., The Photodynamic Effect of Different Size ZnO Nanoparticles on Cancer Cell Proliferation In Vitro. Nanoscale Research Letters 2010, 5 (6), 1063-1071.

59. Zhang, H. J.; Shan, Y. F.; Dong, L. J., A Comparison of TiO2 and ZnO Nanoparticles as Photosensitizers in Photodynamic Therapy for Cancer. Journal of Biomedical Nanotechnology 2014, 10 (8), 1450-1457.

60. Guo, D. D.; Wu, C. H.; Jiang, H.; Li, Q. N.; Wang, X. M.; Chen, B. A., Synergistic cytotoxic effect of different sized ZnO nanoparticles and daunorubicin against leukemia cancer cells under UV irradiation. Journal of Photochemistry and Photobiology B-Biology 2008, 93 (3), 119-126.

61. Muharnmad, F.; Guo, M. Y.; Qi, W. X.; Sun, F. X.; Wang, A. F.; Guo, Y. J.; Zhu, G. S., pH-Triggered Controlled Drug Release from Mesoporous Silica Nanoparticles via Intracelluar Dissolution of ZnO Nanolids. Journal of the American Chemical Society 2011, 133 (23), 8778-8781.

62. Mitra, S.; Subia, B.; Patra, P.; Chandra, S.; Debnath, N.; Das, S.; Banerjee, R.; Kundu, S. C.; Pramanik, P.; Goswami, A., Porous ZnO nanorod for targeted delivery of doxorubicin: in vitro and in vivo response for therapeutic applications. Journal of Materials Chemistry 2012, 22 (45), 24145-24154.

# CHAPTER TWO: RAPID DISSOLUTION OF ZNO NANOPARTICLES INDUCED BY BIOLOGICAL BUFFERS SIGNIFICANTLY IMPACTS CYTOTOXICITY

Josh E. Eixenberger†‡, Catherine B. Anders†‡, Rebecca J. Hermann†, Raquel J. Brown⊥, Kongara M. Reddy‡, Alex Punnoose‡ and Denise G. Wingett*†

†Biomolecular Sciences Graduate Program, ‡Department of Physics, ⊥Biomolecular Research Center, Boise State University, Boise, ID 83725, USA

*Email: denisewingett@boisestate.edu

Reproduced with permission from ACS: Chemical Research in Toxicology (2017) 30, 8, 1641-1651, https://pubs.acs.org/doi/abs/10.1021/acs.chemrestox.7b00136, DOI: 10.1021/acs.chemrestox.7b00136. 

No significant changes were made to this publication.

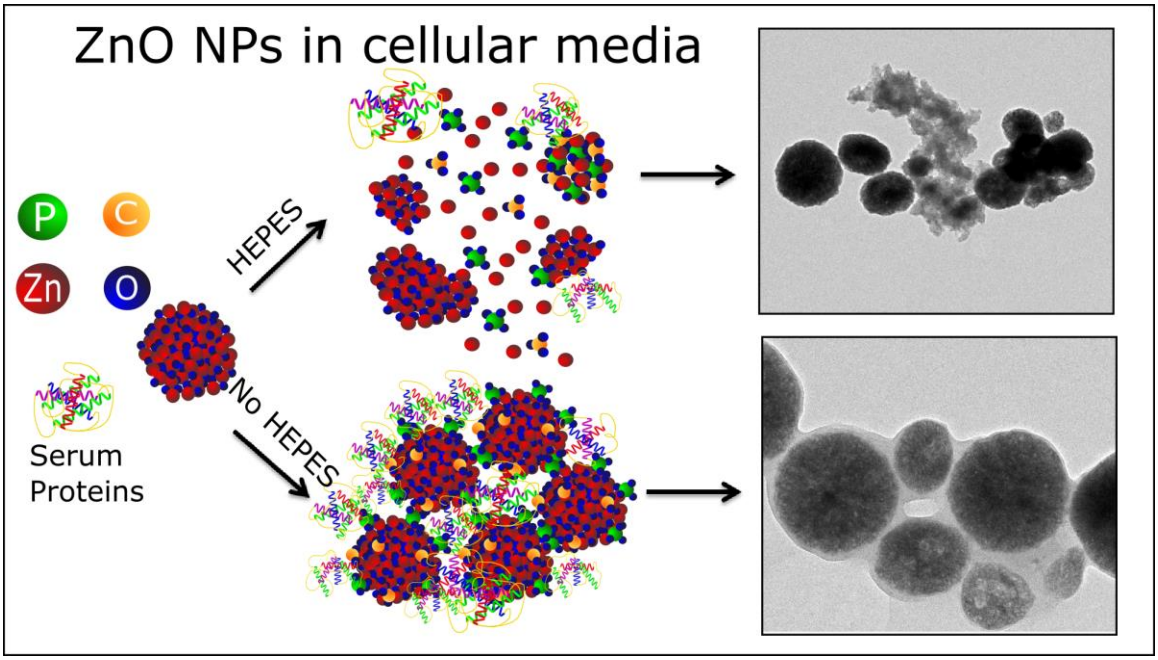


**Abstract**

Zinc oxide nanoparticles (nZnO) are one of the most highly produced nanomaterials and are used in numerous applications including cosmetics and sunscreens despite reports demonstrating their cytotoxicity. Dissolution is viewed as one of the main sources of nanoparticle (NP) toxicity; however, dissolution studies can be time-intensive to perform and complicated by issues such as particle separation from solution. Our work attempts to overcome some of these challenges by utilizing new methods using UV/vis and fluorescence spectroscopy to quantitatively assess nZnO dissolution in various biologically relevant solutions. All biological buffers tested induce rapid dissolution of nZnO. These buffers, including HEPES, MOPS, and PIPES, are commonly used in cell culture media, cellular imaging solutions, and to maintain physiological pH. Additional studies using X-ray diffraction, FT-IR, X-ray photoelectron spectroscopy, ICP-MS, and TEM were performed to understand how the inclusion of these nonessential media components impacts the behavior of nZnO in RPMI media. From these assessments, we

demonstrate that HEPES causes increased dissolution kinetics, boosts the conversion of nZnO into zinc phosphate/carbonate, and, interestingly, alters the structural morphology of the complex precipitates formed with nZnO in cell culture conditions. Cell viability experiments demonstrated that the inclusion of these buffers significantly decrease the viability of Jurkat leukemic cells when challenged with nZnO. This work demonstrates that biologically relevant buffering systems dramatically impact the dynamics of nZnO including dissolution kinetics, morphology, complex precipitate formation, and toxicity profiles.

## Introduction

Nanomaterials have generated much attention over the past decade due to the emergence of novel properties generally not apparent in their bulk micron-sized counterparts. These novel properties have led to applications in electronics, optics, antimicrobial materials, and coatings.[1–3] Specifically, ZnO nanoparticles (nZnO) are highly produced and extensively used in commercial products such as electronics, cosmetics, and sunscreens.[4–7] However, when prepared at the nanoscale size, numerous recent reports demonstrate high cytotoxicity from nZnO in various cell lines and model organisms.[8–12] The large production volume of nZnO, coupled with an incomplete understanding of what physicochemical properties contribute to their toxicity, poses a concern to the environment and public health.[13] The mechanism of toxicity is heavily debated, with multiple factors contributing to the source of cytotoxicity. These mechanisms are generally thought to depend on physicochemical properties such as size, dissolution kinetics, and retained surface species.[14–17] With such variability in nZnO properties, numerous mechanisms have been suggested including membrane disruption,

generation of reactive oxygen species (ROS), and particle dissolution.[18–20] Most researchers recognize the complex nature of deciphering the exact source of cytotoxicity as multiple mechanisms occur concurrently and vary between cell lines.[21–24] Dissolution is considered a significant contributor to the cytotoxicity of nZnO and has been the focus of numerous studies.[25–27] The dissolution properties appear to be influenced by the size, shape, defects, and synthesis procedure.[28,29] This has established the need to present detailed physicochemical characterizations of nZnO so that researchers can decipher findings and make meaningful conclusions. Studies have shown how biologically relevant species interact and affect the dissolution properties of nZnO, which has further confounded the interpretations of complex dissolution studies.[26,27,30] Through these studies, it has been understood that particle dissolution is affected by pH, ionic strength, adsorption of complexing ligands, phosphate ion concentration, and interactions with carbonates in the media.[28–32] These findings highlight the fact that the complexity of toxicity assessments stems from more than the physicochemical properties of nZnO and requires an understanding of how media components alter their toxicity. Dissolution studies on particle systems are often carried out by inductively coupled plasma mass spectrometry (ICP-MS), inductively coupled plasma atomic emission spectroscopy (ICP-AES), and atomic absorption spectroscopy (AAS), which are a few of the standards for quantitative analysis. However, the quantification of nanoparticle (NP) dissolution presents difficulties including the physical separation of NPs from the dissolved ionic species, insoluble precipitant formation, and achieving an equilibrium phase along with time and cost factors.[25,26,33,34] In this work, we attempt to overcome some of these challenges and present simple methods using UV/vis absorbance spectra and

spectrofluorometric monitoring to measure real-time dissolution kinetics of nZnO supported by ICP-MS and microscopy techniques. By taking the dissolution results into consideration, studies on cell viability were performed to determine how common buffering systems affect dissolution kinetics that impacts the structural transformation and cytotoxicity of nZnO. To our knowledge, no reports exists that address particle dissolution induced by these buffering solutions and the resulting effects that impact NP toxicity.

## Experimental Procedures

### nZnO Synthesis and Characterization

ZnO NP samples were produced using the forced hydrolysis method as previously reported.[35] Briefly, zinc acetate was added to diethylene glycol (DEG), and the solution brought to 80 °C. Nanopure water was added, and the solution was heated to 150 °C and held for 90 min. Upon cooling to room temperature, the NPs were collected by centrifugation at 41410g, subsequently washed with ethanol, and the pellet dried overnight at 60 °C. ZnO NPs where characterized using X-ray diffraction (XRD), transmission electron microscopy (TEM), dynamic light scattering (DLS), X-ray photoelectron spectroscopy (XPS), and Fourier transformed infrared spectroscopy (FT-IR). XRD spectra were collected using a Rigaku Miniflex 600 X-ray diffractometer, and the crystal phase, lattice parameters, and average crystalline size determined using Rigaku PDXL software version 1.8.0.3. NP size distributions were obtained using randomly selected particles in images obtained from a JEOL JEM-2100 HR analytical transmission electron microscope. DLS and zeta potential measurements were performed in nanopure water at a concentration of 1 mg/mL using a Malvern Zetasizer NanoZS.

Real-Time Kinetics of nZnO Dissolution

Real-time dissolution kinetics measurements were performed using DLS, UV/vis spectrometry, fluorescence spectroscopy, and confirmed using inductively coupled plasma mass spectrometry (ICP-MS). For comparison and consistency, all NP stock solutions were made by suspending nZnO at a concentration of 2.035 mg/mL, vortex mixing, and sonicating the solution for 10 min. An aliquot of 40 μL was added to 1.92 mL of nanopure water for a final concentration of 40.7 μg/mL (~0.5 mM). All buffers used were prepared at a 0.5 M concentration (except PBS, made at 20×, and sodium bicarbonate, made at 75 mg/mL) and pH adjusted to 7.4. For each interaction study, 40 μL of each stock buffer (100 μL 20× PBS) was added to the NP solution (2 mL total solution for a 2% overall change in NP concentration) to monitor NP dissolution kinetics. The Malvern Zetasizer NanoZS was used to qualitatively assess NP dissolution kinetics in size mode by acquiring 2 runs with 5 s run durations, totaling 180 runs with a 10 s pause in between runs. Fluorescence spectra were collected at room temperature using a FluoroMax-4 spectrofluorometer with 4.5 mL disposable cuvettes with a working range of 285−750 nm. Fluorescence spectra were collected with multiple excitation wavelengths (310−340 nm); however, 310 nm was chosen to eliminate the Raman peak, associated with water, that would convolute with the nZnO emission spectra when using higher wavelengths for excitation (see Supporting Information, Figure S2.1). Monitoring the emission peak at 368 nm yielded a linear correlation between fluorescence and concentration of nZnO (see Supporting Information, Figure S2.3). For kinetics measurements, the kinetics mode was used with 310 nm/368 nm ex/em with 2 nm slit width and 0.5 s integration times. Using the linear correlation, counts per second (CPS)

were converted to concentration of nZnO in solution. Absorbance spectra were obtained at room temperature using a CARY 5000 spectrophotometer using 4.5 mL disposable cuvettes with a working wavelength range of 285−750 nm. Initially, full absorbance spectra were collected from 290−550 nm. A linear correlation between absorbance and concentration was also achieved, and dissolution kinetics was obtained by monitoring absorbance at 368 nm in kinetics mode for consistency (see Supporting Information, Figure S2.2). For ICP-MS studies, solutions were made by the same procedure but incubated in Ultracel-4 3k centrifugal filter units (Millipore) for 20 min. Solutions were then centrifuged at 4000g for 10 min to remove any NPs and precipitates. A 0.5 mL aliquot was transferred to 24.5 mL 2% high purity nitric acid solution and analyzed by the ThermoElectron X-series II quadrupole ICP-MS for determination of total free zinc ions in solution.

Effects of HEPES on the Behavior of nZnO in Biological Media

To assess the role that HEPES plays on the dissolution properties and fate of nZnO in biological media, RPMI 1640 (see American Type Tissue Collection (ATTC) Web site for formulation, www.atcc.org) with and without 10 mM HEPES was used in these studies. To determine the amount of free zinc ions in solution, ICPMS was employed to analyze the amount of free zinc in the media at various time points. For this study, 150 μL of 4.07 mg/mL ZnO NPs was added to 15 mL (40.7 μg/mL overall NP concentration) of RPMI 1640 (with and without 10 mM HEPES) in tissue culture flasks. The flasks were then moved into a cell culture incubator at 37 °C and 5% $CO_2$ atmosphere. Two milliliter aliquots were taken out at various time points and transferred to Ultracel-3K centrifugal filter units and centrifuged for 10 min at 4000g. Additional

preparation for ICP-MS studies was performed as described above. nZnO and free zinc have been shown to form precipitates in media containing sodium bicarbonate and phosphates. To determine how HEPES in the media influences the transformation of nZnO, XRD, XPS, and FT-IR were utilized to characterize NP/precipitate formation in the media. For basic control reactions, 50 mM ZnCl2 was mixed in solution containing sodium bicarbonate or PBS to form precipitant and was collected via centrifugation at 41410g and subsequently analyzed by FT-IR (see Supporting Information, Figure S2.9). For media/nZnO studies, 10 mL of 4.07 mg/mL ZnO NP stock was added to 0.5 L of RPMI 1640 with and without 10 mM HEPES. The solution was shaken and incubated at room temperature. At various time points, the solution was centrifuged at 41410g for 10 min. The pellet was washed with nanopure water and dried overnight at 60 °C. For analysis, a Rigaku Miniflex 600 X-ray diffractometer was used to obtain the XRD pattern of the powdered sample, and images were obtained with a JEOL JEM-2100 HR analytical transmission electron microscope. XPS spectra were collected using a Physical Electronics Versaprobe system with a monochromated Al Kα X-ray source. The beam diameter was approximately 100 μm with 25 W of power. For general survey scans, a pass energy of 117.5 eV was used and for higher resolution core level scans, a pass energy of 23.65 eV was utilized. Deconvolution of peaks was carried out using OriginPro 2017. FT-IR pellets were produced by grinding 1.5 mg of nZnO/precipitants with 2.000 g of KBr and pressed with 8 tons of pressure for 4 min. FT-IR spectra were collected using a Bruker Tensor 27 spectrometer. Deconvolution of the FT-IR peaks was performed using OPUS 7.0.129. Cell Culture and Viability Studies. To assess the effect that HEPES has on the cytotoxicity profiles of nZnO, the Jurkat T cell line was used as a model

system. Cells were cultured in RPMI 1640 containing 10 mM HEPES and supplemented with 10% FBS (fetal bovine serum), 1% penicillin/streptomycin, and 2 mM L-glutamine per ATCC (American Type Culture Collection, Rockville, MD) recommendation. Cells were maintained in log phase and seeded at a concentration of 5 × 105 cells/mL in a 96-well plate for viability assays. A fresh stock solution of nZnO was prepared for each viability experiment by sonicating nZnO in autoclaved DI water at a concentration of 4.07 mg/mL for 10 min. RPMI 1640 without HEPES was then added to the stock solution (to avoid vehicle effects) to bring the final concentration to 2.035 mg/mL and subsequently sonicated for an additional 10 min. During the sonication step, cells were concurrently plated and then treated with the nZnO stock solution immediately after sonication. Cells were then cultured for 24 h at 37°C and 5% CO2. For the Alamar Blue metabolic assay, Alamar Blue (10% (v/v)) was added 20 h after treatment with NPs and incubated for an additional 4 h at 37 °C and 5% CO2. The fluorescence intensity was determined at 24 h by a Biotek Synergy MX plate reader using excitation/emission at 530/590 nm. Flow cytometry was also employed to verify experimental results. After the 24 h treatment period, cells were washed with PBS (phosphate buffered saline) and resuspended in FACS buffer (PBS/15% FBS/0.02% NaN3) and stained with a FITC labeled anti-HLA ABC antibody (BD Biosciences, San Jose, CA). Cells were subsequently washed, and 0.4 μg/mL propidium iodide (PI) was added to stain and detect nonviable cells using a BD FACS Caliber flow cytometer.

Confocal Microscopy

Confocal microscopy was utilized in reflection mode to image the dissolution of nZnO. Briefly, 81.4 μg/ mL solutions of nZnO in nanopure water were placed on Wilco

well glass bottom dishes and allowed to dry overnight. Nanopure water was added prior to imaging as a control to ensure the disappearance of NPs was due to dissolution from HEPES and not from solubility/ dissolution in water. Confocal images were acquired in reflectance mode as a Z-stack/time series utilizing the α-Plan-FLUAR 100x/NA 1.45/oil objective, an argon (514 nm) laser as excitation source, and a BP505−550 emission filter. Specifically, images with a frame size of 69.1 μm × 69.1 μm (0.14 μm pixel size) were acquired every 9.576 s for 30 min. To account for optical drift and ensure collecting the optical plane of interest, three 0.2 μm overlapping slices over a Z-range of 0.4 μm were collected. Image processing was performed with ZEN 2009 imaging software (Carl Zeiss, Inc., Thornwood, NY).

Statistical Analysis

The data for Figure 2.9 were analyzed with a linear mixed model, with fixed effects of presence or absence of HEPES buffer, concentration, and their interaction. The date of the experiment was modeled as a random effect using compound symmetry for the correlation among outcomes run on the same date. Viability at each concentration was compared between HEPES and no HEPES, and comparisons were adjusted using the Bonferroni step-up correction to control family wise type 1 error rate at 5%.[36]

## Results

ZnO Nanoparticle Synthesis and Characterization

nZnO was synthesized by a wet chemical method using the forced hydrolysis of zinc acetate solubilized in DEG.35 X-ray powder diffraction spectra showed the expected hexagonal wurzite crystal structure with an average crystal size of 9.0 ± 2.3 nm. The lattice parameters obtained from analysis were a = 3.253 and c = 5.215, and no other

crystal phases were detected. TEM images in Figure 2.1 show large aggregates with a size range of 50−600 nm made up of small individual ZnO crystals of an average size of 9.8 ± 1.7 nm, which is consistent with XRD analysis (see Supporting Information, Figure S2.8). The high resolution TEM (HRTEM) image (Figure 2.1C) demonstrates that the crystal lattice terminates at the boundary of the crystals, indicating no coatings or amorphous phases are present on the surface. Dynamic light scattering and electrophoretic measurements performed in nanopure water revealed an average hydrodynamic size of 345 ± 13.6 nm and zeta potential of +35.7 mV. Additional characterization information from FTIR spectra, X-ray photoelectron spectroscopy (XPS), and dissolution kinetics are discussed in subsequent sections.

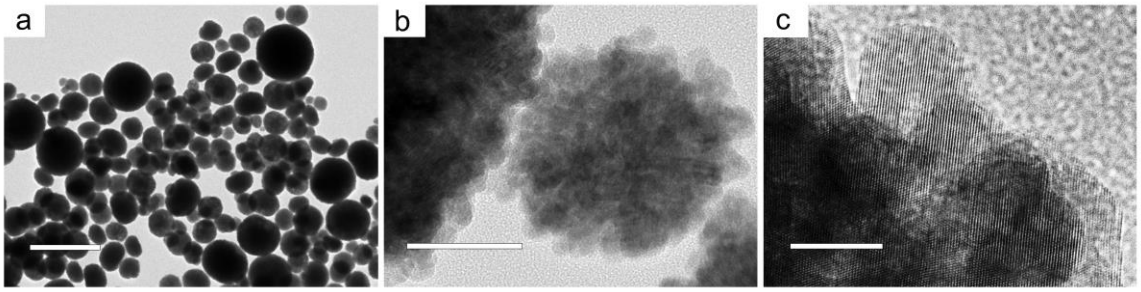


**Figure 2.1 (a) Scale bar: 1 µm. Low magnification image shows large spherical aggregates of ZnO with a size range of 50-600 nm. (b) Scale bar: 50 nm. Higher magnification reveals aggregates are comprised of nZnO crystals with an average size of 9.8 ± 1.7 nm. (c) Scale bar: 10 nm. High-resolution TEM image demonstrates crystal lattice termination at the crystal boundary with no amorphous structures or coatings.**

Real-Time Dissolution Kinetics

Certain media components have been shown to interact with NPs by influencing their interactions with cells due to protein corona formation, development of insoluble precipitants, and altering dissolution equilibriums.[29,32,37] By utilizing the newly proposed methods, numerous media components were screened to assess their effect on the

dissolution properties of nZnO. Media components tested, such as glucose and various salts, had little effect on the dissolution properties in the time scale evaluated but did affect particle aggregation and sedimentation profiles as seen in previous reports (see Supporting Information, Figure S2.4).[28,38] Interestingly, it was found that 4-(2-hydroxyethyl)-1piperazineethanesulfonic acid (HEPES), a common component in biological media, induces rapid dissolution of nZnO observed by UV/vis spectroscopy, fluorescence spectroscopy, and verified by ICP-MS (Figure 2.2). With this finding, multiple biologically relevant buffers developed by Good et al. were tested.[39] Many of these buffers have been used in studies of nZnO in cell culture experiments, cellular imaging, and to maintain physiological pH.[25,27,29,35]

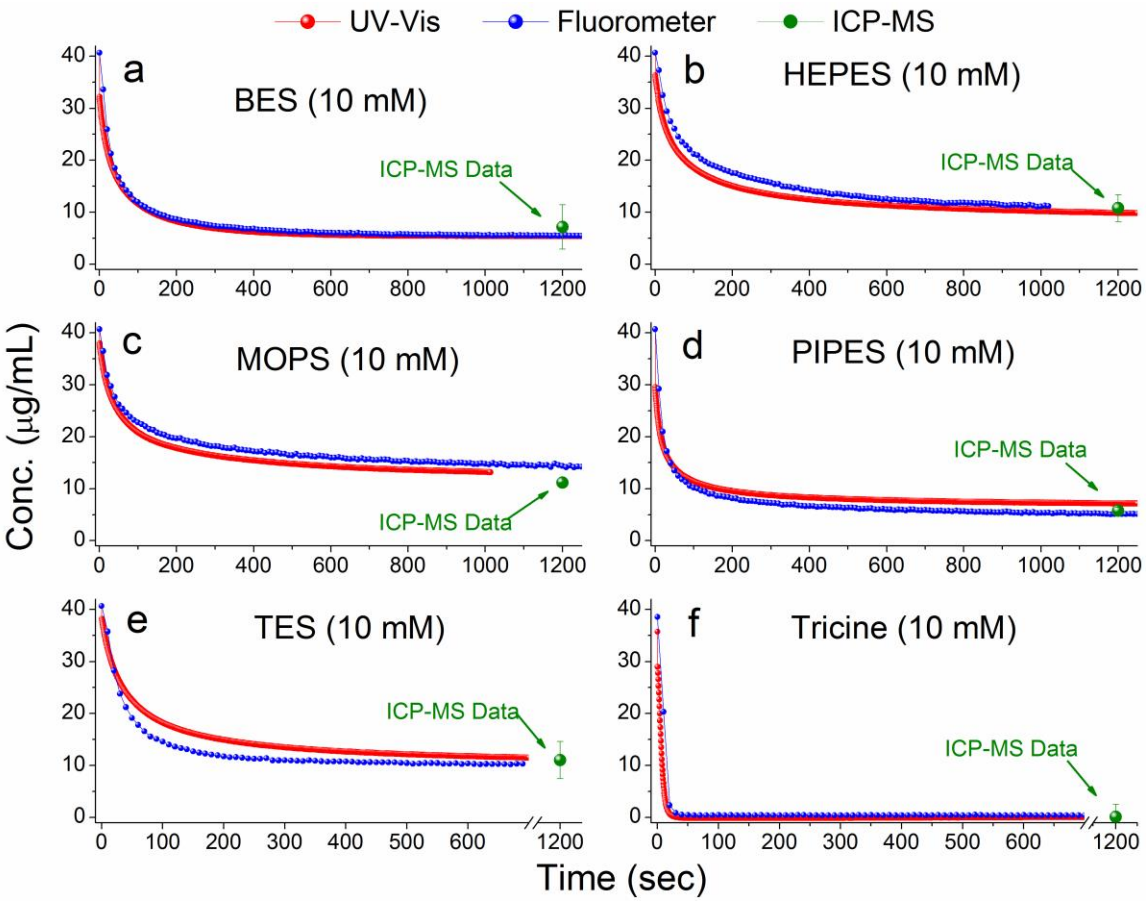

**Figure 2.2 (a)-(f) Real-time dissolution kinetics of 40.7 µg/mL(0.5 mM) nZnO from UV/vis spectroscopy and spectrofluorometric monitoring in various buffers developed by Good *et al*. Each buffer was prepared at a stock concentration of 500 mM and was adjusted to pH=7.4. ICP-MS data points are plotted on the kinetics profiles to demonstrate the reliability of converting spectra to quantitative concentration measurements. Measurements reveal that each of Good's buffers tested (10 mM final concentration) induced rapid dissolution of nZnO within 20 minutes.**

The real-time dissolution kinetics of 40.7 µg/mL nZnO (highest concentration possible for linear correlation; see Supporting Information, Figure S2.3) is shown in Figure 2.2 and demonstrates that all the buffers tested (pH = 7.4) induced rapid dissolution with various kinetics profiles. The dissolution kinetics for both absorbance and fluorescence monitoring techniques is very consistent as seen in Figure 2.2, and all experiments were performed in triplicate to ensure reproducibility (Supporting Information, Figure S2.6).

To assess the accuracy and reliability of converting the absorbance and fluorescence spectra to nZnO concentration, ICP-MS was utilized. The same reactions were completed in Ultracel-4 3k centrifugal filter units (pore size 0.1 nm) and centrifuged at 4000g to separate the remaining NPs from the free zinc ions. The data points were plotted over the kinetics profiles, which confirmed the results obtained from the new methods by utilizing absorbance and fluorescence spectra (Figure 2.2).

At least 72.5% dissolution of 0.5 mM nZnO (40.7 µg/mL) was achieved from each of the buffers (10 mM; pH = 7.4 ± 0.05) within 20 min (Table 1). The kinetics profiles highlight the ability of these methods to monitor rapid real-time dissolution kinetics that is lost in other quantitative assessments such as ICP-MS. Additionally, these methods eliminate the need to separate the particles from the solution, reducing time and cost factors. The ability to rapidly screen how biologically and environmental relevant

species impact the dissolution of nZnO will facilitate characterization and toxicity assessments.

**Table 2.1 ICP-MS measurements of the dissolution of nZnO (40.7 µg/mL) in various solutions after 20 minutes. PBS and sodium bicarbonate appear to have a lower percentage of dissolved nZnO than in nanopure water. However, insoluble zinc phosphates and zinc carbonates are removed in the separation process, lowering the calculated dissolution percentage. All of Good's buffers tested (pH= 7.4) induced 72.5% or more dissolution within the 20 minute time frame.**

| Buffer/Media | Concentration | nZnO Dissolution % |
|---|---|---|
| Nanopure Water | - | 4.8 ± 0.5 |
| Phosphate Buffered Saline | 1x | 3.3 ± 0.3 |
| Sodium Bicarbonate | 1.5 mg/mL | 1.4 ± 0.2 |
| MOPS | 10 mM | 72.5 ± 0.2 |
| TES | 10 mM | 72.8 ± 8.8 |
| HEPES | 10 mM | 73.5 ± 6.4 |
| BES | 10 mM | 82.4 ± 10.5 |
| PIPES | 10 mM | 85.7 ± 1.5 |
| Tricine | 10 mM | 99.6 ± 5.8 |

DLS was subsequently employed to qualitatively assess and confirm the dissolution of nZnO by monitoring the derived counts per second (CPS) while taking measurements in size mode. As seen in Figure 2.3, the number of CPS drastically reduced upon the addition of Good's buffers, while the number of CPS in PBS was maintained. In the solution containing tricine, the system stopped collecting measurements due to insufficient signal, qualitatively confirming complete dissolution.

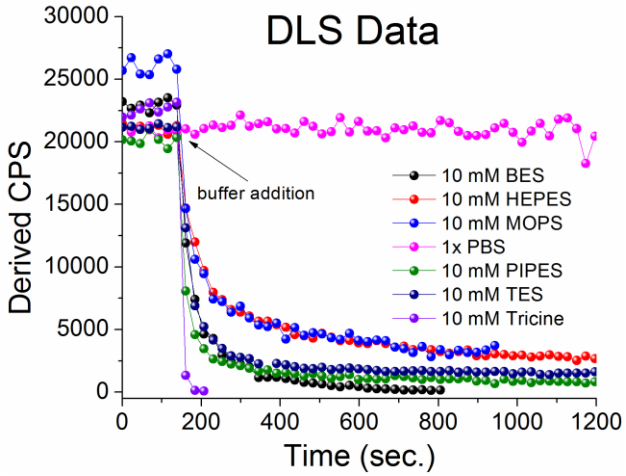


**Figure 2.3 A qualitative assessment of nZnO dissolution obtained from dynamic light scattering (DLS) monitored in size mode. All six Good's buffers induce rapid dissolution of nZnO as demonstrated by the fast reduction in derived counts per second (CPS).**

Confocal microscopy was utilized to visualize the dissolution of nZnO induced by the presence HEPES. No fluorescent tags were used, and the images generated were due to reflection from the NP aggregates on the bottom of the well. The apparent size of the nZnO aggregates was consistent with TEM and DLS hydrodynamic size measurements. As seen in Figure 2.4, little to no change was detected in the integrity of the NPs in water over the ~15 min (1000 s) time course. However, a striking reduction in size, intensity, and sharpness of the NP was seen upon the addition of HEPES (Figure 2.4d−f). The vast majority of NPs disappeared from the images within 250 s following the addition of HEPES (see Supporting Information for time-lapsed video).

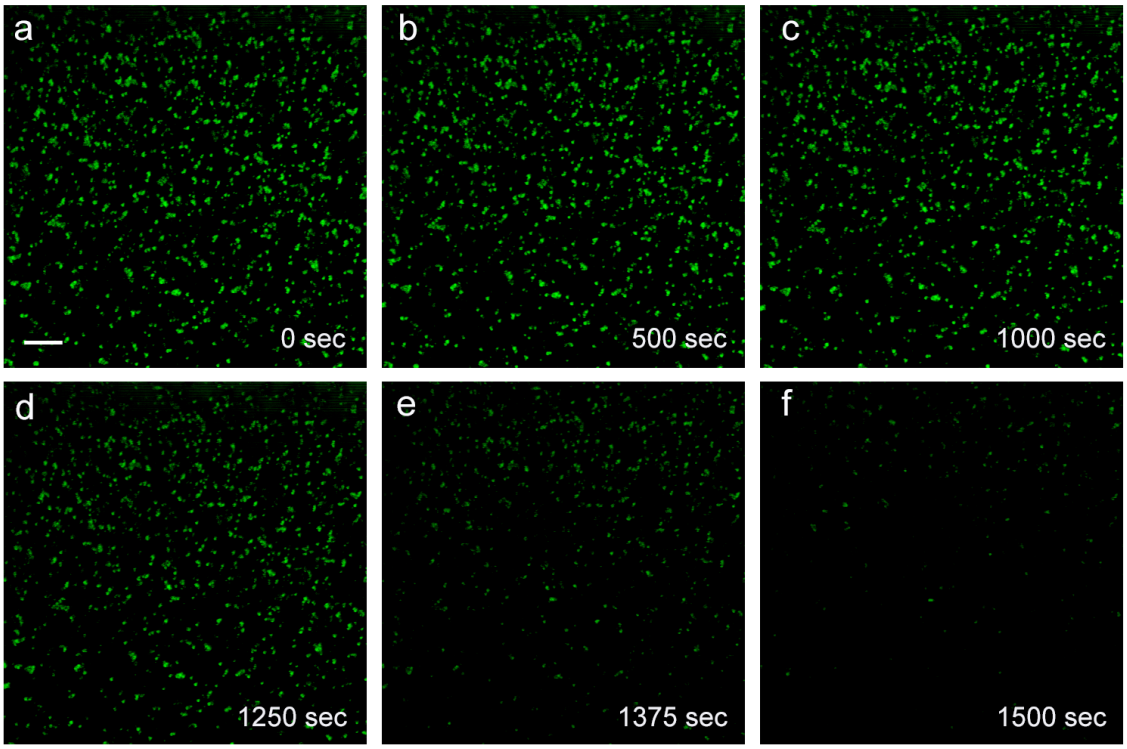


**Figure 2.4 Scale bar: 2 µm. A panel of nZnO confocal images obtained in reflection mode as a time series/z-stack. (a)-(c) DI water was added as a control to ensure any changes to the NPs wasn't due to solubility in water. (d)- (f) HEPES addition. nZnO quickly undergoes dissolution within the 250 second time frame, demonstrating significant dissolution by HEPES.**

Morphological Changes of ZnO NPs

It is important to note that the previous experiments were performed in simple solutions without salts and additional buffers such as PBS. The dynamics of nZnO in media are complex, and competing events such as protein corona formation, NP agglomeration/sedimentation, and achieving dissolution equilibrium all impact the toxicity profiles of nZnO. Additionally, reports have demonstrated microstructural transformation of nZnO due to phosphate ions and have shown that free zinc ions react in media to form various zinc carbonate and phosphate precipitants.[29,31,40] The complex nature of cellular media affects the dissolution kinetics of nZnO and the results from the

screening of numerous biological components prompted investigation into how inclusion of HEPES could potentially alter the dynamics of nZnO in cellular media.

ICP-MS was used to quantify the amount of free zinc in the media to determine any differences in dissolution kinetics from the inclusion of HEPES. nZnO was added to RPMI 1640 (with and without 10 mM HEPES) in culture flasks and placed in a cell culture incubator to mimic viability assay conditions. As seen in Figure 2.5, the media containing HEPES showed consistently higher levels of free zinc up to the 24 h time point. However, at 24 h, the levels were not appreciably different. This suggests a more rapid initial dissolution of the NPs in the presence of HEPES that eventually reaches the same equilibrium regardless of media composition. Since the inclusion of HEPES in RPMI media increases the dissolution rate of nZnO, investigations into how HEPES alters the structural transformation of nZnO were performed.

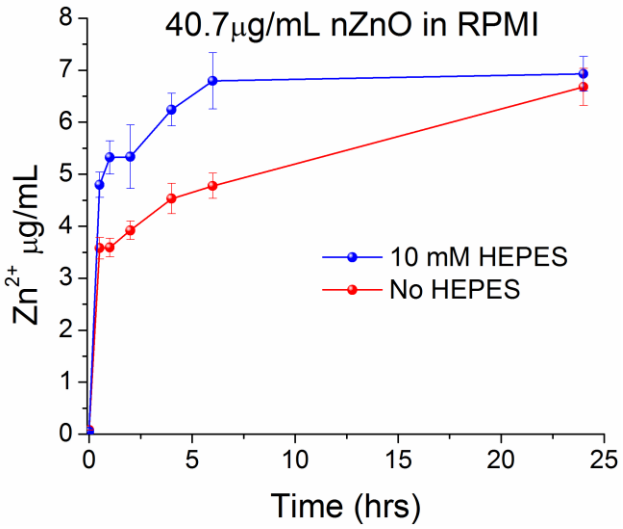


**Figure 2.5 ICP-MS measurements on the amount of free zinc ions from nZnO present in RPMI 1640 media with and without 10 mM HEPES over 24 hours.**

XRD was employed to assess changes in the nZnO crystalline size and to determine if crystalline phases of zinc phosphate or zinc carbonate appear in the spectra. In media with and without HEPES, only the hexagonal wurzite crystalline phase of ZnO was detected over the 24 h time course (see Supporting Information, Figure S2.8). However, any amorphous species formed in solution would not display a well-defined Bragg peak but broadening of the ZnO peaks were observed. During the 24 h treatment, the apparent average crystalline size from XRD slowly reduced from ~9.3 nm to ~7.5 nm in both situations, but no apparent differences were noted between the samples from XRD analysis.

We have previously demonstrated that nZnO with very similar properties such as crystal size, lattice parameters, and band gap have significant differences in their hydrodynamic size, zeta potential, and cytotoxicity due to differences in their surface chemistry.[17] FT-IR was utilized to investigate how the surface chemistry changed and determine which species formed. The FT-IR spectra of as-prepared nZnO showed the characteristic Zn−O vibrational modes at 478 $cm^{-1}$ (Figure 2.6).[17,41] However, during the 24 h time course, the Zn−O peak shifts down to 455 $cm^{-1}$, likely due to changes in the surface structure influencing the Zn−O bonds in the NPs. The two peaks at 1411 and 1597 $cm^{-1}$ are attributed to surface bound carboxylate groups retained from the zinc acetate precursor or the DEG solvent.[17] The intensity of these peaks was reduced upon addition to RPMI 1640 media and new functional groups appeared in the spectra as early as the 2 h time point.

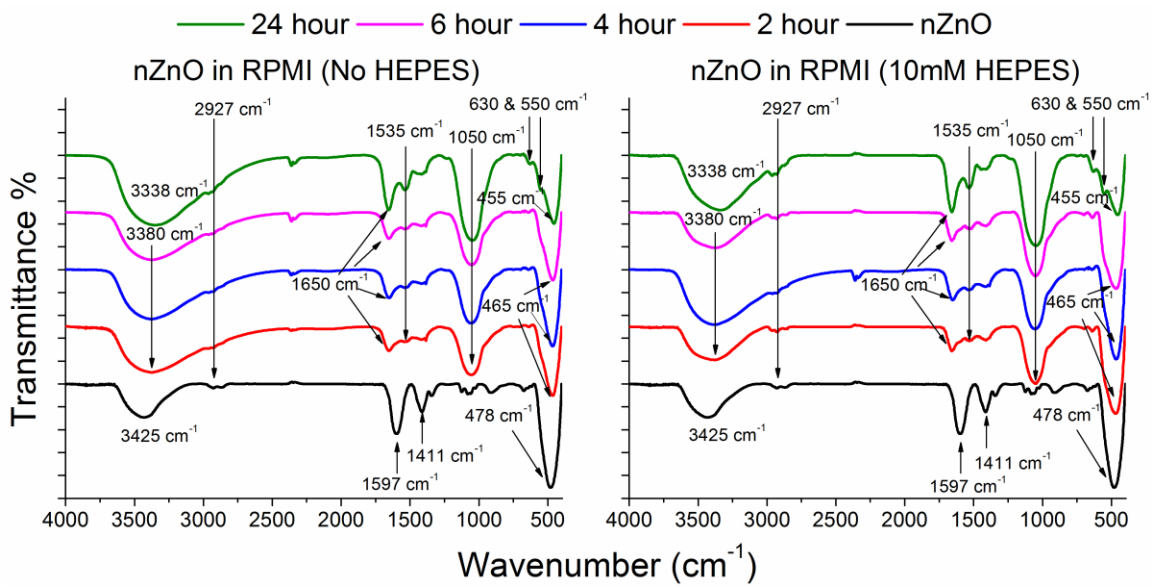


**Figure 2.6 FTIR spectra of as-prepared nZnO and nZnO post incubation in RPMI 1640 with (right) and without (left) 10 mM HEPES over 24 hours. The as-prepared nZnO FTIR spectra show a strong peak at 478 $cm^{-1}$ indicative of the Zn-O modes. Other functional groups found at 1411 $cm^{-1}$ and 1597 $cm^{-1}$ are due to carboxylate groups retained from the zinc acetate precursor or DEG solvent. New functional groups appear upon incubation in cellular media and the peaks at 550, 630 and 1050 $cm^{-1}$ are attributed to $PO_4^{3-}$ stretching and bending modes. The peaks near 1535 $cm^{-1}$ are from C=O stretching and may be from either carbonate formation or from Amide II bonds from protein corona formation. The broad O-H region shifts from 3425 $cm^{-1}$ to 3338 $cm^{-1}$ due to convolution of the O-H ban and new N-H stretching groups.**

The emergence of the strong peak at 1050 $cm^{-1}$ is attributed to a convolution of the $PO_4^{3-}$ symmetric and antisymmetric stretching modes.[42,43] The shoulder appearing at 550 $cm^{-1}$ is a convolution of the Zn−O stretch and a bending mode of $PO_4^{3-}$.[44] The shoulder appearing at 630 $cm^{-1}$ is associated with the bending mode of $PO_4^{3-}$ and increased in intensity over the 24 h.[44,45] The peak centered at 1535 $cm^{-1}$ is due to C-O stretching, indicating carbonates or amide II formation derived from interactions with carbonate or proteins in the media.[46–50] Up to the 24 h time point, nZnO shows a continual increase in peak intensity in the phosphate and carbonate/amide II regions. However, when the two samples at 24 h are compared (Figure 2.7), the ratio between the area of the phosphate peaks (1050 $cm^{-1}$) and the area of the Zn−O modes (420, 445, and

485 $cm^{-1}$) is higher in the media containing HEPES (4.13 vs 2.75), indicating increased dissolution and conversion to zinc phosphate.[51–55] Over the 24 h, the O−H broad region peak increased and shifted from 3425 to 3338 $cm^{-1}$, likely due to both the O−H region and increasing concentration of the N− H stretching regions from amide A and B bands.[49,50] The additional peak at 1650 $cm^{-1}$ is due to the presence of either crystalline water or more likely, the amide I mode from bound serum proteins.[42,43,50,56] These results indicate that the species formed are a complex mixture of nZnO, retained proteins from fetal bovine serum (FBS) in the media, and insoluble precipitate formation that is likely an amorphous mixture of zinc phosphate and carbonate species.

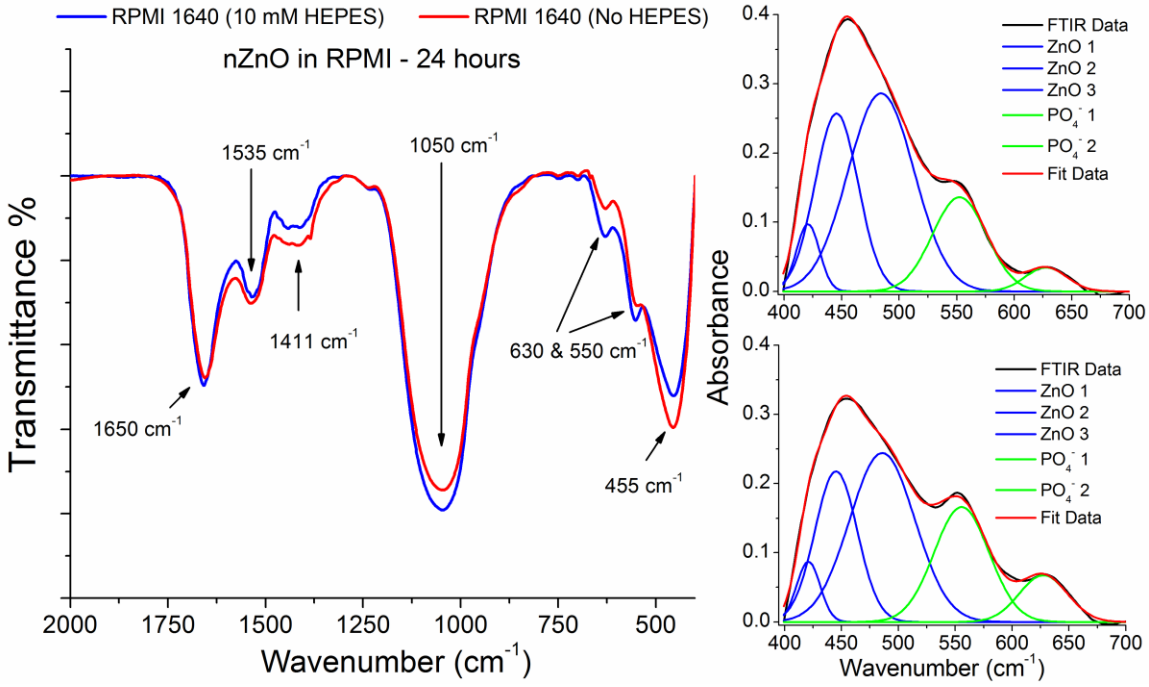


**Figure 2.7 (a) FTIR spectra of nZnO incubated in RPMI 1640 with (blue) and without (red) 10 mM HEPES at the 24 hour time point. The peak at 455 $cm^{-1}$ is attributed to Zn-O modes and the broad peak at 1050 $cm^{-1}$ is a convolution of $PO_4^{3-}$ stretching modes. Qualitatively, the peak intensity in HEPES free media is stronger in the Zn-O modes and weaker in the phosphate stretching modes than the media containing HEPES. The deconvolution of the Zn-O modes in media containing HEPES (c) and without (b) at 24 hours was used to compare the samples. The area of the 1050 $cm^{-1}$ phosphate peak was divided by the area of the three Zn-O peaks (420,445, and 485 $cm^{-1}$). A peak area ratio of 4.13 was obtained for nZnO incubated**

**in media containing HEPES vs. a ratio of 2.75 in the media without HEPES. This demonstrates a faster conversion of nZnO to zinc phosphate in RPMI 1640 containing 10 mM HEPES.**

XPS was utilized to quantify atomic concentrations of each element present as well as verify FT-IR results. By looking at the survey spectra of nZnO/precipitants collected at 24 h (Figure 2.8a), the atomic concentrations reveal that a major contribution to the amorphous species is an organic matrix likely from fetal bovine serum (FBS) proteins in the media. Additionally, by looking at the ratio between the total phosphate and zinc gives atomic ratios at 2.0 (10 mM HEPES media) versus 1.65 (HEPES free media), which is very similar to results obtained from FTIR, indicating increased phosphate formations in media containing 10 mM HEPES. High resolution core level scans of the Zn 2p3/2 region demonstrate a single peak at 1021.8 eV in the as-prepared nZnO sample (Figure 2.8b). Once introduced to media, new zinc species become apparent, with a new peak observed with a chemical shift of +2.0 eV from the Zn−O peak (Figure 2.8c) indicating Zn-$PO_4^{3-}$ bond formation (see Supporting Information, Figure S2.10). These results confirm complex formations of nZnO, proteins, and insoluble phosphate/carbonate precipitants.

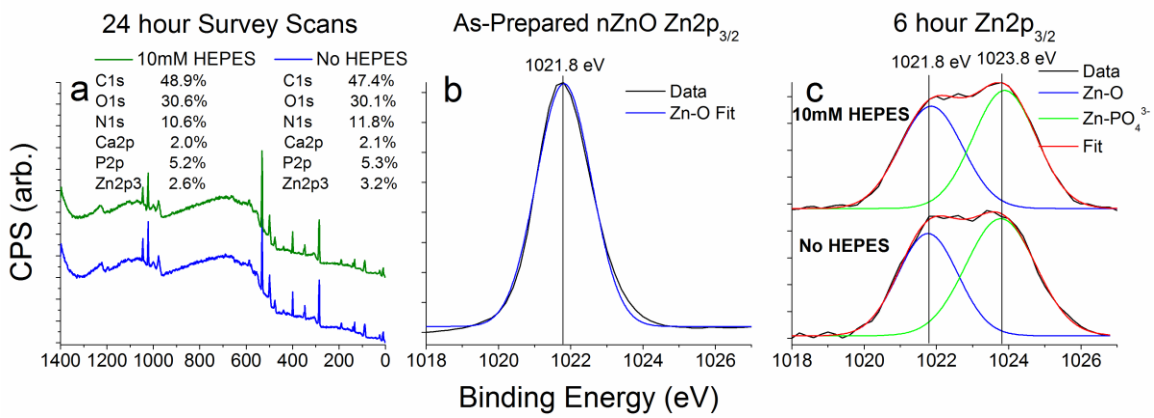


**Figure 2.8 XPS spectra of nZnO. (a) Survey scan of nZnO incubated in RPMI 1640 cellular media with and without 10 mM HEPES. Atomic concentrations of the various elements present are similar in both media types, however, the phosphorus to zinc ratio is different, with atomic concentration ratios of 2.0 (10 mM HEPES) and 1.65 (No HEPES). (b) The core level high resolution scan of the $Zn2p_{3/2}$ region of as-prepared nZnO demonstrates a single peak with a binding energy of 1021.8 eV. (c) A high resolution core level scan of the $Zn2p_{3/2}$ peak of nZnO incubated in cellular media for 6 hours reveals similar new zinc species present in both cases, apparent by the new peak appearing with a chemical shift of about 2 eV. XPS data verifies similar changes in media types, with a modest difference in the amount of ZnO conversion to new species.**

TEM was utilized to compare the structural transformation of nZnO in both media conditions and to evaluate the integrity of the crystal lattice, formation of particle aggregates, as well as amorphous species. The high-resolution TEM image in Figure 2.1 demonstrates that the as-prepared nZnO crystal lattice terminates at the crystal boundary with no amorphous species or coating present. In contrast, amorphous species are seen when nZnO is exposed to cellular media with or without HEPES as early as the 2 h time point (Figure 2.9). From our FTIR and XPS studies, the amorphous species formed in both cases is a mixture of proteins, zinc phosphates, and carbonates. Interestingly, the morphological formation of the amorphous species is radically different due to the exclusion of HEPES in RPMI media.

The samples incubated in media containing HEPES show rapid degradation of the spherical aggregates, making the particles appear more porous. Over the 24 h period,

particle integrity is lost (Figure 2.9), and pieces of aggregates are seen with amorphous material spread throughout. The high resolution TEM images (see Supporting Information, Figure S2.11) reveal individual ZnO crystals embedded within the amorphous material. Lower magnification TEM images (Figure 2.9; additional figures in Supporting Information, Figure S2.11) show pieces that have broken off from the aggregates and formation of precipitates retaining aggregates/pieces with irregular morphologies.

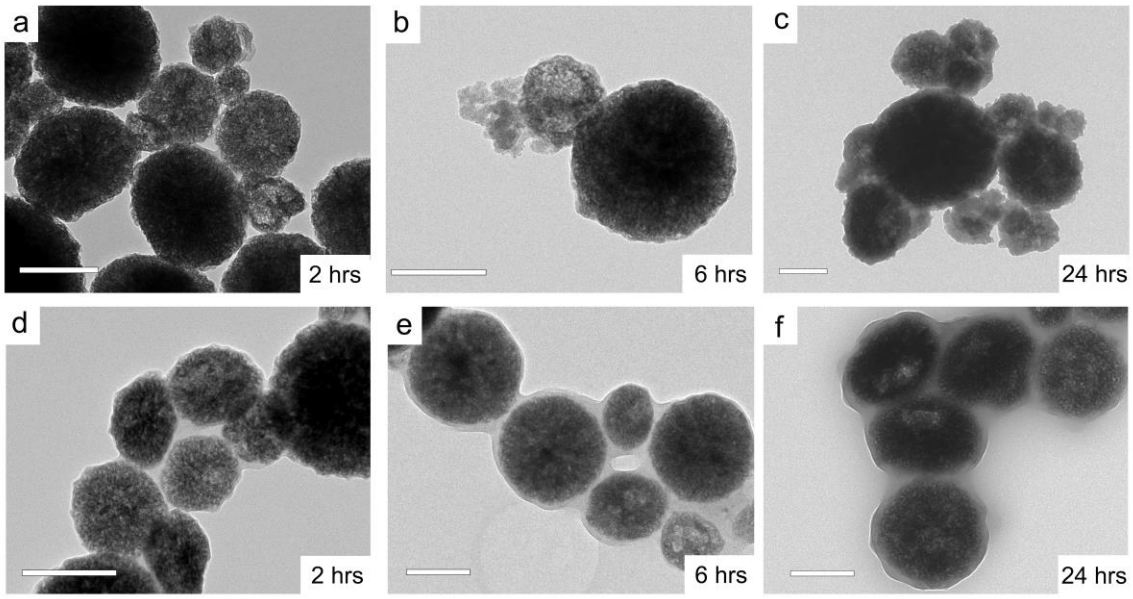


**Figure 2.9 (a)- (f) Scale bars: 200 nm. (a)-(c) TEM images of nZnO in RPMI containing HEPES. Over 24 hours, integrity of the particles is lost, with increasing porosity and portions of nZnO aggregates breaking off and amorphous material embedded in the particles (additional HRTEM images in supporting information). (d)- (f) TEM images of nZnO in RPMI excluding HEPES. Porosity is seen to increase over the 24 hours, however the proteins and amorphous zinc phosphate/carbonate form a matrix around the aggregates binding numerous particles together instead of embedding between the nZnO crystals in the aggregate.**

Even though FT-IR and XPS demonstrated similar species composition in both media conditions, the transformation of nZnO was very different when HEPES was omitted from the media. Similar structures were seen in both media compositions for

individual nZnO aggregates, but large fractions of the samples had very different morphologies. Interestingly, instead of the rapid degradation of the aggregates seen in the presence of HEPES, the absence of HEPES allows for the amorphous species to form a matrix/corona around the particles (Figure 2.9). With many particles bound together, this feature impacts their dispersion stability and rapidly settle out of solution. The porosity of the particles increases over 24 h; however, it appears to be less dramatic when HEPES is absent with more of the spherical nature of the aggregates retained. The high-resolution TEM images (see Supporting Information, Figure S2.11) demonstrate a higher density of nZnO nanocrystals in the aggregates, and the amorphous species coat the particles instead of being randomly distributed throughout the interior of the aggregates.

Taken together, these results demonstrate that HEPES affects the dissolution and structural morphology of nZnO in complex media conditions. Inclusion of HEPES or any of the Good's buffers evaluated likely impacts particle characterization and toxicity results and may therefore contribute to discrepancies in the literature regarding nZnO toxicity. With this is mind, we investigated how inclusion of HEPES in RPMI media impacts the cytotoxicity of nZnO.

Viability

The cytotoxic effects of nZnO on Jurkat leukemic cells have been reported by numerous groups and the source of toxicity attributed to both dissolution properties and ROS generation.[20,35,57] ROS generation may be inherent to nZnO from surface layer defects such as oxygen vacancies and elevated ROS levels have been associated with increased cytotoxicity in leukemic cell lines.[22] Direct interactions of nZnO with the mitochondrial membrane has also been shown to lead to increased ROS production.[23]

Additionally, ROS can also be generated due to significant release of zinc ions by inducing mitochondrial membrane leakage and subsequent increases in intracellular superoxide levels, or possibly as a byproduct of the cell death process itself.[20]

Dissolution-related cytotoxicity has been attributed to high extracellular free zinc ion concentrations and rapid intracellular dissolution in low pH environments such as endocytic vesicle fusion with lysosomes.[10] Inclusion of HEPES causes an increase in the dissolution rate of nZnO and alters the NP surface structure and morphology, all of which could influence dispersion stability, zinc ion homeostasis, and ROS generation. With this in mind, investigations were performed to understand what influence the inclusion of HEPES has on the viability profile of Jurkat leukemic cells when challenged with nZnO.

Cells were treated with nZnO for 24 h and viability determined using both flow cytometry and the Alamar Blue assay. Zinc chloride was used as a control to assess the toxicity of free zinc in the media. The Alamar Blue assay assesses the viability of live cells based on their ability to metabolically convert resazurin into a fluorescent signal. Significant changes ($p < 0.001$) in viability were observed due to the exclusion of HEPES from the media (Figure 2.10). This could be attributed to potentially three different characteristics: (i) a more rapid release of free zinc ions into the media when HEPES is present, (ii) differences in surface structure/chemistry affecting ROS production, and (iii) increased sedimentation of the NPs when bound together by the complex matrix when excluding HEPES. The toxicity profile of the zinc chloride control was similar in trend to cells treated with nZnO in RPMI/HEPES media. This suggests that the initially higher free zinc concentration due to the inclusion of HEPES may be a significant contributor to the toxicity mechanism.

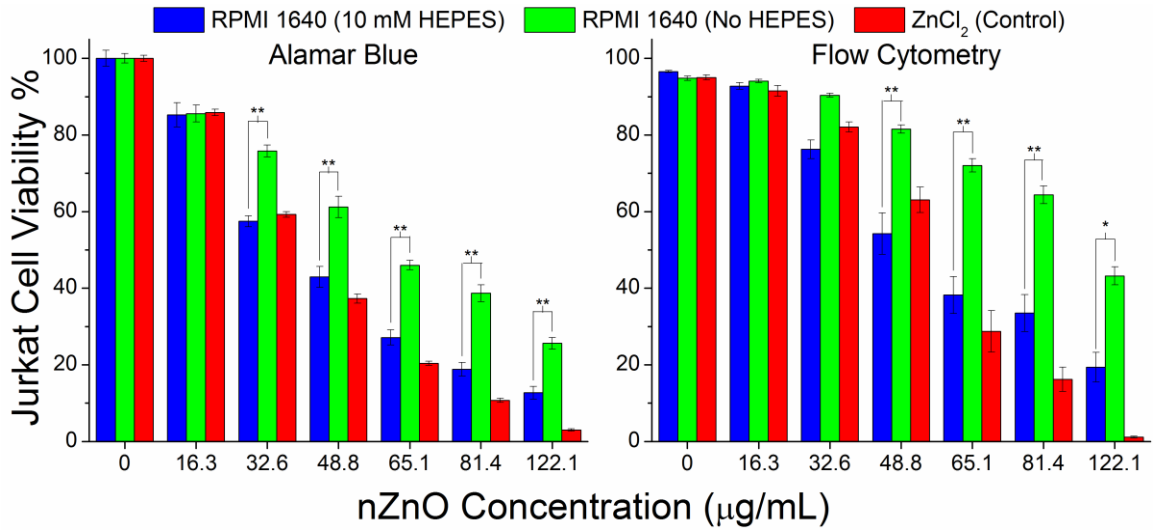


**Figure 2.10 nZnO toxicity on Jurkat leukemic cells at 24 hours. (Left) Alamar Blue assay demonstrating a significant difference in the toxicity of nZnO in media containing HEPES vs no HEPES. (Right) Flow cytometry analysis confirms significant changes to the viability of Jurkat cells when challenged with nZnO. (** indicates p< 0.001; * indicates p< 0.05).**

To verify the experimental results, viability was also determined by the uptake of propidium iodide (PI) using flow cytometry. In contrast to the Alamar Blue assay, the uptake of PI labels late apoptotic/necrotic cells by intercalating between DNA base pairs when membrane integrity is lost; thus, analysis is based upon the number of dead cells in the population. A significant difference ($p < 0.001$ for 3 conc.; $p < 0.05$ for 1 conc.) in the viability of Jurkat cells was observed between the two media types (Figure 2.10). The zinc chloride control again had a similar toxicity profile when compared to the media containing HEPES; however, at higher concentrations, the zinc chloride appears more toxic. Assuming dissolution is the key driver of toxicity, this is expected since the free zinc concentration does not reach equilibrium in nZnO treated media until at least the 6 h time point (Figure 2.5) and nZnO crystals are still detectable after the 24 h time course.

## Discussion

This paper demonstrates the ability to use simple, relatively fast, and cost-effective methods to quantitatively evaluate real-time dissolution kinetics of nZnO in aqueous solutions. These methods, using UV/vis or a spectrofluorometer, could potentially be adapted for use in more complex situations such as in wastewater treatment studies or screenings in other biologically relevant solutions. This work also highlights that screening interactions in simple solutions can be expanded to more complex situations, leading to a better fundamental understanding of how nZnO behaves in model systems that may impact nZnO dissolution, structural transformation, dispersion, and cytotoxicity profile.

The dissolution of nZnO is regarded as a significant source of cytotoxicity and a more complete understanding how nonessential media components such as Good's buffers contribute to the dissolution kinetics may help in deciphering reports on nZnO toxicity. Good's buffers are used extensively in biological studies to maintain physiological pH and have been reported to be used in characterizations studies such as in imaging buffers. The high level of dissolution induced by these buffers may impact results and evaluations at all levels of nZnO assessments, and the impact of utilizing Good's buffers as a buffering system needs to be considered prior to use.

The structural and chemical transformation of nZnO has been shown to be influenced by the concentration of carbonates and phosphates in solution.[29,31] Here we demonstrate that excluding HEPES from the media significantly alters these transformations. From basic chemical assessments, it appeared that there were modest changes in the dynamics of converting nZnO into zinc phosphate and zinc carbonate.

However, the matrix formation that appeared in HEPES-free media suggests that even though chemically similar, structural changes can be dramatic. These structural changes potentially alter nZnO dispersion stability, causing significant changes in their sedimentation profiles. We have previously shown how dispersion stability can greatly impact the cytotoxic profile of nZnO.[58] Understanding the transformation of nZnO in in vitro model systems will help in further determinations on the toxicity of nZnO.

From these studies, we further demonstrated that the difference in the dissolution kinetics and transformation have significant impacts on nZnO toxicity profile in Jurkat leukemic cells. These studies highlight that the observed toxicity profile of nZnO stems from more than just the physicochemical properties of the NP. Nanoscale ZnO interactions with the environment can significantly alter their characteristics and conflicting reports on their toxicity mechanism could potentially be due to the media composition. For our future studies, we plan to investigate the use of phosphate free and HEPES free Dulbecco's modified Eagle medium in place of RPMI 1640 media for toxicity assessments to avoid potential artifacts arising from the transformation of nZnO from phosphate and increased dissolution observed from Good's buffers.

In conclusion, we have shown that a relatively simple, fast, and cost-effective method for screening the dissolution of nZnO can lead to a more thorough understanding of how nZnO behaves in complex conditions. These results also indicate the need for authors to ensure they list all details of the buffering systems used in published studies on nZnO due to the various media compositions required for various cell types and the wide use of Good's buffers in characterization studies such as imaging solutions.

## Associated Content

Supporting Information

The Supporting Information is available free of charge on the ACS Publications website at DOI: 10.1021/acs.chemrestox.7b00136. Confocal microscopy time-lapsed video (AVI) UV/vis and spectrofluorometric monitoring of dissolution; cellular media component screening; X-ray diffraction; FTIR nZnO vs controls; X-ray photoelectron spectroscopy control; high-resolution TEM images; additional morphological TEM images (PDF)

## Author Information

Corresponding Author

*E-mail: denisewingett@boisestate.edu. Phone: 208-426-2921. Fax: 208-392-1430. ORCID

Denise G. Wingett: 0000-0002-1784-9065

Funding

This research was supported in part by NSF-MRI awards (Nos. 032.233, 0722699, 0521315), NSF-RUI (DMR-0840227), and NIH (1R15CA141358−01). We also acknowledge support from the Biomolecular Research Center at Boise State University, COBRE, and INBRE with funding from the NIH Grant Nos. P20GM103408 and P20GM109095, NSF (Nos. 0619793, 0923535), the MJ Murdock Charitable Trust, and the Idaho State Board of Education.

Notes

The authors declare no competing financial interest.

## Supporting Information

Supporting Information Content

UV/vis and spectrofluorometric monitoring of dissolution, Cellular media component screening, X-ray diffraction, FTIR nZnO vs Controls, X-ray photoelectron spectroscopy control, High-resolution TEM images, additional morphological TEM images and description of time-lapsed video

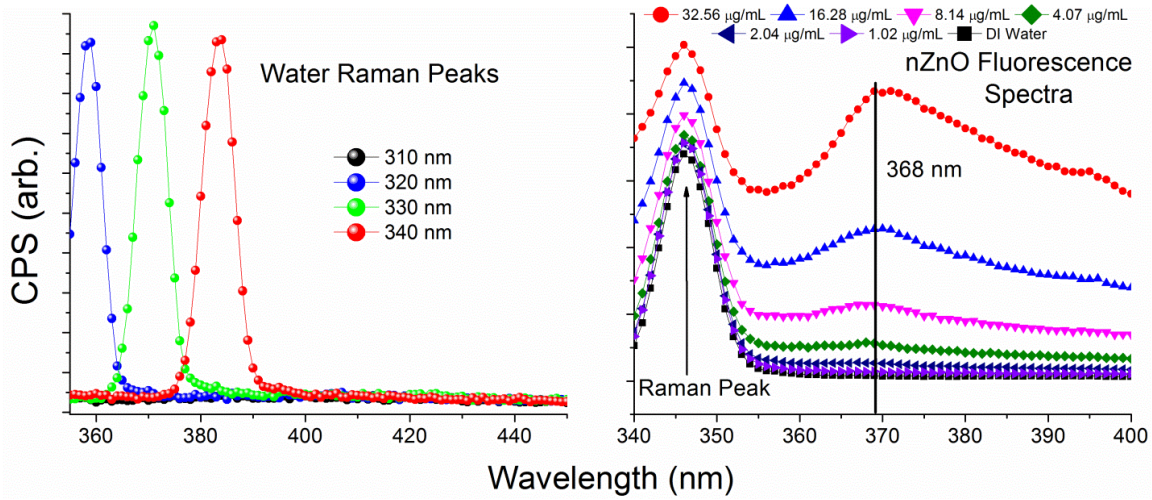


**Figure S2.1 Spectrofluorometric data of nZnO. (left) Raman peaks associated with water appear in the same region as the nZnO fluorescence peak when using a higher wavelength as the excitation source. A 310 nm excitation was chosen to prevent convolution of the nZnO fluorescence peak with the Raman peak. (right) The fluorescence spectra of nZnO at various concentrations using a 310 nm excitation source. The peak intensity at 368 nm was used to monitor nZnO dissolution and convert counts per second (CPS) to concentration.**

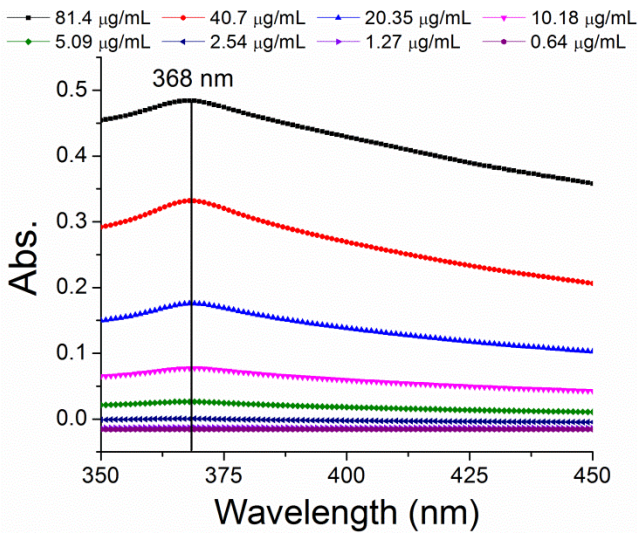


**Figure S2.2 UV/vis data of nZnO. Example absorbance spectra of nZnO for various concentrations, demonstrating the max absorbance at 368 nm. The peak intensity value at 368 nm was used to convert nZnO absorbance to concentration for dissolution studies.**

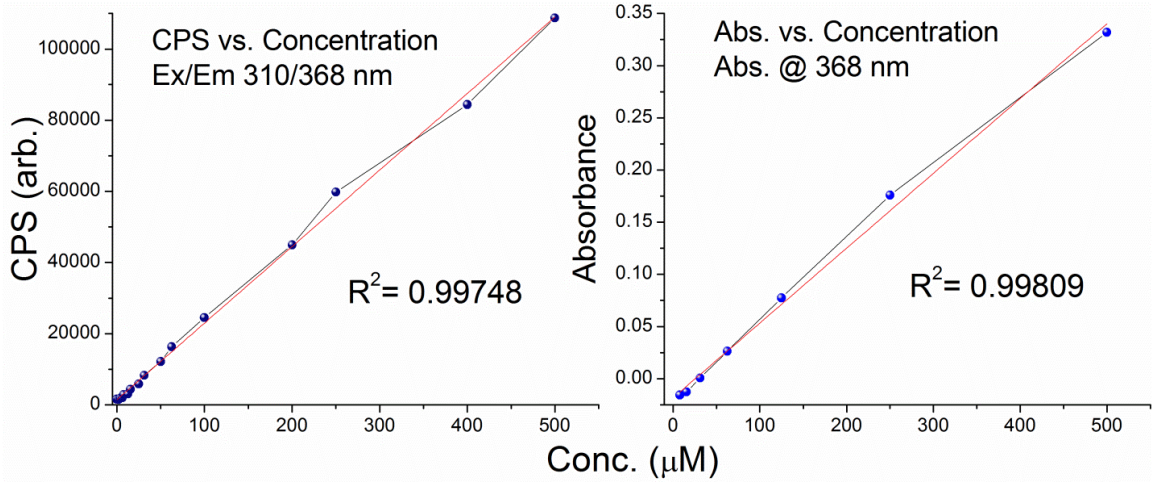


**Figure S2.3 Plots of fluorescence (left) and absorbance (right) vs. concentration. There is a high linear correlation between nZnO CPS/Abs. and concentration up to 500 μM (40.7 μg/mL), allowing simple conversion for real-time quantitative analysis of nZnO dissolution.**

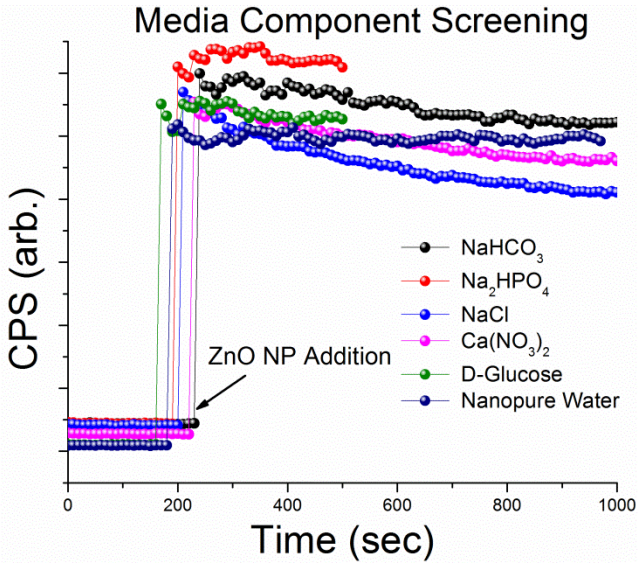


**Figure S2.4 Screening of multiple media components at biologically relevant concentrations (obtained from ATCC product data sheet for RPMI 1640 medium; product # 30-2001) demonstrate high stability of nZnO (40.7 µg/mL) in various solutions. The slow decrease in CPS for these solutions is likely due to sedimentation of nZnO.**

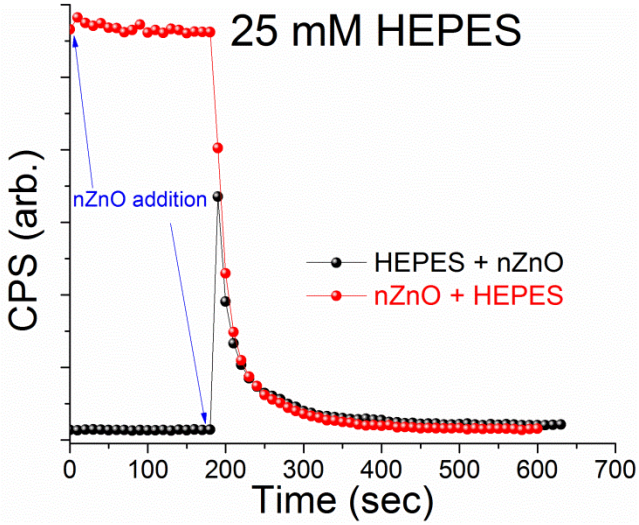


**Figure S2.5 Rapid dissolution of nZnO (40.7 µg/mL) in 25 mM HEPES buffer. Adding nZnO to the solution already containing HEPES (black) never achieved the CPS expected for the concentration used. Switching the approach (red) by suspending nZnO in solution and then adding the buffer shows the same kinetics profile but retains the information lost during the time of addition. All subsequent experiments suspended nZnO in solution first, then added buffer to retain all dissolution kinetics information.**

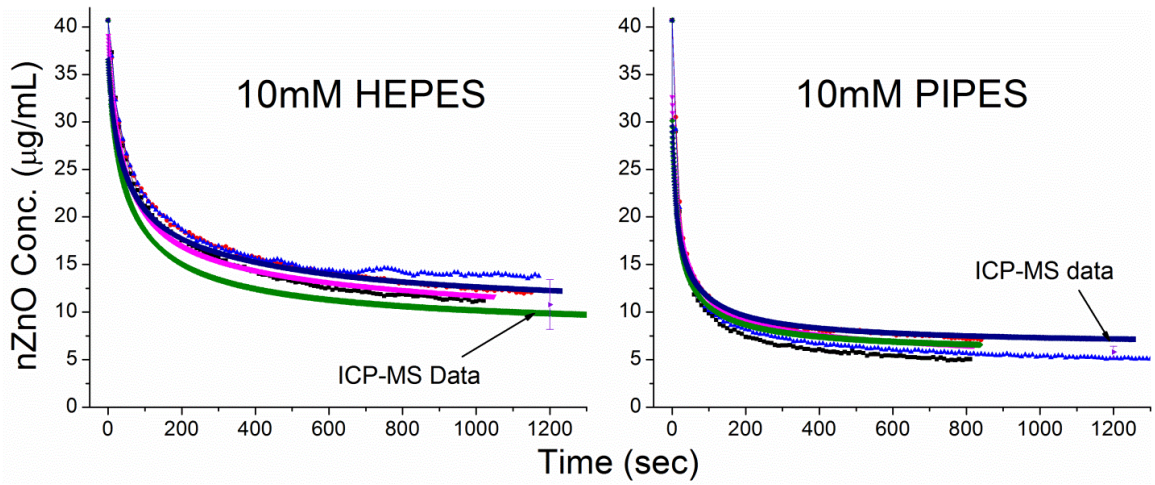


**Figure S2.6 Two examples of triplicated measurements of nZnO (40.7 µg/mL) in Good's buffers. CPS and Abs. were converted into concentration by using the linear correlation in Figure S3. Triplicate of fluorescence and absorbance measurements are plotted (n=6) for each buffer demonstrating both methods are highly reproducible, consistent, and accurate. ICP-MS was utilized to confirm the accuracy of converting spectra information to concentration.**

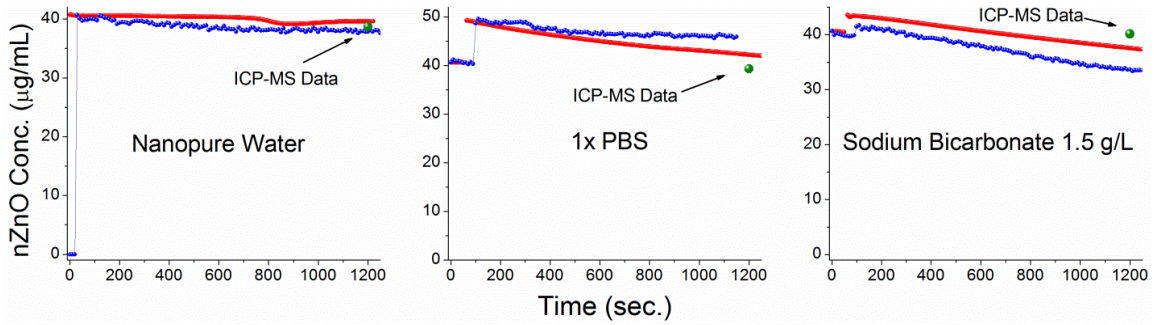


**Figure S2.7 Additional representative plots of nZnO (40.7 µg/mL) in nanopure water, phosphate buffered saline (PBS) and sodium bicarbonate. nZnO is stable in nanopure water over the 20 minute time course demonstrating kinetics is due to interactions with the media components. Interestingly, in both PBS and sodium bicarbonate, the apparent concentration of nZnO increased upon addition of the buffer. This is likely due to formation of zinc phosphates and zinc carbonates respectively, causing an increase in both absorbance and fluorescence measurements.**

Characterization

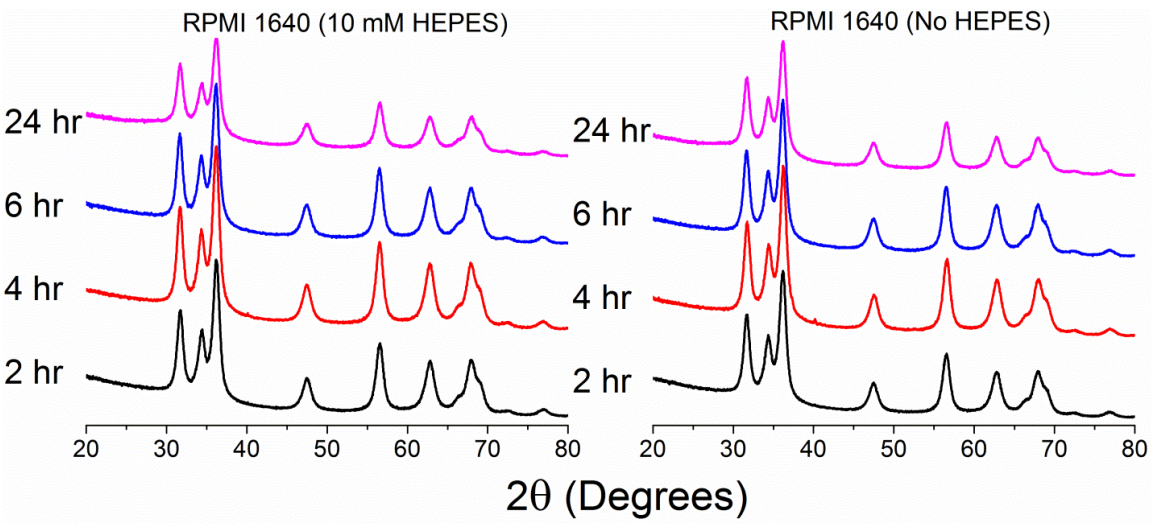


**Figure S2.8 XRD spectra of nZnO (40.7 µg/mL) post incubation in RPMI 1640 cellular media at various time points. In both conditions (with and without 10 mM HEPES) only the wurzite crystal phase of ZnO was detected over the 24 hour time course. No peaks from zinc phosphate or zinc carbonate were detected, however in both cases the calculated average crystal size reduced from ~9.3 nm to ~7.5 nm.**

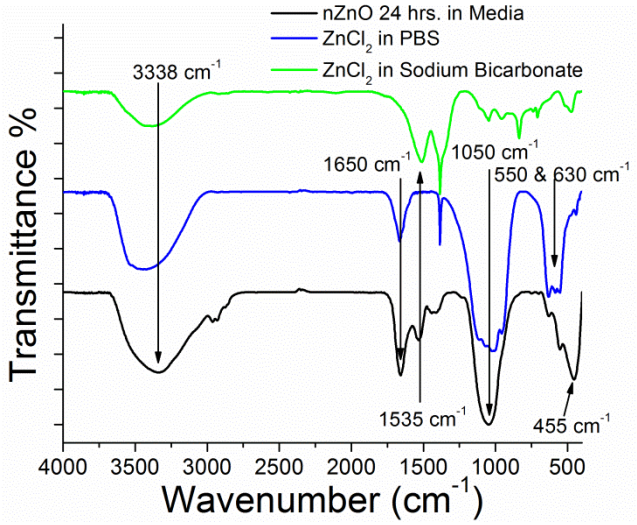


**Figure S2.9 FTIR spectra of nZnO incubated in RPMI cellular media for 24 hours and precipitate collected from 50mM $ZnCl_2$ solution dispersed in phosphate buffered saline (PBS) or sodium bicarbonate. The Zn-O modes at 455 $cm^{-1}$ are not present in the zinc carbonate/phosphate precipitant. Spectra of the controls confirms peak positions in literature that attribute the 550, 630, and 1050 $cm^{-1}$ peaks to $PO_4^{3-}$**

**bending/stretching modes, 1650 $cm^{-1}$ to crystalline water and 1535 $cm^{-1}$ to C=O stretching from carbonate.**

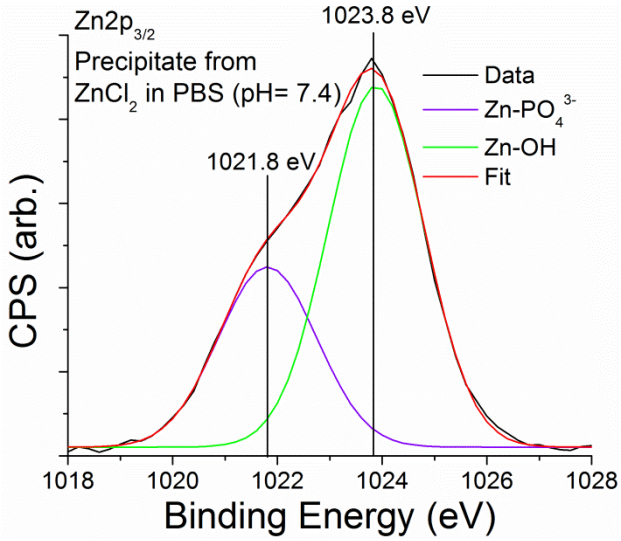


**Figure S2.10 Core level XPS spectra of the $Zn2p_{3/2}$ region. $ZnCl_2$ solution was dispersed in PBS (pH= 7.4) and the precipitate was collected via centrifugation and subsequently dried for 24 hours. Peak deconvolution demonstrates two zinc species with a chemical shift of ~2.0 eV attributed to Zn- $PO_4^{3-}$ and Zn-OH.**

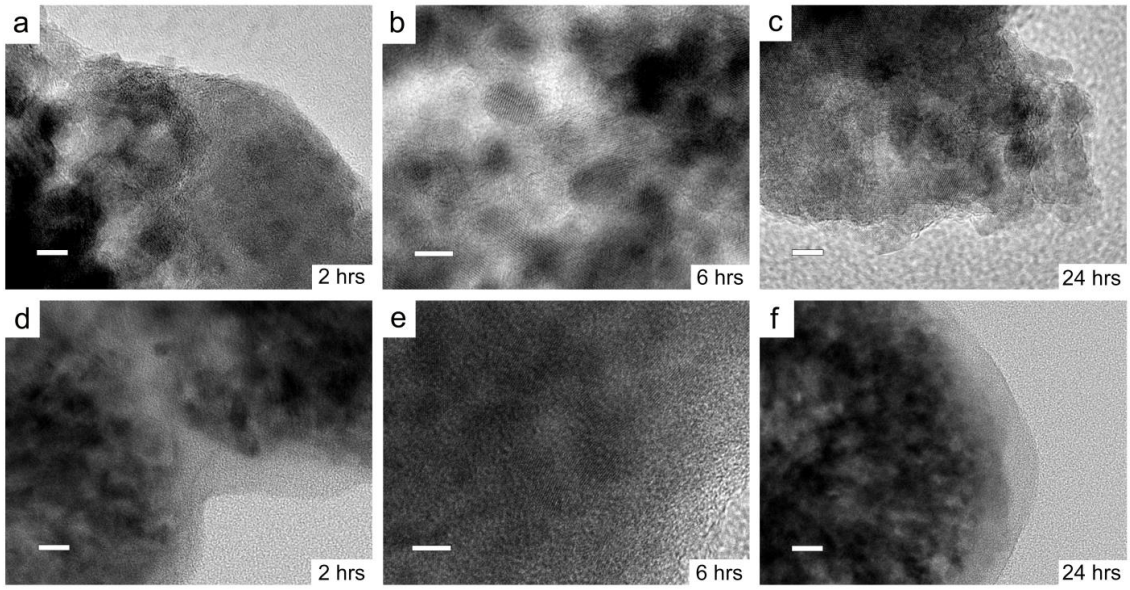


**Figure S2.11 HRTEM images of nZnO post incubation in RPMI 1640 with (a)-(c) and without 10 mM HEPES (d)-(f). (a)-(c) scale bar: 5 nm; Images show pieces of irregular shaped nZnO aggregates. Porosity of the aggregates increased and the amorphous zinc phosphate/carbonates are spread throughout with individual nZnO crystals embedded. Scale bars: 10 nm (d), 5 nm (e) and 20 nm (f). (d)-(f) nZnO images show the amorphous precipitants forming a matrix on the exterior of the aggregates, binding the particles together. The HRTEM images show the individual nZnO crystals comprising the aggregates are more densely packed than in the media containing HEPES (top row). It appears the slower dissolution rate in HEPES free media causes the precipitants to form on the exterior of the aggregates instead of causing loss of particle integrity, resulting in higher porosity and causing pieces of aggregates to separate from the particle.**

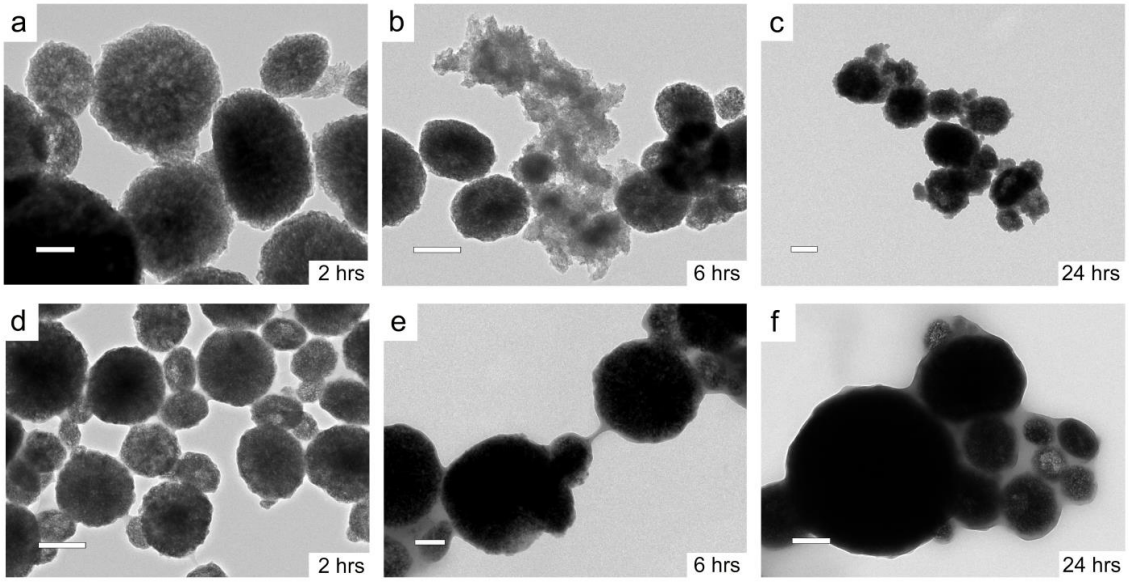


**Figure S2.12 Scale bars: 200 nm except (a) and (e) (100 nm). Additional images of nZnO incubated in media with (a-c) and without (d-f) 10 mM HEPES at 2, 6 and 24 hours. (a)-(c) Irregular shaped precipitants are seen in media containing HEPES and the spherical shape of the aggregates is lost over the time course. (d)-(f) Matrix formation around the particles is seen when omitting HEPES from the media. Many aggregates are bound together and particles appear to retain their spherical morphology. This would impact the dispersion stability of the nanoparticles and formation of precipitants (top row) may contribute to the overall toxicity profile of nZnO in viability assessments.**

Web Enhanced Object

(See materials and methods for experimental details) Confocal microscopy time-lapsed video demonstrates the dissolution of nZnO upon the addition of HEPES. The first part of the video shows nZnO in nanopure water as a control to ensure any changes to nZnO wasn't due to dissolution or solubility in water. Upon addition of HEPES, the majority of nZnO disappears from view. Link: http://pubs.acs.org/doi/suppl/10.1021/acs.chemrestox.7b00136/suppl_file/tx7b00136_si_001.avi

## References

1. Kim, J. S.; Kuk, E.; Yu, K. N.; Kim, J. H.; Park, S. J.; Lee, H. J.; Kim, S. H.; Park, Y. K.; Park, Y. H.; Hwang, C. Y.; Kim, Y. K.; Lee, Y. S.; Jeong, D. H.; Cho, M. H., Antimicrobial effects of silver nanoparticles. *Nanomedicine-Nanotechnology Biology and Medicine* **2007,** *3* (1), 95-101.

2. Hoye, R. L. Z.; Musselman, K. P.; MacManus-Driscoll, J. L., Research Update: Doping ZnO and TiO2 for solar cells. *Apl Materials* **2013,** *1* (6), 11.

3. Sepulveda, B.; Angelome, P. C.; Lechuga, L. M.; Liz-Marzan, L. M., LSPR-based nanobiosensors. *Nano Today* **2009,** *4* (3), 244-251.

4. Becheri, A.; Durr, M.; Lo Nostro, P.; Baglioni, P., Synthesis and characterization of zinc oxide nanoparticles: application to textiles as UV-absorbers. *Journal of Nanoparticle Research* **2008,** *10* (4), 679-689.

5. Seo, Y. K.; Kumar, S.; Kim, G. H., Analysis of Assembling ZnO Nanoparticles Into Nanogap Electrodes for Nanoscale Electronic Device Applications. *Journal of Nanoscience and Nanotechnology* **2011,** *11* (6), 4852-4862.

6. Zvyagin, A. V.; Zhao, X.; Gierden, A.; Sanchez, W.; Ross, J. A.; Roberts, M. S., Imaging of zinc oxide nanoparticle penetration in human skin in vitro and in vivo. *Journal of Biomedical Optics* **2008,** *13* (6), 9.

7. Smijs, T. G. M.; Bouwstra, J. A., Focus on Skin as a Possible Port of Entry for Solid Nanoparticles and the Toxicological Impact. *Journal of Biomedical Nanotechnology* **2010,** *6* (5), 469-484.

8. Sharma, V.; Shukla, R. K.; Saxena, N.; Parmar, D.; Das, M.; Dhawan, A., DNA damaging potential of zinc oxide nanoparticles in human epidermal cells. *Toxicology Letters* **2009,** *185* (3), 211-218.

9. Nair, S.; Sasidharan, A.; Rani, V. V. D.; Menon, D.; Manzoor, K.; Raina, S., Role of size scale of ZnO nanoparticles and microparticles on toxicity toward bacteria and osteoblast cancer cells. *Journal of Materials Science-Materials in Medicine* **2009,** *20*, 235-241.

10. Muller, K. H.; Kulkarni, J.; Motskin, M.; Goode, A.; Winship, P.; Skepper, J. N.; Ryan, M. P.; Porter, A. E., pH-Dependent Toxicity of High Aspect Ratio ZnO Nanowires in Macrophages Due to Intracellular Dissolution. *Acs Nano* **2010,** *4* (11), 6767-6779.

11. Kumar, A.; Pandey, A. K.; Singh, S. S.; Shanker, R.; Dhawan, A., Engineered ZnO and TiO2 nanoparticles induce oxidative stress and DNA damage leading to reduced viability of Escherichia coli. *Free Radical Biology and Medicine* **2011,** *51* (10), 1872-1881.

12. Saptarshi, S. R.; Duschl, A.; Lopata, A. L., Biological reactivity of zinc oxide nanoparticles with mammalian test systems: an overview. *Nanomedicine* **2015,** *10* (13), 2075-2092.

13. Gottschalk, F.; Sonderer, T.; Scholz, R. W.; Nowack, B., Modeled Environmental Concentrations of Engineered Nanomaterials (TiO2, ZnO, Ag, CNT, Fullerenes) for Different Regions. *Environmental Science & Technology* **2009,** *43* (24), 9216-9222.

14. Jiang, J. K.; Oberdorster, G.; Biswas, P., Characterization of size, surface charge, and agglomeration state of nanoparticle dispersions for toxicological studies. *Journal of Nanoparticle Research* **2009,** *11* (1), 77-89.

15. Yang, H.; Liu, C.; Yang, D. F.; Zhang, H. S.; Xi, Z. G., Comparative study of cytotoxicity, oxidative stress and genotoxicity induced by four typical nanomaterials: the role of particle size, shape and composition. *Journal of Applied Toxicology* **2009,** *29* (1), 69-78.

16. Xia, T.; Kovochich, M.; Liong, M.; Madler, L.; Gilbert, B.; Shi, H. B.; Yeh, J. I.; Zink, J. I.; Nel, A. E., Comparison of the Mechanism of Toxicity of Zinc Oxide and Cerium Oxide Nanoparticles Based on Dissolution and Oxidative Stress Properties. *Acs Nano* **2008,** *2* (10), 2121-2134.

17. Punnoose, A.; Dodge, K.; Rasmussen, J. W.; Chess, J.; Wingett, D.; Anders, C., Cytotoxicity of ZnO Nanoparticles Can Be Tailored by Modifying Their Surface

Structure: A Green Chemistry Approach for Safer Nanomaterials. *Acs Sustainable Chemistry & Engineering* **2014,** *2* (7), 1666-1673.

18. Xie, Y. P.; He, Y. P.; Irwin, P. L.; Jin, T.; Shi, X. M., Antibacterial Activity and Mechanism of Action of Zinc Oxide Nanoparticles against Campylobacter jejuni. *Applied and Environmental Microbiology* **2011,** *77* (7), 2325-2331.

19. Akhtar, M. J.; Ahamed, M.; Kumar, S.; Khan, M. A. M.; Ahmad, J.; Alrokayan, S. A., Zinc oxide nanoparticles selectively induce apoptosis in human cancer cells through reactive oxygen species. *International Journal of Nanomedicine* **2012,** *7*, 845-857.

20. Kao, Y. Y.; Chen, Y. C.; Cheng, T. J.; Chiung, Y. M.; Liu, P. S., Zinc Oxide Nanoparticles Interfere With Zinc Ion Homeostasis to Cause Cytotoxicity. *Toxicological Sciences* **2012,** *125* (2), 462-472.

21. Sharma, V.; Anderson, D.; Dhawan, A., Zinc oxide nanoparticles induce oxidative DNA damage and ROS-triggered mitochondria mediated apoptosis in human liver cells (HepG2). *Apoptosis* **2012,** *17* (8), 852-870.

22. Shen, C. C.; James, S. A.; de Jonge, M. D.; Turney, T. W.; Wright, P. F. A.; Feltis, B. N., Relating Cytotoxicity, Zinc Ions, and Reactive Oxygen in ZnO NanoparticleExposed Human Immune Cells. *Toxicological Sciences* **2013,** *136* (1), 120-130.

23. Jeng, H. A.; Swanson, J., Toxicity of metal oxide nanoparticles in mammalian cells. *Journal of Environmental Science and Health Part a-Toxic/Hazardous Substances & Environmental Engineering* **2006,** *41* (12), 2699-2711.

24. Hanley, C.; Thurber, A.; Hanna, C.; Punnoose, A.; Zhang, J. H.; Wingett, D. G., The Influences of Cell Type and ZnO Nanoparticle Size on Immune Cell Cytotoxicity and Cytokine Induction. *Nanoscale Research Letters* **2009,** *4* (12), 1409-1420.

25. David, C. A.; Galceran, J.; Rey-Castro, C.; Puy, J.; Companys, E.; Salvador, J.; Monne, J.; Wallace, R.; Vakourov, A., Dissolution Kinetics and Solubility of ZnO Nanoparticles Followed by AGNES. *Journal of Physical Chemistry C* **2012,** *116* (21), 11758-11767.

26. Misra, S. K.; Dybowska, A.; Berhanu, D.; Luoma, S. N.; Valsami-Jones, E., The complexity of nanoparticle dissolution and its importance in nanotoxicological studies. *Science of the Total Environment* **2012,** *438*, 225-232.

27. Mudunkotuwa, I. A.; Rupasinghe, T.; Wu, C. M.; Grassian, V. H., Dissolution of ZnO Nanoparticles at Circumneutral pH: A Study of Size Effects in the Presence and Absence of Citric Acid. *Langmuir* **2012,** *28* (1), 396-403.

28. Bian, S. W.; Mudunkotuwa, I. A.; Rupasinghe, T.; Grassian, V. H., Aggregation and Dissolution of 4 nm ZnO Nanoparticles in Aqueous Environments: Influence of pH, Ionic Strength, Size, and Adsorption of Humic Acid. *Langmuir* **2011,** *27* (10), 6059-6068.

29. Mu, Q. S.; David, C. A.; Galceran, J.; Rey-Castro, C.; Krzeminski, L.; Wallace, R.; Bamiduro, F.; Milne, S. J.; Hondow, N. S.; Brydson, R.; Vizcay-Barrena, G.; Routledge, M. N.; Jeuken, L. J. C.; Brown, A. P., Systematic Investigation of the Physicochemical Factors That Contribute to the Toxicity of ZnO Nanoparticles. *Chemical Research in Toxicology* **2014,** *27* (4), 558-567.

30. Reed, R. B.; Ladner, D. A.; Higgins, C. P.; Westerhoff, P.; Ranville, J. F., Solubility of nano-zinc oxide in environmentally and biologically important matrices. *Environmental Toxicology and Chemistry* **2012,** *31* (1), 93-99.

31. Lv, J. T.; Zhang, S. Z.; Luo, L.; Han, W.; Zhang, J.; Yang, K.; Christie, P., Dissolution and Microstructural Transformation of ZnO Nanoparticles under the Influence of Phosphate. *Environmental Science & Technology* **2012,** *46* (13), 7215-7221.

32. Nel, A. E.; Madler, L.; Velegol, D.; Xia, T.; Hoek, E. M. V.; Somasundaran, P.; Klaessig, F.; Castranova, V.; Thompson, M., Understanding biophysicochemical interactions at the nano-bio interface. *Nature Materials* **2009,** *8* (7), 543-557.

33. Herrmann, R.; Garcia-Garcia, F. J.; Reller, A., Rapid degradation of zinc oxide nanoparticles by phosphate ions. *Beilstein Journal of Nanotechnology* **2014,** *5*, 2007-2015.

34. Zhang, J. Z.; He, X.; Zhang, P.; Ma, Y. H.; Ding, Y. Y.; Wang, Z. Y.; Zhang, Z. Y., Quantifying the dissolution of nanomaterials at the nano-bio interface. *Science China-Chemistry* **2015,** *58* (5), 761-767.

35. Hanley, C.; Layne, J.; Punnoose, A.; Reddy, K. M.; Coombs, I.; Coombs, A.; Feris, K.; Wingett, D., Preferential killing of cancer cells and activated human T cells using ZnO nanoparticles. *Nanotechnology* **2008,** *19* (29), 10.

36. Hochberg, Y., A Sharper Bonferroni Procedure For Multiple Tests Of Significance. *Biometrika* **1988,** *75* (4), 800-802.

37. Rathnayake, S.; Unrine, J. M.; Judy, J.; Miller, A. F.; Rao, W.; Bertsch, P. M., Multitechnique Investigation of the pH Dependence of Phosphate Induced Transformations of ZnO Nanoparticles. *Environmental Science & Technology* **2014,** *48* (9), 4757-4764.

38. Keller, A. A.; Wang, H. T.; Zhou, D. X.; Lenihan, H. S.; Cherr, G.; Cardinale, B. J.; Miller, R.; Ji, Z. X., Stability and Aggregation of Metal Oxide Nanoparticles in Natural Aqueous Matrices. *Environmental Science & Technology* **2010,** *44* (6), 1962-1967.

39. Good, N. E.; Winget, G. D.; Winter, W.; Connolly, T. N.; Izawa, S.; Singh, R. M. M., Hydrogen Ion Buffers For Biological Research. *Biochemistry* **1966,** *5* (2), 467-&.

40. Turney, T. W.; Duriska, M. B.; Jayaratne, V.; Elbaz, A.; O'Keefe, S. J.; Hastings, A. S.; Piva, T. J.; Wright, P. F. A.; Feltis, B. N., Formation of Zinc-Containing Nanoparticles from Zn2+ Ions in Cell Culture Media: Implications for the Nanotoxicology of ZnO. *Chemical Research in Toxicology* **2012,** *25* (10), 2057-2066.

41. Wahab, R.; Ansari, S. G.; Kim, Y. S.; Dar, M. A.; Shin, H. S., Synthesis and characterization of hydrozincite and its conversion into zinc oxide nanoparticles. *Journal of Alloys and Compounds* **2008,** *461* (1-2), 66-71.

42. Yuan, A. Q.; Liao, S.; Tong, Z. F.; Wu, J.; Huang, Z. Y., Synthesis of nanoparticle zinc phosphate dihydrate by solid state reaction at room temperature and its thermochemical study. *Materials Letters* **2006,** *60* (17-18), 2110-2114.

43. Wang, J.; Li, D.; Liu, J.; Yang, X.; He, J.; Lu, Y., One-Step Preparation and Characterization of Zinc Phosphate Nanocrystals with Modified Surface. *Soft Nanoscience Letters*: 2011; Vol. 1, pp 81-85.

44. Pawlig, O.; Trettin, R., Synthesis and characterization of alpha-hopeite, Zn-3(Po-4)(2)center dot 4H(2)O. *Materials Research Bulletin* **1999,** *34* (12-13), 1959-1966.

45. Jung, S. H.; Oh, E.; Shim, D.; Park, D. H.; Cho, S.; Lee, B. R.; Jeong, Y. U.; Lee, K. H.; Jeong, S. H., Sonochemical Synthesis of Amorphous Zinc Phosphate Nanospheres. *Bulletin of the Korean Chemical Society* **2009,** *30* (10), 2280-2282.

46. Hales, M. C.; Frost, R. L., Synthesis and vibrational spectroscopic characterisation of synthetic hydrozincite and smithsonite. *Polyhedron* **2007,** *26* (17), 4955-4962.

47. Cheng, J. Q.; Poduska, K. M., A Strategy for Hydroxide Exclusion in Nanocrystalline Solid-State Metathesis Products. *Nanomaterials* **2013,** *3* (3), 317-324.

48. Kanari, N.; Mishra, D.; Gaballah, I.; Dupre, B.; Mineral Processing Environm, E., Thermal decomposition of zinc carbonate hydroxide. *Thermochimica Acta* **2004,** *410* (1-2), 93-100.

49. Kong, J.; Yu, S., Fourier transform infrared spectroscopic analysis of protein secondary structures. *Acta Biochimica Et Biophysica Sinica* **2007,** *39* (8), 549-559.

50. Barth, A., Infrared spectroscopy of proteins. *Biochimica Et Biophysica Acta-Bioenergetics* **2007,** *1767* (9), 1073-1101.

51. Sahai, A.; Goswami, N., Structural and vibrational properties of ZnO nanoparticles synthesized by the chemical precipitation method. *Physica E-Low-Dimensional Systems & Nanostructures* **2014,** *58*, 130-137.

52. Decremps, F.; Pellicer-Porres, J.; Saitta, A. M.; Chervin, J. C.; Polian, A., High-pressure Raman spectroscopy study of wurtzite ZnO. *Physical Review B* **2002,** *65* (9), 4.

53. Wang, R. P.; Xu, G.; Jin, P., Size dependence of electron-phonon coupling in ZnO nanowires. *Physical Review B* **2004,** *69* (11), 4.

54. Munoz-Hernandez, G.; Escobedo-Morales, A.; Pal, U., Thermolytic Growth of ZnO Nanocrystals: Morphology Control and Optical Properties. *Crystal Growth & Design* **2009,** *9* (1), 297-300.

55. Verges, M. A.; Mifsud, A.; Serna, C. J., Formation Of Rod-Like Zinc-Oxide Microcrystals In Homogeneous Solutions. *Journal of the Chemical Society-Faraday Transactions* **1990,** *86* (6), 959-963.

56. Huang, Y. Y.; He, L. Z.; Liu, W.; Fan, C. D.; Zheng, W. J.; Wong, Y. S.; Chen, T. F., Selective cellular uptake and induction of apoptosis of cancer-targeted selenium nanoparticles. *Biomaterials* **2013,** *34* (29), 7106-7116.

57. Buerki-Thurnherr, T.; Xiao, L. S.; Diener, L.; Arslan, O.; Hirsch, C.; Maeder-Althaus, X.; Grieder, K.; Wampfler, B.; Mathur, S.; Wick, P.; Krug, H. F., In vitro mechanistic study towards a better understanding of ZnO nanoparticle toxicity. *Nanotoxicology* **2013,** *7* (4), 402-416.

58. Anders, C. B.; Chess, J. J.; Wingett, D. G.; Punnoose, A., Serum Proteins Enhance Dispersion Stability and Influence the Cytotoxicity and Dosimetry of ZnO Nanoparticles in Suspension and Adherent Cancer Cell Models. *Nanoscale Research Letters* **2015,** *10*, 22.

# CHAPTER THREE: ZNO NANOPARTICLES MODULATE THE IONIC TRANSPORT AND VOLTAGE REGULATION OF LYSENIN NANOCHANNELS

Sheenah L. Bryant[1,2†], Josh E. Eixenberger[1,2†], Steven Rossland[1,3], Holly Apsley[1,4], Connor Hoffmann[1,5], Nisha Shrestha[1,2], Michael McHugh[2], Alex Punnoose[1,2] and Daniel Fologea[1,2]*

[1]Department of Physics, Boise State University, Boise, ID 83725, USA. [2]Biomolecular Sciences Graduate Program, Boise State University, Boise, ID 83725, USA. [3]Present Address: Department of Physics, University of Utah, Salt Lake City, UT 84112, USA. [4]Present Address: Department of Social Sciences, Yale NUS College, Singapore 138610, Singapore. [5]Present Address: Department of Chemical and Biological Engineering, Montana State University, Bozeman, MT 59717, USA.

*Email: DanielFologea@boisestate.edu

Journal of Nanobiotechnology (2017) 15:90

https://jnanobiotechnology.biomedcentral.com/articles/10.1186/s12951-017-0327-9

DOI 10.1186/s12951-017-0327-9

Publisher Springer Nature

No significant changes were made to this publication.

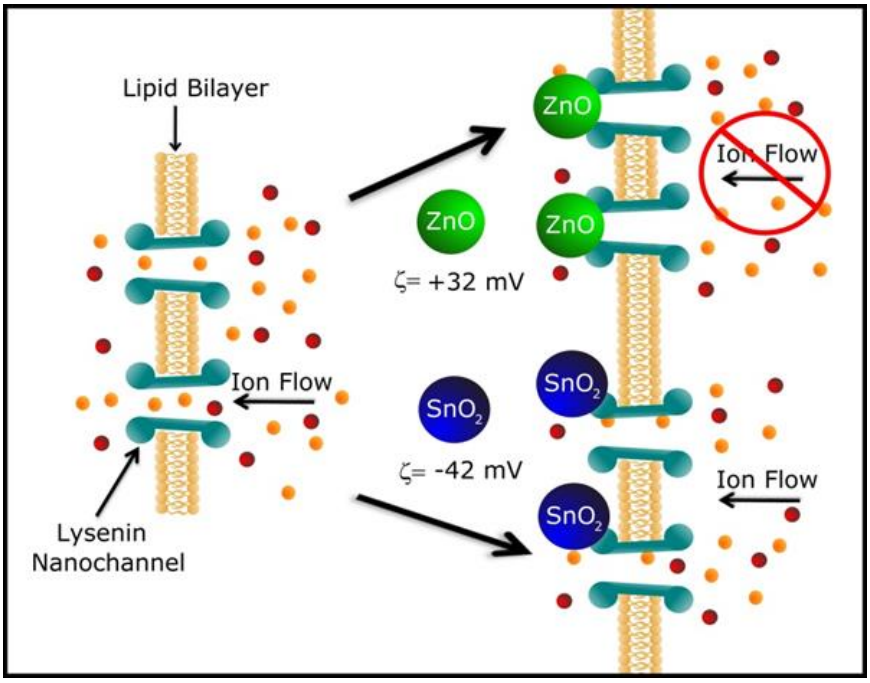



## Abstract

**Background**: The insufficient understanding of unintended biological impacts from nanomaterials (NMs) represents a serious impediment to their use for scientific, technological, and medical applications. While previous studies have focused on understanding nanotoxicity effects mostly resulting from cellular internalization, recent work indicates that NMs may interfere with transmembrane transport mechanisms, hence enabling contributions to nanotoxicity by affecting key biological activities dependent on transmembrane transport. In this line of inquiry, we investigated the effects of charged nanoparticles (NPs) on the transport properties of lysenin, a pore-forming toxin that shares fundamental features with ion channels such as regulation and high transport rate.

**Results**: The macroscopic conductance of lysenin channels greatly diminished in the presence of cationic ZnO NPs. The inhibitory effects were asymmetrical relative to

the direction of the electric field and addition site, suggesting electrostatic interactions between ZnO NPs and a binding site. Similar changes in the macroscopic conductance were observed when lysenin channels were reconstituted in neutral lipid membranes, implicating protein-NP interactions as the major contributor to the reduced transport capabilities. In contrast, no inhibitory effects were observed in the presence of anionic S nO2 NPs. Additionally, we demonstrate that inhibition of ion transport is not due to the dissolution of ZnO NPs and subsequent interactions of zinc ions with lysenin channels.

**Conclusion**: We conclude that electrostatic interactions between positively charged ZnO NPs and negative charges within the lysenin channels are responsible for the inhibitory effects on the transport of ions. These interactions point to a potential mechanism of cytotoxicity, which may not require NP internalization.

## Background

The rapid development of certain nanomaterials (NMs) has led to their extensive use in many commercial applications including cosmetics, sporting goods, automotive parts, and electronics,[1-4] while many others are under intense investigation for scientific, technological, and biomedical applications.[5-9] The large surface area to volume ratio of these materials yields novel physical and chemical properties that enable applications that are unachievable using micron-sized bulk material of identical composition. The scientific community has spent decades developing an understanding of NMs in order to control their fundamental physical and chemical properties. However, early investigations demonstrated that some of the same properties that make NMs attractive for multiple applications may cause unintended hazardous interactions with biological systems. Therefore, environmental and human exposure poses potentially significant

risks,[10] and this paradigm has led to intense investigations on the potential biological impact of NMs.[11, 12] While we have thus far attained a tremendous body of knowledge on end-point effects such as cytotoxicity, neurotoxicity, genotoxicity and oxidative stress,[13-16] we lack a thorough understanding of the principles by which modulation of size, charge, composition, dissolution levels and surface chemistry affect the interaction of NMs with living cells.

ZnO nanoparticles (NPs) are considered to be one of the more toxic of the metal oxide NMs.[17, 18] Studies on ZnO NPs have demonstrated toxicity towards a large number of cell lines and model organisms, however, the mechanism of cytotoxicity is still under debate. Certain physicochemical properties, such as surface chemistry, dissolution potential, and their intrinsic ability to produce reactive oxygen species (ROS) have a strong impact on their cytotoxic effects.[19-21] Several studies have demonstrated that cytotoxicity stems from high dissolution rates, causing elevated levels of $Zn^{2+}$ ions in cellular media that eventually disrupt homeostasis and leads to cell death.[22, 23] Other groups have suggested that their intrinsic ability to produce ROS (which may arise from surface defects, such as oxygen vacancies) is responsible for the high cytotoxic potential of ZnO NPs.[24, 25] In the same line, $SnO_2$ NPs have been shown to inhibit kinetic growth and cytotoxicity towards certain cell lines and organisms,[18, 26, 27] while other publications have demonstrated modest to no cytotoxic effects.[28, 29] Similar to other NPs, the crystal and hydrodynamic size of $SnO_2$ NPs play an important role on their toxic effects, and smaller sizes have been shown to correlate with increased toxicity.[27]

Our inability to correctly predict how physical and chemical properties relate to toxicity stems from the fact that biological systems are elaborate and structurally and

functionally interconnected, making it very difficult to isolate distinct interactions responsible for cytotoxicity. Therefore, investigations utilizing a simplified model system that mimics the structure and function of a biological assembly can be an important step towards a more complete understanding of mechanisms of nanotoxicity. In these regards, we address how the directional flow of ions across lipid membranes containing specialized transmembrane ion transporters are affected by NPs. This work is motivated by the tremendous biological relevance of ionic transport for any living cell, and by the evidence that malfunctions of the mechanisms that control the transmembrane transport may have catastrophic consequences for cell functionality.[30]

Among transmembrane transporters, voltage-regulated channels play key roles in fundamental cellular processes such as creating and maintaining electrochemical gradients, transmission of information, ion transport, signaling, and metabolism.[31] A salient feature of such transporters is the regulation of their activity by transmembrane electric fields interacting with voltage-sensing domains present in the channel's structure.[32] The presence of charged domains in different regions of protein channels presents opportunities for electrostatic interactions with charged NPs, which may affect the transmembrane transport and functionality of the host cells.

Given the large variety of ion transporters in the cell membrane, isolating a particular one in a specific cell for relevant studies on transport modulation induced by NPs is not an easy task. Moreover, reconstitution of a particular ionic transporter in an artificial membrane system, although feasible, may require multiple, extensive and costly preparation steps. A simplified system featuring fundamental characteristics of ion channels may constitute an excellent model for investigating potential nanotoxicity

effects originating from the disruption of transmembrane transport of ions. Therefore, we propose a simplified model that explores the effects of charged NPs on the transport of ions through lysenin channels inserted into an artificial bilayer lipid membrane (BLM).

Lysenin is a pore-forming protein extracted from the coelom of the earthworm *E. foetida*, which self-assemble as a large conductance nonameric pore (~3 nm) in artificial and natural lipid membranes containing sphingomyelin (SM).[33-35] The recently deciphered crystal structure indicates large charged domains present within the channel,[36, 37] thus presenting a strong potential for electrostatic interactions with charged NPs. The physiological role of lysenin is still obscure but the cytolytic and hemolytic activity is indicative of a pore-forming toxin.[38] Nonetheless, its relevance for nanotoxicity studies stem from several remarkable biophysical properties it shares with ion channels. Unlike many other pore-forming toxins and similar to voltage-gated ion channels, lysenin channels present asymmetrical voltage-induced gating.[33, 39] They adopt an open state at negative voltages, while positive voltages larger than ~+20 mV induce gating and closing.[39, 40] This salient feature is complimented by reversible ligand-induced gating, manifested as conformational changes in the presence of low concentrations of multivalent metal cations leading to channel closure.[41, 42] Once the multivalent cations bind and induce conformational changes, the channel adopts a sub-conducting or closed state.[41, 42] Another advantageous property of lysenin channels is that voltage and ligand-gating properties can be easily discriminated. This is achieved by reconstituting the channels in neutral lipid membranes which maintains the ligand-induced gating mechanism but renders lysenin unresponsive to the applied voltage.[41, 42] The high transport rate of lysenin channels yield large ionic currents which facilitate data recording

and analysis. Lastly, lysenin channels are easily reconstituted in artificial membrane systems containing SM, are stable for extended time periods, and the monomer form of the protein is commercially available.

## Methods

Chemicals and Nanoparticles

Asolectine (Aso), cholesterol (Chol), SM (from Sigma-Aldrich) and diphytanoyl phosphatidylcholine (DiPhytPC, from Avanti Polar Lipids) were purchased as powders and dissolved in n-decane at a final concentration of 50 mg/mL. For the support electrolyte, NaCl (Fisher Scientific) was dissolved in nanopure water at a final concentration of 130 mM (if not otherwise indicated) and buffered with 20 mM 4-(2-hydroxyethyl)-1-piperazineethanesulfonic acid (HEPES) at pH = 7.2. ZnO and $SnO_2$ NPs were synthesized using wet chemical methods as previously described.[43, 44] Briefly, for ZnO NP samples, the precursor zinc acetate dihydrate ($Zn[CH_3CO_2]_2 \cdot 2H_2O$) was suspended in diethylene glycol. The solution was heated and nanopure water was added when the solution reached $80^0$ C. The temperature was then brought to and held at $150^0$ C for 90 minutes. The NPs were collected by centrifugation and subsequently washed with ethanol. For $SnO_2$ NPs, sodium stannate ($Na_2[Sn(OH)_6]$) and urea were used as precursors with nanopure water as the solvent. The solution was heated to 90 $^0$C and held for 90 minutes. The NPs were collected via centrifugation and subsequently washed with nanopure water. Characterizations were performed using X-ray diffraction (XRD) (Figure S1, Additional file 1), transmission electron microscopy (TEM) (Figure S2 and S3, Additional file 1), zeta potential (ZP) measurements, dynamic light scattering (DLS) (Figure S4, Additional file 1), X-ray photoelectron spectroscopy (XPS) (Figure S5,

Additional file 1) and Fourier-transform infrared spectroscopy (FTIR) (Figure S6, Additional file 1). XPS confirmed sample purity and atomic concentrations for stoichiometric ratios. XRD was employed to ensure crystal phase purity and to obtain average crystalline size for both samples. XRD confirmed the expected hexagonal wurzite crystal structure for ZnO and cassiterite for $SnO_2$. The average crystal size for ZnO and $SnO_2$ NPs was analyzed with Rietveld refinement using Materials Analysis Using Diffraction (MAUD) software and estimated at 8.3 +/- 2 nm and 4.3 +/- 0.04 nm respectively. A JEOL JEM-2100 HR analytical TEM was used to confirm spherical morphology and average crystal sizes. FTIR spectra was collected using a Bruker Tensor 247 spectrometer and FTIR pellets were produced by first grinding 1.6 mg of each NP sample with 0.200 g of spectroscopic grade KBr. The ground powder mixture was then pressed with 8 tons of pressure for 3 minutes and pellets were analyzed after removing the KBr background. Zeta potential and DLS measurements were performed, after dispersing the powders in nanopure water at a concentration of 1 mg/mL, using a Malvern Zetasizer NanoZS. ZnO NP clusters had an average hydrodynamic size (HDS) of 276 nm and average ZP of +32mV, whereas $SnO_2$ NP clusters average HDS was 176 nm with an average ZP of -42.0 mV.

Bilayer Lipid Membrane Setup

The experimental setup employed the use of a planar BLM chamber consisting of two polytetrafluoroethylene (PTFE) reservoirs separated by a thin (~120μm) PTFE film that had been pierced with an electric spark to create a circular hole of ~ 70 μm diameter.[45, 46] The reservoirs were filled with 1mL buffered electrolyte and connected via two Ag/AgCl electrodes inserted in the solution to an Axopatch 200B amplifier

(Molecular Devices). The amplified analog signal fed the DigiData 1440A digitizer (Molecular Devices) which provided the digital signal for visualization, recording, and further analysis. Continuous stirring of the solutions in the BLM chamber was assured by a low-noise magnetic stirrer (Warner Instruments). All the experiments were performed in voltage-clamp mode upon manual or automatic voltage stimulation. The signal recorded during various voltage stimulations was further analyzed with ClampFit 10.6.2.2 (Molecular Devices) and Origin 8.5.1 (Origin Lab) software packages.

Experimental Procedure

Lipid membrane preparation was performed by "painting" the hole in the PTFE film with small amounts of lipid mixtures composed of 4mg Aso or DiPhytPC, 2mg Chol, and 2mg SM dissolved in ~400μL n-decane.[46, 47] The successful creation of the BLM was indicated by measuring the capacitance in response to an applied triangular voltage stimulation, while achievement of a seal resistance larger than 1000 GΩ was assessed by measuring the leakage current in response to a DC voltage stimulation (100 mV). Channel insertion was performed by adding the lysenin monomer (from Sigma-Aldrich, 0.3 nM final concentration) to the ground (*cis*) reservoir under continuous stirring and at -60 mV bias potential applied to the *trans* (headstage) reservoir. The application of a negative voltage was required to prevent the voltage-induced gating which manifests at positive transmembrane potentials.[33, 39, 40] After the insertion process was completed, as indicated by a steady state value of the open current, an extensive flushing of the *cis* reservoir with lysenin-free electrolyte was performed to remove the bulk monomer and prevent additional insertions. To avoid potential changes in the lysenin functionality originating in congestion effects,[48] the total number of channels

inserted into the membranes was limited to ~1000. To facilitate quantitative comparison of the influence of NPs on the transport properties of lysenin channels in parallel experiments comprising different numbers of inserted channels, we used the relative changes in the macroscopic conductance ($G_r = G/G_0$) for data plotting, where G is the conductance after addition of NPs and $G_0$ is the conductance before addition. In order to avoid premature dissolution and/or aggregation, the NPs (powder form) were dispersed by sonication for 5 minutes in the support electrolyte solution in a sonication bath before each addition to the reservoirs.

## Results and Discussion

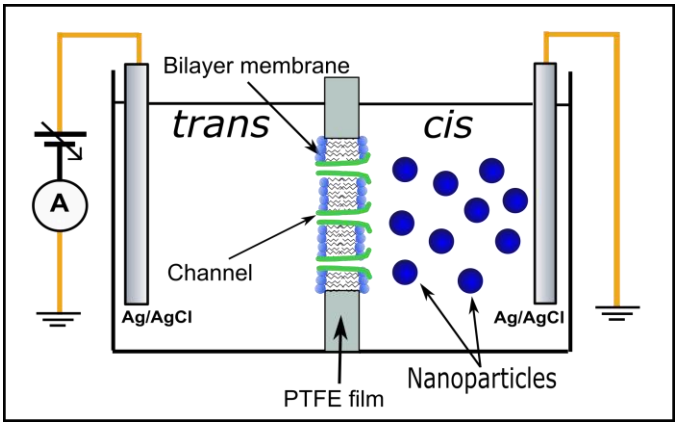


**Figure 3.1 The experimental setup comprises lysenin channels reconstituted into planar lipid bilayer membranes. The modulation of ionic transport and regulation by ZnO NPs is assessed in classic voltage-clamp experiments.**

Once a steady state current through the population of lysenin channels was achieved, the NPs were introduced into either side of the chamber with both negative and positive voltages applied across the membrane to assess their effect on the macroscopic conductance (see Fig. 1 for a schematic of the setup). The addition of ZnO NPs (20 µg/mL final concentration) to either side of the membrane containing lysenin channels, when biased by -60 mV, yielded only a modest decrease of the macroscopic conductance,

i.e. a few percent, irrespective of the side of addition (Fig. 2). This slight decrease in the conductance suggests a minimal influence of ZnO NPs on the lysenin channels' ability to transport ions in these particular experimental conditions.

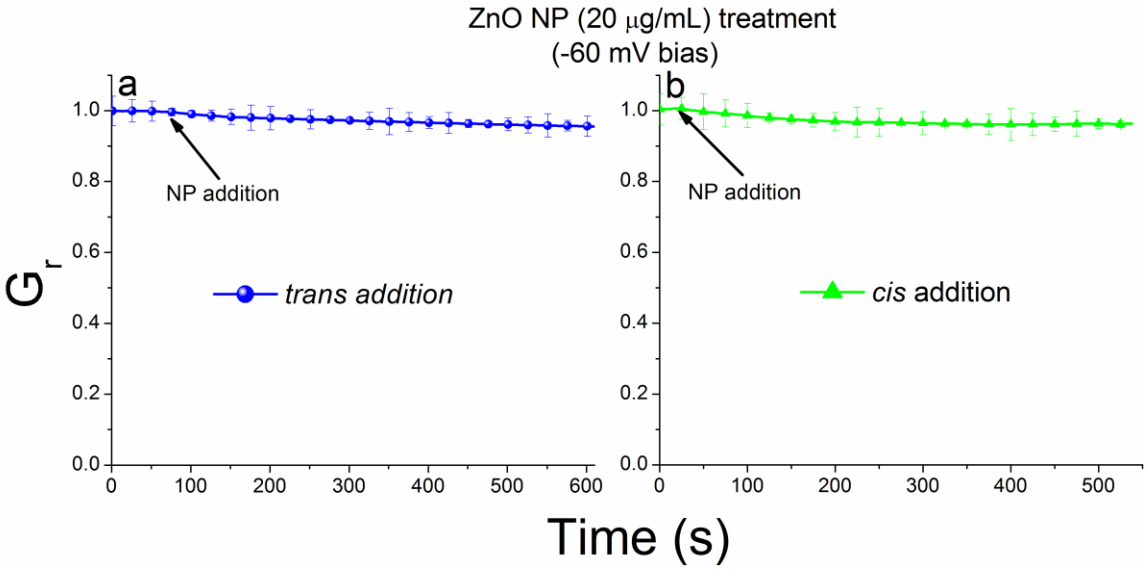


**Figure 3.2 ZnO NPs do not alter the ionic conductance of lysenin channels when biased by a -60 mV transmembrane voltage. Addition of ZnO NPs to either *trans* (a) or *cis* (b) reservoirs induces only negligible changes of the macroscopic conductance. The experimental values are reported as mean ± S.D., n = 3. All the data points represent experimental values but symbols have been skipped for improved visibility.**

To explain the small reduction in conductance, one may hypothesize several different mechanisms such as ligand gating induced by small amounts of $Zn^{2+}$ ions provided from low NP dissolution, ligand gating induced by NP binding to a specific binding site, or physical occlusion by transient NP attachment to the opening of the nanopore. Past investigations show a dramatic yet reversible decrease of the macroscopic conductance of lysenin channels in the presence of low concentrations of multivalent cations,[41, 42] indicative of strong interactions with lysenin channels. Those interactions have been elucidated in single-channel experiments, which provide evidence of gating, i.e. transition from the open state to a sub-conducting or closed state.[41, 42] To explain

lysenin's reversible gating in the presence of multivalent cations, it is assumed that the channel's structure contains at least one negatively-charged binding site with high affinity for cations, which triggers gating upon binding. A potential leakage of $Zn^{2+}$ ions from NPs may affect the macroscopic conductance of lysenin channels, as observed. In addition, if exposed this binding site could electrostatically interact with cationic NPs and yield a significant decrease in conductance either by induced gating or physical occlusion of the conducting pathway. However, such strong effects were not observed in the above experimental conditions, which prompted us to look closer to the lysenin's structure for alternative explanations. The assembled lysenin channel shows the presence of multiple anionic domains,[36, 37, 49] hence presenting opportunities for physical occlusions of the channels through electrostatic interactions even in the absence of gating. We may account for the weak conductance inhibition by considering the position of a binding site and the orientation of the external electric field. A deep-buried binding site would be inaccessible from either side to NPs larger than the channel's diameter (~3 nm), which is mostly the case in our investigations. Nanoparticle interaction with a binding site present at the *trans* opening of the channel would be prevented at -60 mV by the electric field orientation. Although the electric field in the bulk is very low, its amplitude increases substantially when approaching the channel opening (fringe effects), therefore keeping the NPs far from a binding site located at the *cis* opening. The same electric field will drive the NPs added to the *cis* side towards the membrane but the lack of changes in macroscopic conductance suggest the absence of a binding site at this location. The hypothesis of an exposed binding site at the *trans* opening was further sustained in similar experiment comprising *trans* NP addition and no transmembrane voltage; in such experimental

conditions, a marked decrease of the macroscopic conductance was observed at -60 mV after two hours of NP incubation in the absence of a bias potential (data not shown). However, this result could be an artifact originating from dissolution during the prolonged NP exposure to the electrolyte solution.

To identify if the elusive binding site is located either deep within the channel or at the *trans* side, we performed the experiments under positive bias potentials (Figure 3). After the channel insertion process, the influence of ZnO NPs was assessed in experiments comprising of *cis* or *trans* addition and opposite orientations of the electric field. Lysenin channels are voltage-gated at positive voltages greater than ~+20 mV but are stable in the open state for extended time periods as long as the applied voltage is less than this critical value.[33, 39] Interestingly, addition of ZnO NPs to the *trans* side under positive biasing (+15 mV to prevent voltage gating) induced a rapid and sustained decrease of the macroscopic conductance (Fig. 3), while *cis* addition elicited only a weak response in otherwise similar conditions. Consequently, we concluded that the electric field plays a major role in preventing ZnO NPs accumulation near the membrane when biased by -60 mV, however, in the absence of an electric field or when positive voltages are applied, ZnO NPs may interact with a binding site situated at the *trans* opening of the channel.

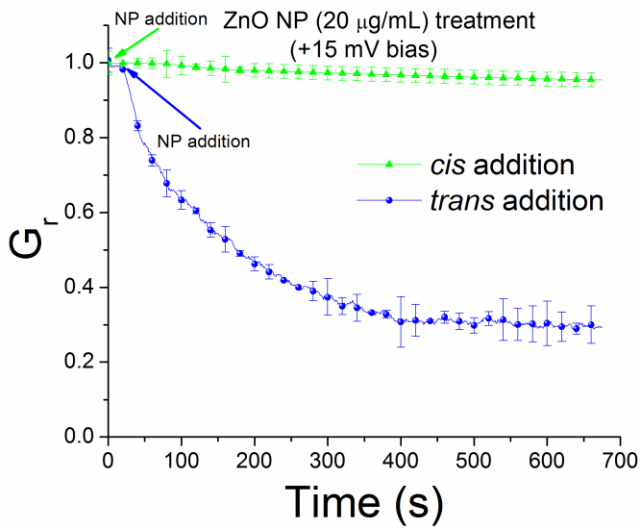


**Figure 3.3 Interactions between lysenin channels and ZnO NPs at +15 mV bias potential. *Cis* addition (green) of ZnO NPs yield minor changes in the macroscopic conductance. In contrast, *trans* addition (blue) elicits a significant decrease of the macroscopic conductance by ~70 %. The experimental values are reported as mean ± S.D., n = 3. All the data points represent experimental values but symbols have been skipped for improved visibility.**

Dissolution of ZnO NPs can result in high extracellular $Zn^{2+}$ concentrations which have been proposed as one of the main mechanisms of ZnO NPs cytotoxic effects.[22, 23, 50] Zinc ions inhibit the macroscopic conductance of lysenin channels by a ligand-induced gating mechanism.[41, 42] Due to the high sensitivity of lysenin channels to $Zn^{2+}$, dissolution may explain the observed inhibition of conductance upon exposure to ZnO NPs. To eliminate such potential experimental artifacts, we performed investigations in similar conditions but added $Zn^{2+}$ ions ($ZnSO_4$; 2 mM final concentration) to the reservoirs instead of ZnO NPs. Addition of $Zn^{2+}$ to the either side, biased by -60 mV, yielded a sudden decrease of the macroscopic conductance in agreement with previous reports (Fig. 4).[41, 42] Addition of the same amount of $Zn^{2+}$ to a similar BLM containing lysenin channels and biased by +15 mV (to prevent voltage-induced gating) yielded a similar relative decrease of the macroscopic open current (Fig. 4). If conductance inhibition elicited by ZnO NPs had been induced by the $Zn^{2+}$ ions dissipating from the NPs, then

addition to either side would have displayed a similar pattern of conductance inhibition. However, addition of $Zn^{2+}$ ions yielded fundamentally different results compared with the experiments involving ZnO NPs. $Zn^{2+}$ ions affected the macroscopic conductance irrespective of the side of addition and direction of the electric field, while the inhibitory activity of ZnO NPs depended on both these experimental parameters. The total concentration of ZnO NPs was only 20 μg/mL (corresponding to ~0.25 mM $Zn^{2+}$ ions) and resulted in a 70% decrease in the macroscopic conductance. In order to obtain an approximate decrease of only 45% in conductance measurements with $Zn^{2+}$ ions, the experiment employed a final concentration of 2.0 mM. Assuming complete dissolution of ZnO NPs, this would correlate to approximately eight times the amount of $Zn^{2+}$ ions from $ZnSO_4$ in the solution. To further eliminate the possibility that the $Zn^{2+}$ ions contributed to the observed conductance inhibition, experiments with ZnO NPs were carried out in the presence of the strong $Zn^{2+}$ chelator EDTA. EDTA (10 mM) was added to the solutions prior to nanoparticle addition, thus effectively preventing any interactions of the free zinc ions from the NPs with lysenin channels. These experiments yielded almost identical decreases in the macroscopic conductance when compared with ZnO NPs with no EDTA (Figure S7, Additional file 1). Our results clearly indicate that the conductance inhibition elicited by ZnO NPs was not a consequence of $Zn^{2+}$ ions from dissolution. These experiments revealed that the extent of the conductance inhibition depended on both the orientation of the lysenin channels and the electric field relative to the site of ZnO NP addition. The observed conductance inhibition may originate from local accumulation of NPs by electrophoretic effects, specific interactions with the membrane itself, or preferential interactions with binding sites of lysenin.

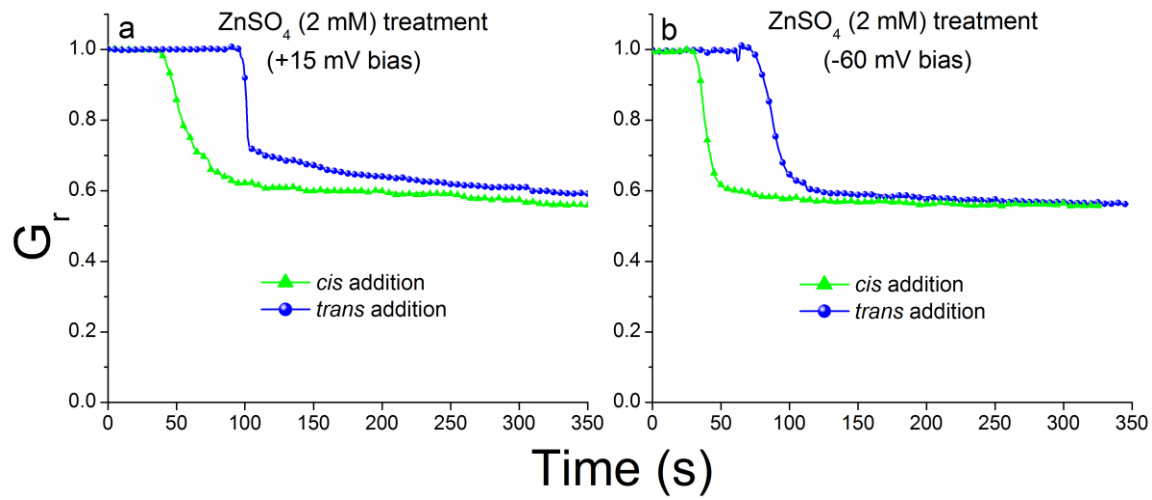


**Figure 3.4 $Zn^{2+}$ ions decrease the macroscopic conductance of lysenin channels irrespective of bias potential and site of addition. At +15 mV transmembrane voltage (a), $Zn^{2+}$ addition to either the *cis* or *trans* reservoir reduces the macroscopic conductance by ~ 40%. Similar decreases are recorded upon $Zn^{2+}$ interactions with lysenin channels biased by -60 mV (b). The presented data represent a typical single run for each experiment.**

Next, we asked whether or not exposure to ZnO NPs changes the voltage-induced gating profile. To answer this question, the voltage-induced gating of lysenin channels was assessed from the I-V plot recorded in the range -60 to +60 mV (Fig. 5) at a voltage rate of 0.2 mV/s with and without the addition of ZnO NPs. The macroscopic current recorded in absence of NPs (Fig. 5) featured the well-known characteristics of voltage-induced gating, i.e. a linear behavior in the negative voltage range, indicative of the absence of gating, and a non-linear behavior at positive voltages higher than +20 mV, indicative of channel closure.[33, 39, 40] A typical feature of the macroscopic current recorded at positive voltages is the transition from high current to low current through a dynamic negative resistance region.[39, 40] The macroscopic currents recorded in the same voltage range after addition of ZnO NPs (20 µg/mL final concentration) to the *trans* side of the membrane yielded a fundamentally different I-V plot (Fig. 5). The addition of ZnO NPs elicited a slight decrease in the open current recorded in the negative voltage range,

however, the I-V characteristic preserved quasi-linearity between -60 mV and -20 mV. Once the voltage approached neutral values, the macroscopic current greatly deviated from the control I-V plot and the ionic transport capabilities of lysenin channels were strongly diminished in the presence of ZnO NPs. Interestingly, the macroscopic conductance started to decrease at small negative voltages, as indicated by the diminished slope of the I-V plot. This is consistent with the hypothesis that the fringe effect of the electric field prevents the NPs from interacting with the binding site. The magnitude of the electric field decreases with decreasing applied voltage and the weak electrophoretic force, although opposed, is not sufficient to prevent interactions with the binding site and channel conductance modulation. The consistently lower macroscopic currents indicated that addition of ZnO NPs induced severe channel conductance inhibition as demonstrated by the large decrease of the macroscopic current at any positive voltage. At positive voltages, the currents recorded in the presence of ZnO NPs were consistently lower than the currents recorded in the absence of ZnO NPs up to ~+40 mV, after which the recorded currents were similar to the control when the channels are in a closed state.

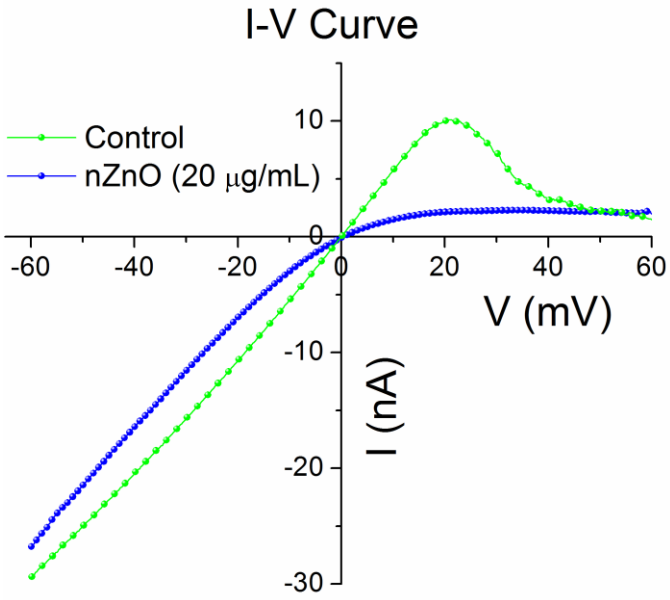


**Figure 3.5 Effects of ZnO NPs on lysenin voltage-induced gating. In the absence of NPs, lysenin channels begin to close at transmembrane potentials greater than 20 mV (green curve). ZnO NPs (20 μg/mL final concentration) almost completely abrogate the conductance in the positive voltage range (blue curve) and indicate a strong interaction with the lysenin channels. All points on the curves are experimental data and symbols have been added for discrimination. The presented data represent a typical single run for each experiment.**

This experiment demonstrated that ZnO NPs affect the macroscopic conductance of lysenin channels in a voltage-dependent manner but it does not offer a complete mechanistic description. The significant changes in the I-V curve after addition of ZnO NPs potentially stem from multiple mechanisms. Experimental evidence and theoretical modeling have demonstrated that electrostatic interactions between membrane components and NPs are key factors that contribute to toxicity and the ability of NPs to internalize into cells.[51-53] Our experiments comprised a simple system consisting of lysenin channels inserted into an artificial BLM composed of charged lipids. We assumed that the conductance of lysenin channels was affected by interactions between the proteins channels and NPs but we could not exclude interactions between the charged

lipids and ZnO NPs as a source of conductance modulation. The Aso lipid mixture used for BLM preparation contains several anionic components that may interact electrostatically with voluminous cationic NPs unable to penetrate the lumen, which would lead to channel conductance modulation. To elucidate the potential role played by the charged lipids, we performed experiments by replacing Aso with neutral DiPhytPC. The use of neutral lipids abolishes the voltage-induced gating at positive voltages while preserving the ligand-induced gating observed in the presence of multivalent cations.[41, 42] Addition of ZnO NPs to the *cis* side of a neutral membrane containing lysenin channels and biased by +60 mV elicited no change in the macroscopic conductance (Fig. 6). However, addition of ZnO NPs to the *trans* side of the same membrane, biased by an identical positive voltage, yielded a massive decrease in conductance similar to the results obtained using charged lipids (Fig. 6). The non-symmetrical response and preservation of the inhibitory capabilities of ZnO NPs recorded for the neutral BLM suggest that the inhibition mechanism excludes electrostatic interactions between NPs and lipids. The interaction between lysenin channels and ZnO NPs is therefore likely responsible for the observed inhibitory activity.

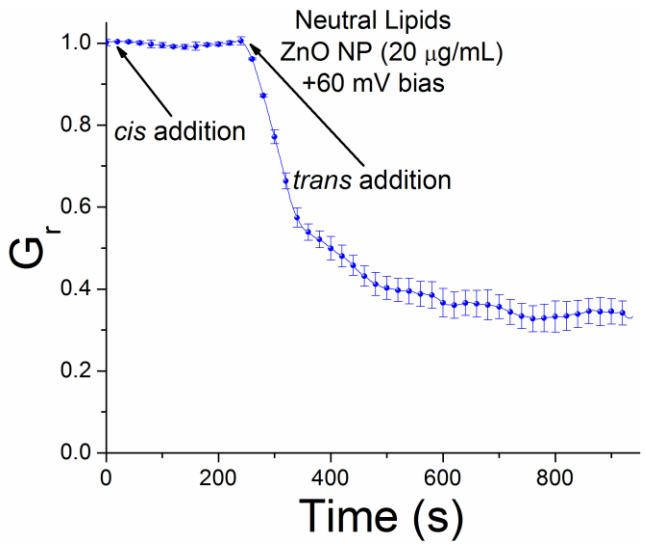


**Figure 3.6 Lysenin channels reconstituted in neutral lipid membranes interact with ZnO NPs at +60 mV transmembrane voltage. *Cis* addition of ZnO NPs elicits no changes in the macroscopic conductance. In contrast, ZnO NPs added to the *trans* reservoir interact with lysenin channels and significantly diminish their ionic transport capabilities. The experimental values are reported as mean ± S.D., n = 3. All the data points represent experimental values but symbols have been skipped for improved visibility.**

We have shown that lysenin channels interact with positively charged ZnO NPs but have not yet demonstrated the electrostatic nature of those interactions. Therefore, we asked whether or not any NPs electrophoretically driven towards a specific or non-specific yet accessible binding site would interact with lysenin channels and inhibit their conductance. In this respect, we performed conductance experiments by replacing positively charged ZnO NPs with negatively charged $SnO_2$ NPs (-42 mV ZP). Irrespective of the applied voltage and the addition site, $SnO_2$ NPs did not affect the macroscopic conductance of lysenin channels (Fig. 7). In order to try to elicit interactions with $SnO_2$ NPs, 200 μg/mL (final concentration) of $SnO_2$ NPs were used, which is 10x the concentration of ZnO NPs that induced rapid decreases in the macroscopic conductance (Fig. 3). The crystal and hydrodynamic sizes of $SnO_2$ NPs used in this experiment were much smaller than ZnO NPs, suggesting that $SnO_2$ NPs would be better

suited to inhibit conductance by physical occlusion. The absolute magnitude of the ZP for $SnO_2$ NPs was also larger than ZnO NPs, further strengthening the hypothesis of a mechanism that requires strong electrostatic interactions between cationic ZnO NPs and an anionic domain present at the *trans* side of the lysenin channel to induce conductance inhibition. Also, to further support the hypothesis that electrostatic interactions between the lysenin channels and ZnO NPs initiate a decrease in conductance, we investigated the effects of electrostatic screening induced by an increased ion concentration in the bulk electrolyte solutions. Addition of 20 µg/mL ZnO NPs to the *trans* side of the bilayer containing lysenin channels in 500 mM NaCl and under positive bias reduced the conductance inhibition by ~15% (Figure S8, Additional file 1), which is a large reduction from what we observed at 130 mM NaCl concentration (~70%, Fig. 2). In addition, the time required to reach equilibrium increased to more than 2500 s, indicating that ionic screening weakened the interactions between NPs and lysenin channels, and supporting the hypothesis that electrostatic interactions are at the origin of the observed changes in conductance. However, we may not eliminate potential artifacts arising from the effects of screening on the ZnO NPs. At high salt concentration, screening may accelerate NP aggregation, which is what we observed when attempting to further increase the ionic concentration of the bulk electrolyte solutions. The ZnO NPs rapidly aggregated into large clusters at the bottom of the vials in a matter of minutes, which prevented further experimentation in high ionic strength conditions.

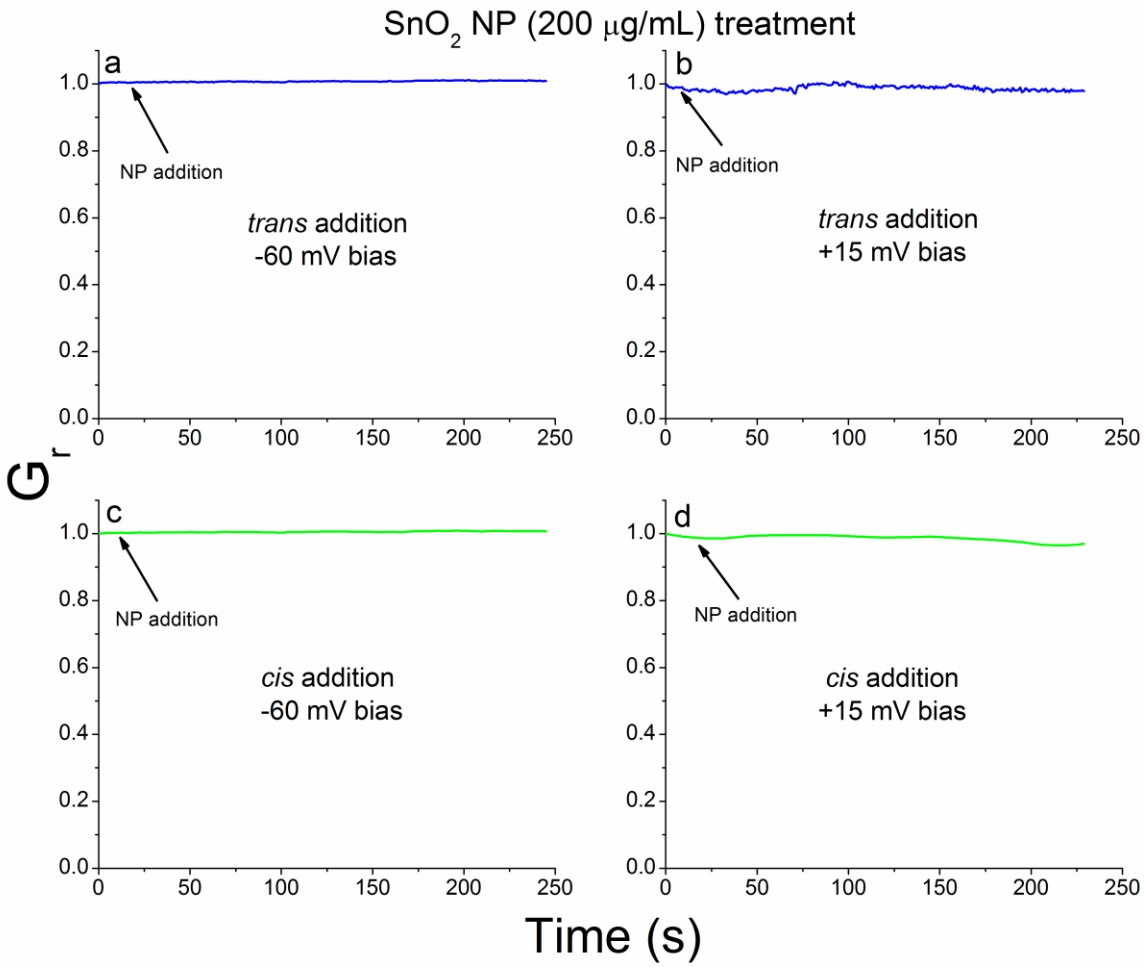


**Figure 3.7 Interactions between anionic $SnO_2$ NPs and lysenin channels reconstituted into a planar bilayer lipid membrane. Addition of $SnO_2$ NPs to the *trans* reservoir at -60 mV (a) and +15 mV (b) indicates insignificant changes of the macroscopic conductance. Similarly, $SnO_2$ NP addition to the *cis* reservoir at -60 mV (c) and +15 mV (d) yields negligible changes in the ionic transport capabilities. The presented data represent a typical single run for each experiment.**

A few assumptions can be proposed about the mechanism responsible for the observed decrease in macroscopic conductance elicited by addition of ZnO NPs. Electrostatic interactions may bring ZnO NPs close enough to the channels such that the resulting physical blockage reduces the individual currents. In such case, an opposite electric field of appropriate magnitude may drive the NPs away from the binding site therefore unblocking the channels. Our attempts to apply higher voltages across the BLM and to force the unblocking were not successful. However, it is possible for the binding

site to have a relatively strong affinity for charged ZnO NPs and consequently the force required to remove the NPs from the binding sight may require much higher electric fields. Unfortunately, such experiments are very difficult to achieve as the BLM is prone to disruption at high transmembrane voltages.

Another potential inhibition mechanism mimics ligand-induced gating. It has been established that lysenin channels interact with multivalent cations and undergo conformational transitions that force the channel into closed or sub-conducting states.[41, 42] This ligand-induced gating mechanism relies on electrostatic interactions between cations and one or more binding sites but ionic current blockage stems from the induced gating. It is possible that charged ZnO NPs interact electrostatically with one or more binding sites, yet not necessarily the same one(s) involved in the ligand-induced gating and would force the channels to adopt a sub-conducting or a closed state. Lastly, defects on the surface of ZnO NPs such as oxygen vacancies have been shown to correlate with ROS production.[24, 54] Since the electrostatic interactions induce close contact of ZnO NPs with the channels, the highly reactive surface of ZnO NPs may interact with cysteine and methionine residues in their structure which may alter channel functionality and conduction similar to reports of oxidation of cysteine residues in $Ca^{2+}$/$K^{+}$ channels.[55, 56]

## Conclusions

Our work demonstrates that the transport properties of lysenin channels change significantly in the presence of cationic ZnO NPs. The modulation of the transport properties by NPs is strongly dependent on the net charge, and the orientation of the electric field and channel with respect to the NPs. There is little doubt that the primary interaction between NPs and lysenin channels is electrostatic. Nonetheless, the simplicity

of the experimental system investigated here does not necessarily warrant biological interpolation to other protein channels interacting with NPs, not even ZnO. In complex biological environments, the binding of various functional groups on the NP surface may significantly alter their ability to interact with membrane components irrespective of the surface charge of the pristine nanomaterial. Given the aggregation tendency of the investigated NPs, we may not exclude aggregation at the membrane surface as being at the origin of conductance changes. Even the neutral lipids used for our investigations present a dipole moment that may initiate NP binding; further NP aggregation at these binding sites may impede the ionic flow by physical occlusion or by introducing supplementary electrostatic energy barriers for ions. However, if an induced dipole moment that initiated binding of NPs to lipids occurred, then $SnO_2$ NPs should have yielded a similar response due to their higher net charge. In spite of these shortcomings, an important conclusion of this report pertains to the potential ability of NPs to interact with transmembrane transporters without the need of internalization. Many previous studies assume that cytotoxic effects of NPs are due to translocation of NPs into the cytosol by various transport mechanisms and/or dissolution of the NPs, disrupting homeostasis and interfering with vital cellular processes. Our work suggests that NPs may tamper with ionic transport mechanisms by basic electrostatic interactions. Given the physiological relevance of controlled transmembrane transport, such alterations may have catastrophic effects for cells. While this observation is generally valid for any cell, it may prove extremely helpful for understanding the potential neuro-toxic effects of NPs.[57] The physiology of the neural cell is based on the transport properties and regulation of voltage-gated ion channels, which are transmembrane structures with multiple charged

domains that may interact electrostatically with NPs. Changes in the voltage-induced gating mechanism or blockage of ionic transport induced by NPs[57] may dramatically affect the correct functionality of the nerve cell. Such interactions may explain why certain NPs specifically alter the individual currents through specific channels while the transport properties of other channels are not affected by various NPs.[58, 59] The local distribution of charge within the structure of several ion channels is currently known so it may be possible to predict potential toxic effects based on interactions with charged NPs, or to design NPs intended to alter the activity of transmembrane transporters.

This foray into deciphering the effects of NPs on the transmembrane transport of ions indicates alterations in the transporters' functionality as a potential mechanism of cytotoxicity. A previous study shows that ZnO NPs may induce neuronal cytotoxicity and genotoxicity in the absence of internalization or free $Zn^{2+}$ ions released from the NPs.[60] Future experiments will shed more light on intimate mechanistic details and the role that electrostatic interactions play in modulating the biological activity of protein channels.

## Declarations

### Ethics approval and consent to participate

Not applicable.

### Consent for publication

Not applicable.

### Availability of data and materials

The datasets used and/or analyzed during the current study are available from the corresponding author on reasonable request.

### Competing interests

The authors declare that they have no competing interests.

**Funding**

Research reported in this publication was supported by the National Science Foundation

(grant number 1554166), the National Aeronautics and Space Administration (grant number NNX15AU64H), and the National Institutes of Health (grant number P20GM109095 and P20GM103408). The content is solely the responsibility of the authors and does not necessarily represent the official views of the granting agencies.

**Author's contributions**

Conceived and designed experiments: DF. Wrote the paper: DF, JEE, SLB, NS. Performed nanoparticle/lysenin interaction experiments: SLB, DF, SR, HA, CH, NS, MM. Performed nanoparticle/lysenin interaction experiments, data analysis, and interpretation: DF, SLB, JEE, SR, HA, CH, NS, MM. Nanoparticles fabrication and characterization/analysis: JEE, AP. All authors read and approved the final manuscript.

**Acknowledgements**

SLB and JEE contributed equally to this work.

**Additional file.**

Additional file 1, pdf. Supplementary material that includes complementary figures of material characterization (Fig. S1-Fig. S5: XRD, TEM, DLS, XPS, and FTIR for ZnO and $SnO_2$ NPs), changes in relative macroscopic conductance of lysenin channels in the presence of ZnO NPs and EDTA (Fig. S6), and conductance inhibition at high ionic strength (Fig. S7).

**Supplementary Material**

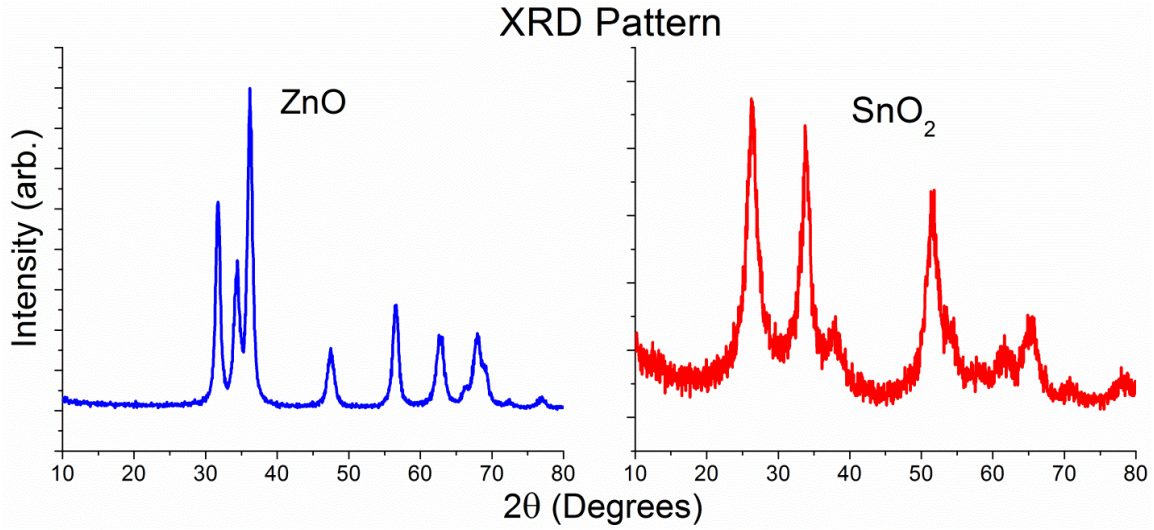


**Figure S3.1 The XRD spectra of ZnO (left) and $SnO_2$ (right). For ZnO, XRD confirmed the hexagonal wurzite crystal structure with no alternate crystal phases detected. The average crystal size determined for ZnO was estimated at 8.3 nm. The XRD spectra of $SnO_2$ demonstrated the crystal phase obtained was cassiterite with no alternate phases present. The average crystal size for $SnO_2$ was determined to be 4.3 nm from the XRD spectra.**

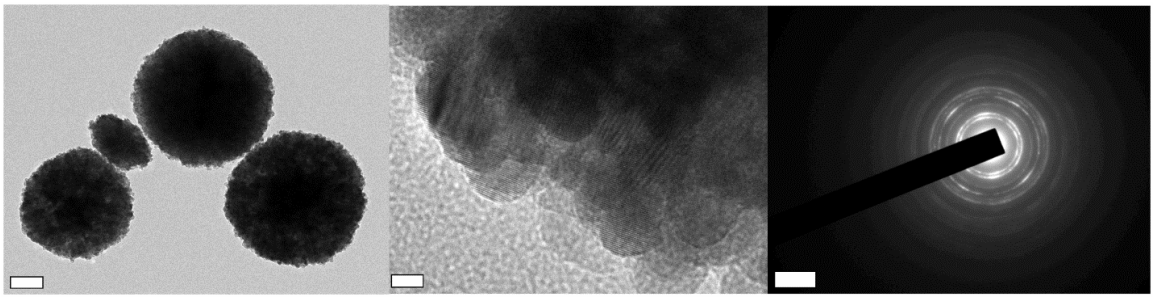

**Figure S3.2 TEM images and electron diffraction pattern of ZnO nanoparticles. (Left; scale bar: 100 nm ) The lower magnification image shows that the ZnO crystals aggregate to form larger spheres. (Middle; scale bar: 5 nm) Higher magnification images demonstrate that the large aggregates are comprised of small ZnO nanoparticles with an average size of ~10 nm. (Right; scale bar: 5 1/nm ) The electron diffraction pattern obtained from the ZnO nanoparticle sample.**

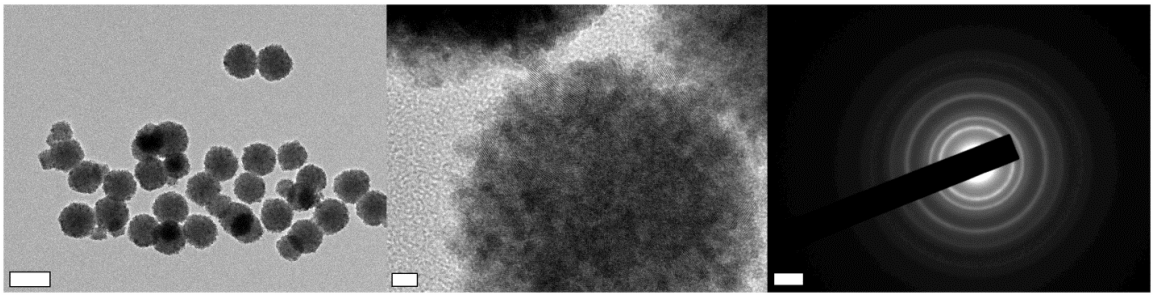

**Figure S3.3 TEM images and electron diffraction pattern of $SnO_2$ nanoparticles. (Left; scale bar: 100 nm ) The lower magnification image shows that $SnO_2$ nanoparticles also form larger aggregates which are generally smaller than the aggregates seen from the ZnO nanoparticles used. (Middle; scale bar: 5 nm) Higher magnification reveals that the aggregates formed are from small $SnO_2$ nanoparticles with an average size of ~5 nm. (Right; scale bar: 2 1/nm ) The electron diffraction pattern obtained from the $SnO_2$ nanoparticle sample.**

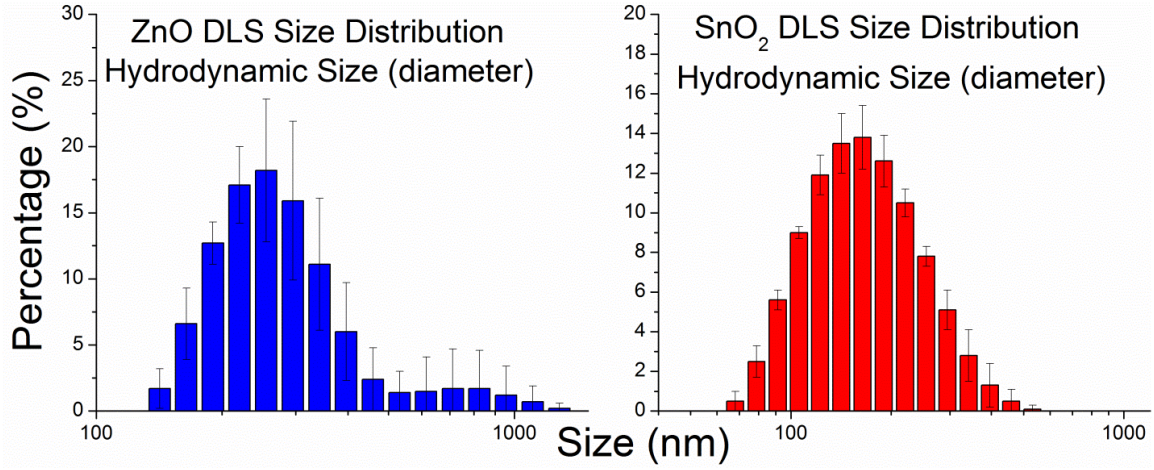


**Figure S3.4 Hydrodynamic size distributions of ZnO (left) and $SnO_2$ (right) obtained from dynamic light scattering measurements. Hydrodynamic size distributions of $SnO_2$ demonstrate smaller average aggregates than ZnO, consistent with images obtained from TEM. The smaller particle size of $SnO_2$ suggests that these NPs would be better suited to inhibit conductance of lysenin channels by physical occlusion but this was not observed experimentally.**

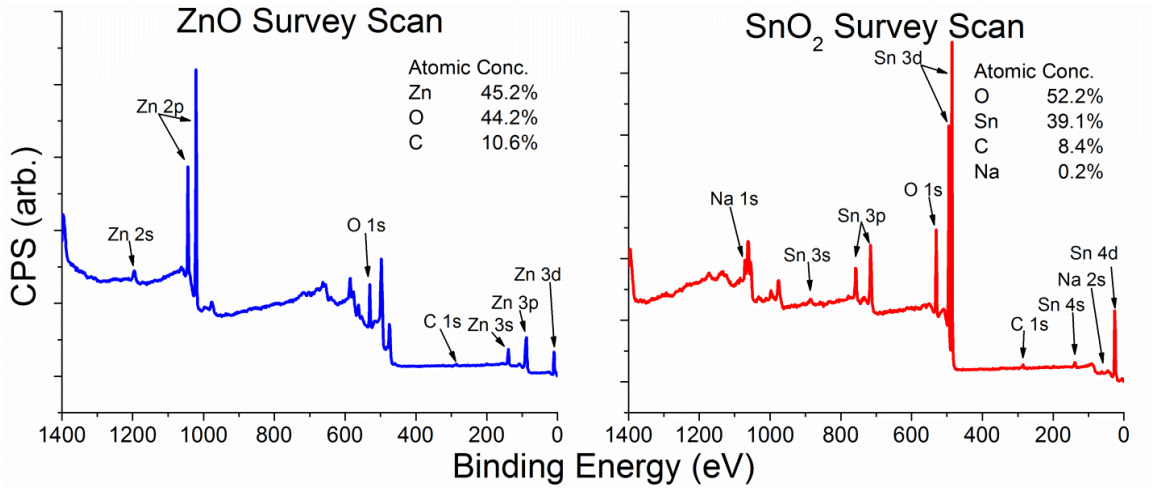


**Figure S3.5 X-ray photoelectron spectroscopy survey spectra of ZnO (left) and $SnO_2$ (right) nanoparticles. Spectra demonstrate high sample purity, small retention of carbon species and sodium in the case of $SnO_2$, likely from carbon dioxide from atmospheric exposure and species retained from the chemical precursors.**

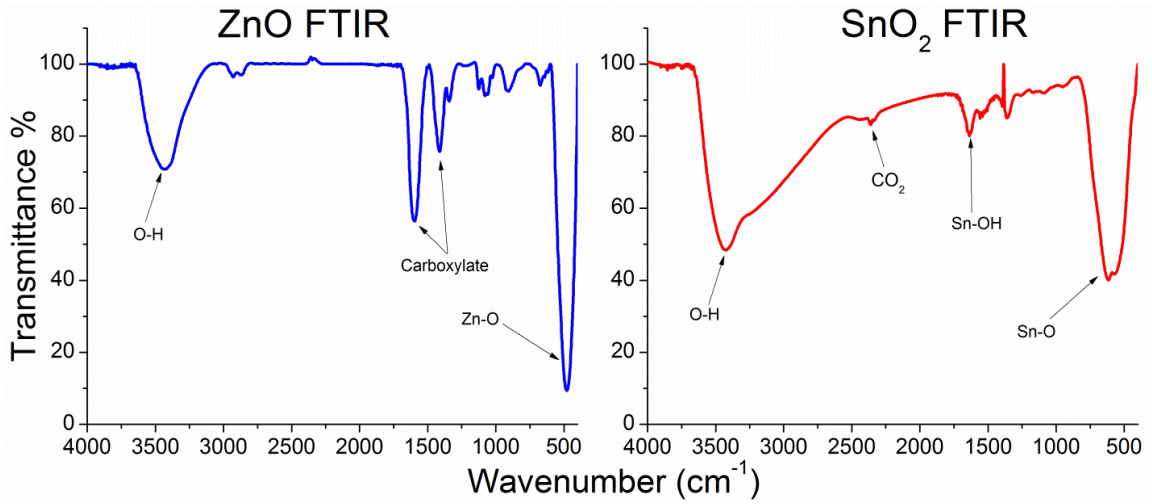


**Figure S3.6 Fourier-transform infrared (FTIR) spectra of ZnO (left) and $SnO_2$ (right) nanoparticles. Spectra confirm retained species from chemical precursors and carbon dioxide, as well as demonstrate hydroxide species are present in both nanoparticles synthesized.**

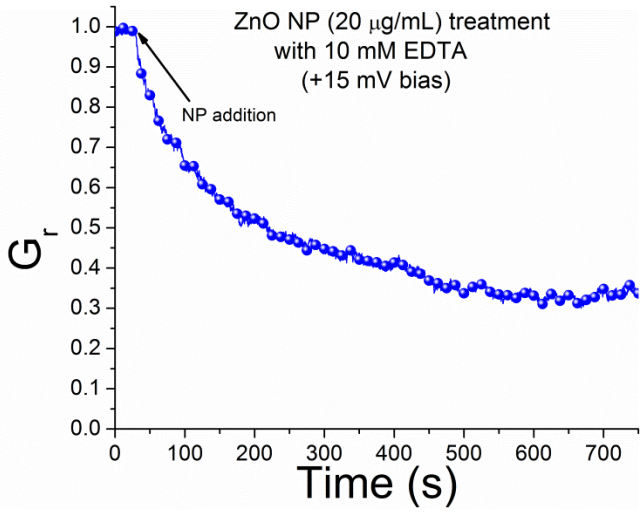


**Figure S3.7 Interactions between ZnO nanoparticles and lysenin channels with EDTA (10 mM) present in the solution reservoirs. EDTA is a strong chelator of $Zn^{2+}$ ions and thus prevents interactions between lysenin nanochannels and zinc ions. Nevertheless, ZnO nanoparticles elicited a strong conductance inhibition of lysenin channels, even with EDTA present, clearly demonstrating that inhibition is due to interactions between ZnO and lysenin, not free zinc ions.**

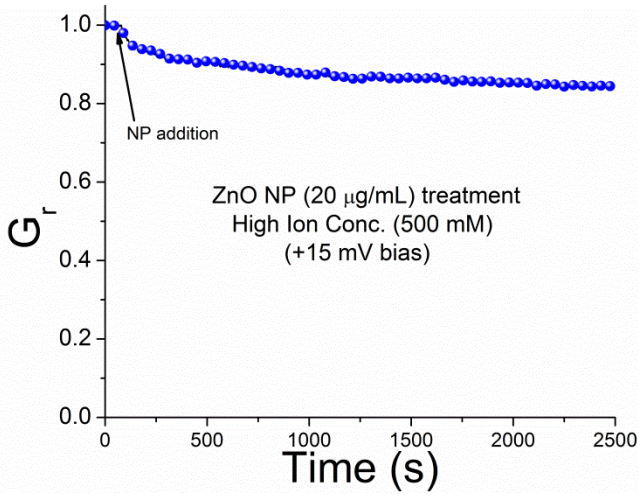


**Figure S3.8 Ionic conductance of lysenin channels in the presence of ZnO nanoparticles while using a significantly higher electrolyte concentration in solution (500 mM). When compared with experiments under low electrolyte solutions (130 mM), the ZnO nanoparticles elicited a much weaker response. The reduction in conductance inhibition may be due to: 1) Debye screening effects that reduce the electrostatic interactions between ZnO nanoparticles and lysenin channels, preventing the initial binding event required for conductance inhibition and 2) increased aggregation of ZnO nanoparticles, which reduces interactions between lysenin channels and ZnO nanoparticles.**

## References

1. Zhang, Y. Y.; Leu, Y. R.; Aitken, R. J.; Riediker, M., Inventory of Engineered Nanoparticle-Containing Consumer Products Available in the Singapore Retail Market and Likelihood of Release into the Aquatic Environment. *Int. J. Environ. Res. Public Health* **2015,** *12* (8), 8717-8743.

2. Sonneville-Aubrun, O.; Simonnet, J. T.; L'Alloret, F., Nanoemulsions: a new vehicle for skincare products. *Adv. Colloid Interface Sci.* **2004,** *108*, 145-149.

3. Magdassi, S.; Grouchko, M.; Kamyshny, A., Copper Nanoparticles for Printed Electronics: Routes Towards Achieving Oxidation Stability. *Materials* **2010,** *3* (9), 4626-4638.

4. Karnaushenko, D.; Makarov, D.; Stober, M.; Karnaushenko, D. D.; Baunack, S.; Schmidt, O. G., High-Performance Magnetic Sensorics for Printable and Flexible Electronics. *Adv. Mater.* **2015,** *27* (5), 880-885.

5. Archana, P. S.; Jose, R.; Vijila, C.; Ramakrishna, S., Improved Electron Diffusion Coefficient in Electrospun TiO2 Nanowires. *J. Phys. Chem. C* **2009,** *113* (52), 21538-21542.

6. McNamara, K.; Tofail, S. A. M., Nanoparticles in biomedical applications. *Adv. Phys.-X* **2017,** *2* (1), 54-88.

7. Nune, S. K.; Gunda, P.; Thallapally, P. K.; Lin, Y. Y.; Forrest, M. L.; Berkland, C. J., Nanoparticles for biomedical imaging. *Expert Opin. Drug Deliv.* **2009,** *6* (11), 1175-1194.

8. Hu, C. M. J.; Zhang, L.; Aryal, S.; Cheung, C.; Fang, R. H.; Zhang, L. F., Erythrocyte membrane-camouflaged polymeric nanoparticles as a biomimetic delivery platform. *Proc. Natl. Acad. Sci. U.S.A* **2011,** *108* (27), 10980-10985.

9. Hsieh, C. T.; Lin, J. S.; Chen, Y. F.; Lin, C. Y.; Li, W. Y., Graphene sheets anchored with ZnO nanocrystals as electrode materials for electrochemical capacitors. *Mater. Chem. Phys.* **2014,** *143* (2), 853-859.

10. Keller, A. A.; McFerran, S.; Lazareva, A.; Suh, S., Global life cycle releases of engineered nanomaterials. *J. Nanopart. Res.* **2013,** *15* (6), 1692.

11. Ahamed, M.; AlSalhi, M. S.; Siddiqui, M. K. J., Silver nanoparticle applications and human health. *Clin. Chim. Acta* **2010,** *411* (23-24), 1841-1848.

12. Teow, Y.; Asharani, P. V.; Hande, M. P.; Valiyaveettil, S., Health impact and safety of engineered nanomaterials. *Chem. Commun.* **2011,** *47* (25), 7025-7038.

13. Hanley, C.; Layne, J.; Punnoose, A.; Reddy, K. M.; Coombs, I.; Coombs, A.; Feris, K.; Wingett, D., Preferential killing of cancer cells and activated human T cells using ZnO nanoparticles. *Nanotechnology* **2008,** *19* (29), 10.

14. Hu, Y. L.; Gao, J. Q., Potential neurotoxicity of nanoparticles. *Int. J. Pharm.* **2010,** *394* (1-2), 115-121.

15. Chen, T.; Yan, J.; Li, Y., Genotoxicity of titanium dioxide nanoparticles. *J. Food Drug Anal.* **2014,** *22* (1), 95-104.

16. Kumar, A.; Pandey, A. K.; Singh, S. S.; Shanker, R.; Dhawan, A., Engineered ZnO and TiO2 nanoparticles induce oxidative stress and DNA damage leading to reduced viability of Escherichia coli. *Free Radical Biology and Medicine* **2011,** *51* (10), 1872-1881.

17. Ivask, A.; Titma, T.; Visnapuu, M.; Vija, H.; Kakinen, A.; Sihtmae, M.; Pokhrel, S.; Madler, L.; Heinlaan, M.; Kisand, V.; Shimmo, R.; Kahru, A., Toxicity of 11 Metal Oxide Nanoparticles to Three Mammalian Cell Types In Vitro. *Curr. Top. Med. Chem.* **2015,** *15* (18), 1914-1929.

18. Seabra, A. B.; Duran, N., Nanotoxicology of Metal Oxide Nanoparticles. *Metals* **2015,** *5* (2), 934-975.

19. Punnoose, A.; Dodge, K.; Rasmussen, J. W.; Chess, J.; Wingett, D.; Anders, C., Cytotoxicity of ZnO Nanoparticles Can Be Tailored by Modifying Their Surface Structure: A Green Chemistry Approach for Safer Nanomaterials. *ACS Sustain. Chem. Eng.* **2014,** *2* (7), 1666-1673.

20. Sharma, V.; Anderson, D.; Dhawan, A., Zinc oxide nanoparticles induce oxidative DNA damage and ROS-triggered mitochondria mediated apoptosis in human liver cells (HepG2). *Apoptosis* **2012,** *17* (8), 852-870.

21. Xia, T.; Kovochich, M.; Liong, M.; Madler, L.; Gilbert, B.; Shi, H. B.; Yeh, J. I.; Zink, J. I.; Nel, A. E., Comparison of the Mechanism of Toxicity of Zinc Oxide and Cerium Oxide Nanoparticles Based on Dissolution and Oxidative Stress Properties. *Acs Nano* **2008,** *2* (10), 2121-2134.

22. Buerki-Thurnherr, T.; Xiao, L. S.; Diener, L.; Arslan, O.; Hirsch, C.; Maeder-Althaus, X.; Grieder, K.; Wampfler, B.; Mathur, S.; Wick, P.; Krug, H. F., In vitro mechanistic study towards a better understanding of ZnO nanoparticle toxicity. *Nanotoxicology* **2013,** *7* (4), 402-416.

23. Kao, Y. Y.; Chen, Y. C.; Cheng, T. J.; Chiung, Y. M.; Liu, P. S., Zinc Oxide Nanoparticles Interfere with Zinc Ion Homeostasis to Cause Cytotoxicity. *Toxicol. Sci.* **2012,** *125* (2), 462-472.

24. Yang, Q. B.; Lin, T. S.; Burton, C.; Park, S. H.; Ma, Y., Physicochemical insights of irradiation-enhanced hydroxyl radical generation from ZnO nanoparticles. *Toxicol. Res.* **2016,** *5* (2), 482-491.

25. Akhtar, M. J.; Ahamed, M.; Kumar, S.; Khan, M. A. M.; Ahmad, J.; Alrokayan, S. A., Zinc oxide nanoparticles selectively induce apoptosis in human cancer cells through reactive oxygen species. *Int. J. Nanomedicine* **2012,** *7*, 845-857.

26. Roopan, S. M.; Kumar, S. H. S.; Madhumitha, G.; Suthindhiran, K., Biogenic-Production of SnO2 Nanoparticles and Its Cytotoxic Effect Against Hepatocellular Carcinoma Cell Line (HepG2). *Appl. Biochem. Biotechnol.* **2015,** *175* (3), 1567-1575.

27. Chavez-Calderon, A.; Paraguay-Delgado, F.; Orrantia-Borunda, E.; Luna-Velasco, A., Size effect of SnO2 nanoparticles on bacteria toxicity and their membrane damage. *Chemosphere* **2016,** *165*, 33-40.

28. Krysanov, E. Y.; Pavlov, D. S.; Demidova, T. B.; Dgebuadze, Y. Y., Effect of nanoparticles on aquatic organisms. *Biol. Bull* **2010,** *37* (4), 406-412.

29. Ai, J.; Biazar, E.; Jafarpour, M.; Montazeri, M.; Majdi, A.; Aminifard, S.; Zafari, M.; Akbari, H. R.; Rad, H. G., Nanotoxicology and nanoparticle safety in biomedical designs. *Int. J. Nanomedicine* **2011,** *6*, 1117-27.

30. Ashcroft, F. M., *Ion Channels and Disease*. Academic Press: San Diego, CA, USA, 1999.

31. Aidley, D. J.; Stanfield, P. R., *Ion Channels. Molecules in Action*. Cambridge University Press: Cambridge, 1996.

32. Bezanilla, F., Voltage-Gated Ion Channels. *IEEE Transactions on Nanobioscience* **2005,** *4* (1), 34-48.

33. Ide, T.; Aoki, T.; Takeuchi, Y.; Yanagida, T., Lysenin forms a voltage-dependent channel in artificial lipid bilayer membranes. *Biochem. Biophys. Res. Communn.* **2006,** *346*, 288-292.

34. Kiyokawa, E.; Makino, A.; Ishii, K.; Otsuka, N.; Yamaji-Hasegawa, A.; Kobayashi, T., Recognition of sphingomyelin by lysenin and lysenin-related proteins. *Biochemistry* **2004,** *43*, 9766-9773.

35. Kwiatkowska, K.; Hordejuk, R.; Szymczyk, P.; Kulma, M.; Abdel-Shakor, A.-B.; Plucienniczak, A.; Dolowy, K.; Szewczyk, A.; Sobota, A., Lysenin-His, a sphingomyelin-recognizing toxin, requires tryptophan 20 for cation-selective channel assembly but not for membrane binding. *Molecular Membrane Biology* **2007,** *24* (2), 121-134.

36. Bokori-Brown, M.; Martin, T. G.; Naylor, C. E.; Basak, A. K.; Titball, R. W.; Savva, C. G., Cryo-EM structure of lysenin pore elucidates membrane insertion by an aerolysin family protein. *Nat Commun* **2016,** *7*, 11293.

37. Podobnik, M.; Savory, P.; Rojko, N.; Kisovec, M.; Wood, N.; Hambley, R.; Pugh, J.; Wallace, E. J.; McNeill, L.; Bruce, M.; Liko, I.; Allison, T. M.; Mehmood, S.; Yilmaz, N.; Kobayashi, T.; Gilbert, R. J.; Robinson, C. V.; Jayasinghe, L.; Anderluh, G., Crystal structure of an invertebrate cytolysin pore reveals unique properties and mechanism of assembly. *Nat Commun* **2016,** *7*, 11598.

38. Bruhn, H.; Winkelmann, J.; Andersen, C.; Andra, J.; Leippe, M., Dissection of the mechanisms of cytolytic and antibacterial activity of lysenin, a defence protein of the annelid *Eisenia fetida*. *Developmental and Comparative Immunology* **2006,** *30*, 597-606.

39. Fologea, D.; Krueger, E.; Mazur, Y. I.; Stith, C.; Okuyama, Y.; Henry, R.; Salamo, G. J., Bi-stability, hysteresis, and memory of voltage-gated lysenin channels. *Biochim. Biophys. Acta, Biomembr.* **2011,** *1808*, 2933-2939.

40. Fologea, D.; Krueger, E.; Lee, R.; Naglak, M.; Mazur, Y.; Henry, R.; Salamo, G., Controlled gating of lysenin pores. *Biophys. Chem.* **2010,** *146* (1), 25-9.

41. Fologea, D.; Al Faori, R.; Krueger, E.; Mazur, Y. I.; Kern, M.; Williams, M.; Mortazavi, A.; Henry, R.; Salamo, G. J., Potential analytical applications of lysenin channels for detection of multivalent ions. *Analytical and Bioanalytical Chemistry* **2011,** *401* (6), 1871-9.

42. Fologea, D.; Krueger, E.; Al Faori, R.; Lee, R.; Mazur, Y. I.; Henry, R.; Arnold, M.; Salamo, G. J., Multivalent ions control the transport through lysenin channels. *Biophys. Chem.* **2010,** *152* (1-3), 40-5.

43. Alanko, G. A.; Thurber, A.; Hanna, C. B.; Punnoose, A., Size, surface structure, and doping effects on ferromagnetism in SnO2. *Journal of Applied Physics* **2012,** *111* (7), 07C321.

44. Hanley, C.; Thurber, A.; Hanna, C.; Punnoose, A.; Zhang, J. H.; Wingett, D. G., The Influences of Cell Type and ZnO Nanoparticle Size on Immune Cell Cytotoxicity and Cytokine Induction. *Nanoscale Research Letters* **2009,** *4* (12), 1409-1420.

45. Shrestha, N.; Bryant, S. L.; Thomas, C.; Richtsmeier, D.; Pu, X.; Tinker, J.; Fologea, D., Stochastic sensing of Angiotensin II with lysenin channels. *Scientific Reports* **2017,** *7* (1), 2448.

46. Bryant, S.; Shrestha, N.; Carnig, P.; Kosydar, S.; Belzeski, P.; Hanna, C.; Fologea, D., Purinergic control of lysenin's transport and voltage-gating properties. *Purinergic Signalling* **2016,** *12* (3), 549-559.

47. Montal, M.; Mueller, P., Formation of Bimolecular Membranes from Lipid Monolayers and a Study of Their Electrical Properties. *Proc. Natl. Acad. Sci. U.S.A* **1972,** *69* (12), 3561-3566.

48. Krueger, E.; Bryant, S.; Shrestha, N.; Clark, T.; Hanna, C.; Pink, D.; Fologea, D., Intramembrane congestion effects on lysenin channel voltage-induced gating. *Eur. Biophys. J.* **2016,** *45* (2), 187-194.

49. De Colibus, L.; Sonnen, A. F.; Morris, K. J.; Siebert, C. A.; Abrusci, P.; Plitzko, J.; Hodnik, V.; Leippe, M.; Volpi, E.; Anderluh, G.; Gilbert, R. J., Structures of lysenin reveal a shared evolutionary origin for pore-forming proteins and its mode of sphingomyelin recognition. *Structure* **2012,** *20* (9), 1498-507.

50. Misra, S. K.; Dybowska, A.; Berhanu, D.; Luoma, S. N.; Valsami-Jones, E., The complexity of nanoparticle dissolution and its importance in nanotoxicological studies. *Sci. Total Environ.* **2012,** *438*, 225-232.

51. Berg, J. M.; Romoser, A.; Banerjee, N.; Zebda, R.; Sayes, C. M., The relationship between pH and zeta potential of similar to 30 nm metal oxide nanoparticle suspensions relevant to in vitro toxicological evaluations. *Nanotoxicology* **2009,** *3* (4), 276-283.

52. Schwegmann, H.; Feitz, A. J.; Frimmel, F. H., Influence of the zeta potential on the sorption and toxicity of iron oxide nanoparticles on S. cerevisiae and E. coli. *J. Colloid Interface Sci.* **2010,** *347* (1), 43-48.

53. Patil, S.; Sandberg, A.; Heckert, E.; Self, W.; Seal, S., Protein adsorption and cellular uptake of cerium oxide nanoparticles as a function of zeta potential. *Biomaterials* **2007,** *28* (31), 4600-4607.

54. Yang, H.; Liu, C.; Yang, D. F.; Zhang, H. S.; Xi, Z. G., Comparative study of cytotoxicity, oxidative stress and genotoxicity induced by four typical nanomaterials: the role of particle size, shape and composition. *J. Appl. Toxicol.* **2009,** *29* (1), 69-78.

55. den Hartog, G. J. M.; Qi, S. F.; van Tilburg, J. H. O.; Koek, G. H.; Bast, A., Superoxide anion radicals activate hepatic stellate cells after entry through

chloride channels: A new target in liver fibrosis. *Eur. J. Pharmacol.* **2014,** *724,* 140-144.

56. Sahoo, N.; Hoshi, T.; Heinemann, S. H., Oxidative Modulation of Voltage-Gated Potassium Channels. *Antioxid. Redox Signal.* **2014,** *21* (6), 933-952.

57. Yang, Z.; Liu, Z. W.; Allaker, R. P.; Reip, P.; Oxford, J.; Ahmad, Z.; Ren, G., A review of nanoparticle functionality and toxicity on the central nervous system. *Journal of The Royal Society Interface* **2010,** *7* (Suppl 4), S411-S422.

58. Shah, B.; Kona, S.; Gilbertson, T. A.; Nguyen, K. T., Effects of Poly-(lactide-co-glycolide) Nanoparticles on Electrophysiological Properties of Enteroendocrine Cells. *J. Nanosci. Nanotechnol.* **2011,** *11* (4), 3533-3542.

59. Liu, Z. W.; Ren, G. G.; Zhang, T.; Yang, Z., Action potential changes associated with the inhibitory effects on voltage-gated sodium current of hippocampal CA1 neurons by silver nanoparticles. *Toxicology* **2009,** *264* (3), 179-184.

60. Valdiglesias, V.; Costa, C.; Kilic, G.; Costa, S.; Pasaro, E.; Laffon, B.; Teixeira, J. P., Neuronal cytotoxicity and genotoxicity induced by zinc oxide nanoparticles. *Environ. Int.* **2013,** *55* (Supplement C), 92-100.

# CHAPTER FOUR: CONTROLLED DEFECT ENGINEERING OF ZNO NANOPARTICLES MODULATES PROPERTIES FOR POTENTIAL BIO-IMAGING AND OPTOELECTRONIC APPLICATIONS

Josh E. Eixenberger†, Catherine B. AndersΩ, Katelyn Wada‡, Kongara M. Reddy‡, Raquel J. Brown⊥, Jonathan Moreno-Ramirez‡§, Ariel E. Weltner⁋, Chinnathambi Karthik⁋, Dmitri A. Tenne‡, Daniel Fologea‡ and *Denise G. Wingett†£

†Biomolecular Sciences Graduate Programs, ‡Department of Physics, ⊥Biomolecular Research Center, ⁋Micron School of Material Science and Engineering, £Department of Biological Sciences, Boise State University, Boise, ID 83725, USA , ΩIdaho Veterans Research & Education Foundation – Boise VA Medical Center, 500 W Fort St, Boise, ID 83702, USA, § Riverstone International School, Boise, ID 83716, USA

*Email: denisewingett@boisestate.edu

Advanced Functional Materials (Submitted Nov. 2018)

Publisher Wiley

No significant changes were made to this submitted publication.

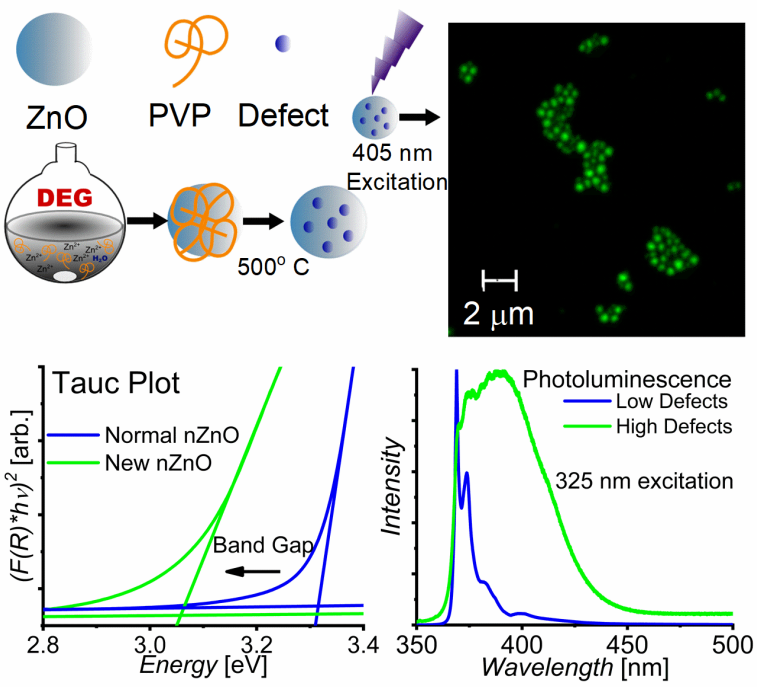



## Abstract

Many attributes of ZnO nanoparticles (nZnO) have led to their utilization in numerous electronic devices and biomedical technologies. nZnO fabrication methods can create a number of intrinsic defects that modulate their properties and can be exploited for the intended purpose. Here we developed a procedure to control the defects states of pure nZnO that are theorized to contribute to the n-type conductivity of the material. These defects reduced the nanoparticle (NP) band gap to ~3.1 eV and generated strong emissions in the violet to blue region while also minimizing the defects responsible for the more common broad green emissions. Several characterization techniques including TGA, FT-IR, XPS, TEM, Raman, photoluminescence and ICP-MS were employed to verify the sample purity, assess how modifications in the synthesis procedure affect the various defects states and understand how these alterations impact the physical properties. The changes to the physical properties prompted investigations into using these NPs for bio-imaging purposes. We demonstrate the ability to utilize traditional

fluorescence microscopy techniques to excite the nZnO with a 405 nm laser and detect their emissions during live-cell imaging experiments. This work lays the foundation for the use of these NPs in various bio-imaging and potential optoelectronic applications.

## Introduction

Nanomaterials composed of ZnO are highly produced and extensively studied due to their promising attributes in numerous fields. ZnO nanomaterials (NMs) are considered for various potential cancer treatment options, water treatment applications and electronic devices.[1-3] The flexible nature of NMs, specifically the ability to control physical properties such as size, surface chemistry, catalytic activity and defect structure, makes them suitable for many novel devices. Researchers often focus on how these properties relate to ZnO nanoparticle (nZnO) toxicity; especially as they appear to be selectively toxic towards cancer cells when compared to their normal non-transformed counter-parts.[4] Although there has been a wealth of data collected about nZnO properties and toxicity, the mechanism of toxicity and cell selectivity remains controversial as it is not fully understood. The ability to fluorescently track nZnO within biological systems is an avenue that should be further explored as it would likely facilitate a better understanding of nZnO interactions with various cell types and cancer.

Numerous semiconducting nanoparticles (NPs) have generated great interest as biological labels due to their small size, photo-stability and relatively long fluorescence lifetimes.[5, 6] The most traditional systems use cadmium chalcogenides as their emission is tunable through size modulation and generally have narrow emission spectra. Unfortunately these particles are toxic towards biological systems through the release of $Cd^{2+}$ ions; reportedly highly toxic in the nanomolar range.[7] In contrast, nZnO display

relatively low toxicity, at an even higher micro-to-millimolar range.[8,9] As nZnO are comparatively less toxic, their potential use in bio-imaging has received considerable attention and yet only modest progress has been made to date.

Using nZnO as a biological labelling tool is partially limited by the need to use UV excitation sources coupled with corresponding emission spectra of nZnO that consists of two peaks; one generally in the UV range (correlating to near band emissions of ~3.37 eV or ~368 nm) and one with the commonly reported broad green emission (~500-700 nm). True UV excitation sources (100 nm-380 nm) are generally absent in conventional fluorescence imaging instruments with most traditional fluorescence microscopy techniques using excitation wavelengths of 405 nm or longer, which is insufficient to excite nZnO as it is below the band gap energy of ZnO. Monitoring UV emissions with standard fluorescent imaging equipment is often not possible, which limits the ability to study nZnO in biological systems. Additionally, the broad green emission of nZnO is theorized to originate from surface defects, such as oxygen vacancies, that can be quickly quenched by transformations in solution such as hydroxide formations and conversion to zinc carbonate/phosphate species.[10-12] An additional complication to targeting the broad green emission region for fluorescence microscopy techniques is that emissions in this region of the spectrum is broad enough to overlap with other fluorophores commonly used in cell and tissue research. Therefore, targeting the broad green emission spectra of nZnO for imaging purposes may not be suitable for many applications.

Some of the aforementioned drawbacks have been overcome through modifications of nZnO, creating novel fluorescent particles through methods such as

encapsulating dyes including fluorescein isothiocyanate (FITC), coating nanoparticles (NPs) with polymers, and doping elements into nZnO to modulate the band gap.[13-15] However, these modifications may impact other properties of nZnO, potentially altering their toxicity mechanism and making them unsuitable for specific types of studies. While these avenues may shed some light into understanding the interplay of nZnO with various cell types, conclusions drawn from these approaches do not necessarily reflect how unmodified nZnO interacts with cells.

In addition to biological applications, nZnO are well suited for optoelectronic devices. Modulating the absorbance, emission spectra and charge carriers in nZnO has been a goal for optoelectronic device applications. To these ends, one approach has been to dope various elements in the crystal lattice of ZnO,[16-17] while other researchers have sought to improve ZnO performance by producing highly oriented and defect-free ZnO nanomaterials. Producing ZnO materials free of defects is hard to achieve, especially at the nanoscale; some have focused their investigations on ways to reduce the defects produced when synthesizing nZnO, while others have actively pursued ways to utilize the various defects states that are inherent to ZnO.

Control of ZnO NM defect states is achieved through various means such as growth on substrates, annealing in various atmospheric conditions and via numerous deposition techniques.[18-21] For nZnO specifically, achieving control of various defects in wet chemical methods can be challenging. Many reports have focused on the green luminescent broad band produced through differing methods, but the precise defect states or surface species responsible are still controversial, making precise control difficult due to lack of a known mechanism.[22-24]

In this report, we pursued controlling defects of highly pure nZnO that affect the emission spectra near the band gap, theoretically creating shallow donors such as zinc interstitials. By controlling these defects, the emission spectra were red-shifted and broadened, creating strong emissions up to ~430 nm. Additionally, the optical band gap was red-shifted down to ~3.1 eV allowing excitation sources, such as a 405 nm laser used in confocal microscopy, to produce sufficient emissions to image the particles without any other modifications. Through variations in the wet chemical synthesis procedure, we demonstrate that the described defect states can be systematically controlled for applications in bio-imaging and potentially optoelectronic devices.

## Results and Discussion

### ZnO Nanoparticle Synthesis and Characterization

PVP is known to modify the structure and morphology of many different NMs, including metal oxide NPs.[25] The inclusion of PVP in synthesis procedures has been shown to act as a surfactant, stabilizing agent, dispersant, binding agent and a capping agent to obtain better dispersions of hydrophobic materials.[25] In this report, it was determined that the PVP content, annealing temperature and the ratio of water to zinc acetate (ZnAc) were the three key factors that affect the defect states of nZnO. The as-prepared nZnO, to which various amounts of PVP were added pre-synthesis, produced nZnO with an average crystal sizes near 10 nm in all cases (Figure S4.1a-c). Similar methods, though lacking PVP, have demonstrated the ability to control the average crystal size of the nZnO by varying the amount of water added during synthesis to produce nZnO with a broad range of sizes - from ~4 nm to ~50 nm. The addition of PVP into the solution with the zinc precursor (2:1 PVP:ZnAc; w/w) removed the ability to

control the size of the particles, regardless of the ratio of water to zinc acetate. For this reason, any changes in the physical properties of these newly synthesized nZnO are not size related effects. It is possible that PVP is coordinating the NPs in the cavities of the polymer during crystal growth and/or capping the particles and restricting their growth, as theorized in reports for other types of NPs.[25]

In our procedure described here, the nZnO produced have a similar morphology to that in other reports; nearly spherical ZnO crystals that form spherical aggregates (Figure S4.1). One consequence of including PVP in the synthesis is that the as-prepared NPs retained some of the polymer and other species from the precursors and solvents. Annealing was performed to remove residual polymer and precursor species to obtain a highly pure nZnO sample. The Thermogravimetric Analysis (TGA) plot of nZnO synthesized with PVP (Figure 4.1a) demonstrates that after only 10 minutes of annealing at 450˚ C, no additional mass loss is evident, even when increasing the temperature to 575˚ C. To confirm the complete loss of retained chemical species, FTIR was utilized to evaluate the removal of the retained chemical species in the sample when annealed at various temperatures for 10 minutes. As seen in Figure 4.1b, after reaching 450˚ C, all the bands associated with the precursors and PVP have effectively been removed and even the band associated with O-H stretching group at ~3400 $cm^{-1}$ is almost entirely eliminated. XPS confirmed the results of the post annealed samples, with only zinc, oxygen, and carbon atoms (associated with carbon dioxide) detected in the spectra (SI Figure S4.2).

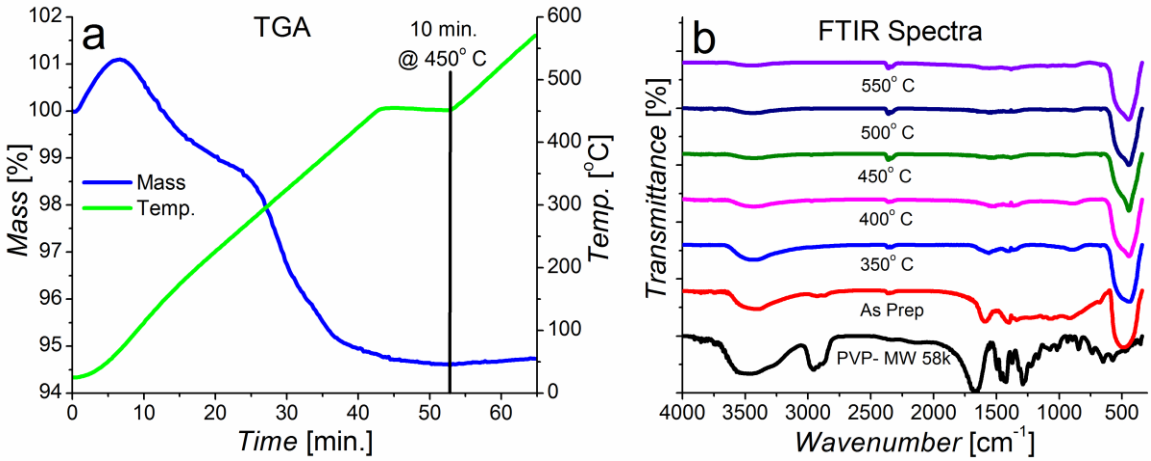


**Figure 4.1 (a) Thermogravimetric Analysis plot of nZnO synthesized with Polyvinylpyrrolidine (PVP) demonstrating the mass loss is complete after 10 minutes of annealing at 450˚ C. (b) FTIR spectra of PVP, the as-prepared nZnO and annealed-nZnO at various temperatures for 10 minutes. FTIR data confirms that after 10 minutes of annealing at 450˚ C that no other chemical species from the precursors are retained with the NPs.**

As annealing can induce crystal growth, XRD analysis was performed and it was determined that the average crystal was ~15 nm; an increase of only ~5 nm (SI Figure S4.1d-f). The modest increase in nZnO size was confirmed with TEM. It was noteworthy that upon thermal treatment the color of the samples visibly changed from an off-white to light yellow. It was this observation that prompted further investigation into the physical and optical properties of these nZnO.

Raman spectroscopy was employed to investigate the potential changes in vibrational properties, verify the sample purity and assess defects induced during the synthesis and annealing procedure. Figure 4.2, shows the low temperature (10 K) resonant UV Raman spectra (325 nm excitation) for bulk ZnO and three samples of the nZnO produced with varying PVP to zinc acetate ratios. The $E_1$ longitudinal (LO) phonon modes are enhanced under resonant conditions. In the bulk ZnO sample, the first-order LO phonon peak appears at 584 $cm^{-1}$ and the second-order (two-phono) peak appears at 1164 $cm^{-1}$.[26-28] Interestingly, a systematic downward shift of the LO phonon peaks was

observed with increasing PVP content. The initial downward shift of the peak, when compared to the bulk nZnO sample (580 vs 584 $cm^{-1}$), is likely due to phonon confinement associated with the smaller particle sizes.[29-31] However, as discussed above, all the nZnO samples produced were ~15 nm in crystal size, so the continued shift of the peak, down to 574 $cm^{-1}$ for the sample with the highest PVP content, is not likely due to phonon confinement from decreasing crystal size. The systematic shift of the phonon peak correlates with the increasing intensity of the peak that appeared in the spectra at 470 $cm^{-1}$. The $E_2$ (High) phonon mode that should appear at 437 $cm^{-1}$ was ruled out as being responsible for the peak found at 470 $cm^{-1}$, due to the large frequency difference, the fact that it was not observed in the bulk ZnO and is not commonly seen in resonant Raman spectra of ZnO.[28,32] As we noted, the intensity of this peak increased with increasing PVP content. We attribute this peak to defect(s) present in the nZnO because all the residual impurities retained from the synthesis procedure were removed during the annealing process. Increasing amounts of defects would also explain the continued shift of the LO phonon modes to lower wavenumbers. As the defect concentration increases, the phonon mean free path would decrease due to scattering by defects, therefore shortening the effective phonon confinement length and inducing the observed systematic shift of the peak,[33] similar to size related phonon confinement. To further investigate the defect(s) responsible for the origin of the peak found at 470 $cm^{-1}$, photoluminescence (PL) was employed.

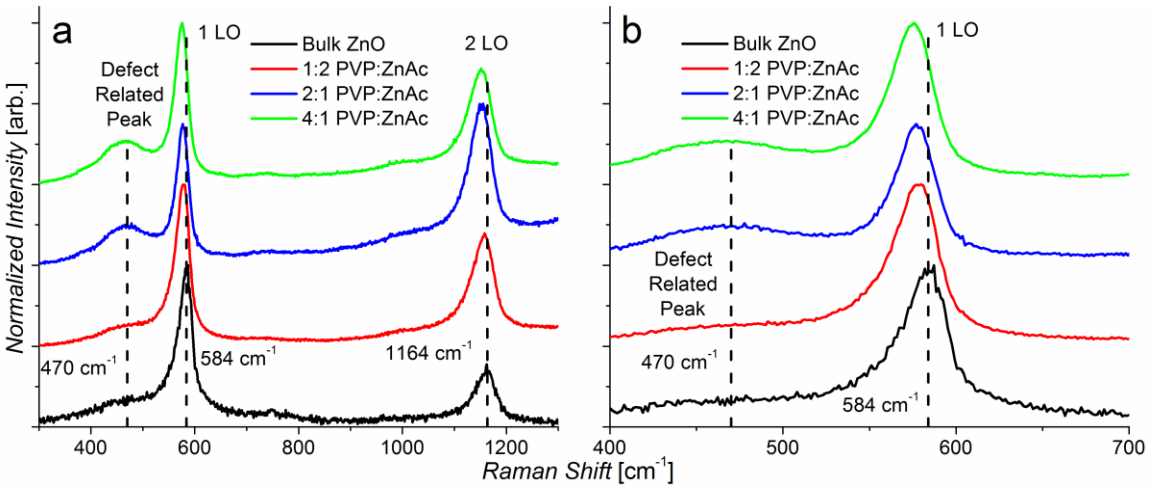


**Figure 4.2 (a) Low temperature (10 K) resonant Raman spectra (325 nm laser) of bulk ZnO and the nZnO synthesized with various amount of PVP. Spectra shows a systematic shift of the LO phonon peaks as the defect related peak centered at 470 $cm^{-1}$ increases in area. (b) Zoomed in spectra of the defect related peak and the 1 LO phonon mode to highlight the systematic shift of the peak as the defect related peak increases in area. This systematic shift is likely due to phonon confinement due to increases in defects present in the ZnO NPs.**

Photoluminescence (PL) is often utilized to assess nZnO-associated defects as they produce various energy states and optical transitions that are within the band gap region. Numerous papers have reported on how the different emission peaks relate with various defects,[32, 34-39] but many of the conclusions remain controversial. In our attempt to determine the origin of the defects, low temperature (10 K) PL was collected and associated with the energy transition modes commonly reported in the literature. Given the systematic shift of the LO phonon modes and the new peak that was observed in the Raman spectra, PL was first collected for samples that have various ratios of PVP to zinc acetate (PVP:ZnAc; w/w), while water content and annealing temperature were held constant. As seen in Figure 4.3a, varying the ratio of PVP systematically altered the PL emission spectra as it did in Raman spectroscopy. Modest changes were noted in the lower PVP:ZnAc ratios, but a significant broadening of the emission peak evolved as the ratio increased. At the highest PVP ratios, the difference in PL emissions was negligible.

As such, subsequent synthesis studies varying the annealing temperature and water content utilized the 2:1 PVP:ZnAc for the synthesis.

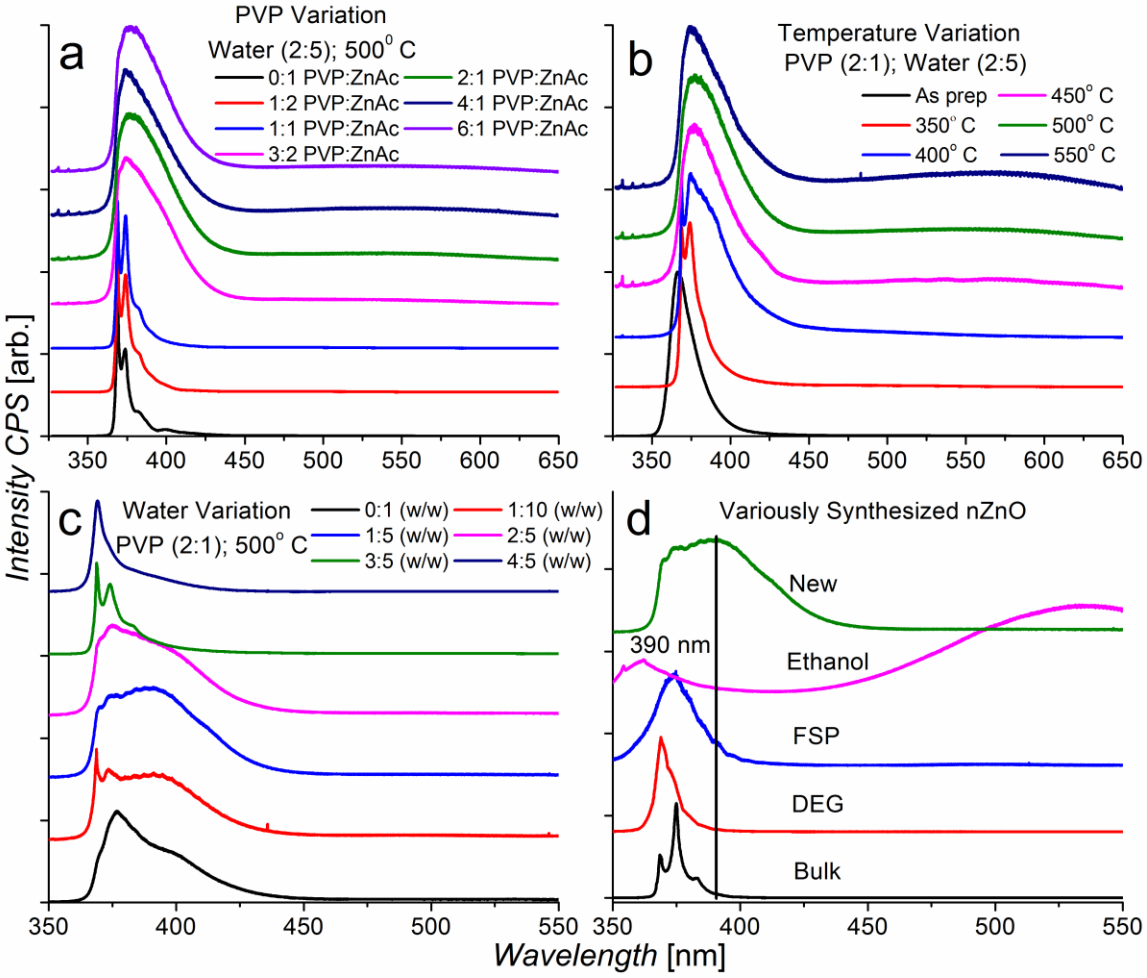


**Figure 4.3 Low temperature Photoluminescence (PL) spectra of the nZnO synthesized by varying different parameters in the synthesis procedure. (a) PL spectra of the nZnO synthesized with various amounts of PVP while all other parameters are kept constant. At low PVP:Zinc Acetate (ZnAc) ratios, little change in the PL spectra is noted. As the amount increases, the well- defined peaks broaden and extend into the visible spectrum. (b) PL spectra of the nZnO annealed at various temperatures. The unannealed sample spectra extends further into the UV range, likely due to the presence of various retained species from the synthesis procedure. As the annealing temperature increase, the main peak in the spectra red-shifts and broadens out to ~450 nm. At the highest temperature used, the broad green emission, commonly reported on nZnO, becomes apparent. (c) PL spectra of the nZnO with various amounts of water added in the synthesis. At relatively high additions of water, the main broad peak narrows likely due to changes from a zinc rich environment to a more balanced oxygen to zinc environment. (d) PL spectra of ZnO NPs synthesized using various methods (ethanol as the solvent, Flame spray pyrolysis (FSP),**

**diethylene glycol as the solvent (DEG) and micron sized (Bulk) ZnO) to demonstrate the extreme difference of the new nZnO compared to other commonly used methods.**

Utilizing the nZnO sample produced with a PVP to zinc acetate ratio of 2:1, additional PL spectra were obtained to evaluate how the changes in surface chemistry, from annealing at various temperatures, impacted the emissions of the sample. As seen in Figure 4.3b, the as-prepared sample's PL spectrum has a peak centered at ~365 nm, which is potentially influenced by the retained species from the precursors on the surface of the particles. However, even after annealing at 350˚ C, the temperature at which the majority of the impurities were removed (Figure 4.1), the PL emission has an apparent red-shift and the peaks are better defined. Once annealing temperature reaches 400˚ C, the PL emission peak starts to broaden and extends into the visible region. Since the samples annealed at or above 450˚ C are highly pure nZnO, the origin of the visible emission is likely due to defects in the crystal structure and not from interactions between ZnO and retained chemical species from the precursors. At annealing temperatures above 500˚ C, only modest changes are observed in the violet/blue range of the PL spectra and the broad defect-related green emission peak around 575 nm, often attributed to oxygen vacancies,[40] becomes evident. Since the focus of this report is primarily to obtain a highly pure nZnO, relatively free of defects related to the broad green emission, all subsequent samples were made with a 2:1 PVP:ZnAc ratio and annealed at 500˚ C.

The final component varied in the synthesis procedure was the volume of water added to the solution (Figure 4.3c). According to published reports on a similar method, the precise control of the nZnO crystal size is dependent upon the ratio of water to zinc acetate,[41] as water is a source for the oxidation of the zinc ions during the Ostwald ripening process. As discussed previously, there were no changes to the crystal size found

by varying the amount of water added during this synthesis procedure and therefore we ruled out effects due to alterations in the crystal size. Surprisingly, it was observed that the ratio of water to zinc acetate had a more significant impact on the formation of defect states than the ratio of PVP to ZnAc or the annealing temperature (Figure 4.3c). Low ratios of water in the synthesis procedure create a zinc-rich environment, potentially allowing for the production of intrinsic defects such as interstitials and antisites, as well as large portions of the crystal surface terminating in zinc atoms. A systematic change in the PL emission was demonstrated but it was noted that increasing amounts of water drastically reduced the strong emission near and above 400 nm. The single emission peak at 368 nm, which correlates with the commonly reported near-band-edge emission, is the only significant peak noted at higher water to ZnAc ratios. Its presence could be due to the reduction of zinc to oxygen ratios, creating a more balanced zinc to oxygen environment, therefore, allowing for better oxidation and formation of the crystals. From these results, we utilized the particles made with a 1:5 water to zinc acetate (w/w) ratio for fluorescence imaging studies.

The systematic control of PL emission spectra associated with nZnO was achieved by varying the PVP content, annealing temperature and water ratios. To demonstrate the significant changes in the defect content utilizing this new method, the PL emission spectra of other ZnO NPs, synthesized using a variety of methods, were also plotted and compared with our nZnO sample found to contain the strongest emissions in the violet/blue region (Figure 4.3d). A good majority of papers published have focused on the defects related to the broad green emissions observed near 575 nm in nZnO. This emission is generally attributed to oxygen vacancies and several of these reports focus on

the origin of this feature and ways to induce its formation. However, as the inclusion of PVP largely restricts the formation of the defects responsible for this broad peak in this synthesis procedure, we chose to further investigate the emission in the 365-450 nm range induced by this method.

In order to get reasonably well assigned peak positions, PL emission spectra with well-defined peaks were first deconvoluted. These peak positions were then assigned to the spectra generated from the nZnO that contained a relatively large number of defects and broad peaks in the violet to blue region. As seen in Figure 4.4a, only four significant peaks were found that contribute to the emissions of the sample produced with a low number of defects. The main peak at 3.36 eV (369 nm) is related to the band gap of the material and the peak found at 3.32 eV (374 nm) is attributed to free excitons.[36] The peak found at 3.24 eV (383 nm) has been reported as a phonon replica of the exciton peak and the last peak found at 3.07 eV is often attributed to zinc vacancies. In contrast, the sample with a relatively high number of defects (Figure 4.4b) was determined to contain seven different peaks. The main contributors to the broadening of the emissions were found at positions that have been reported to be related to transitions involving zinc interstitials and zinc vacancies. The three new major peaks near 3.14 eV, 3.07 eV and 2.97 eV are often attributed to transitions from zinc interstitials to the valence band, the conduction band to zinc vacancies and the conduction band to oxygen interstitials respectively.[36] It is also possible that some of these emissions may arise from interface traps as reported for ZnO thin films,[42] as the crystals are bound together in larger aggregates. However, there has been no clear consensus on which defects are responsible for the observed emission in this region. Various experimental procedures have assigned specific peak positions to

the various native defect states, whereas reports relying on theoretical calculations have demonstrated that some of these defects are unlikely to occur due to diffusion rates and the required formation energies.[22-24] Regardless of the origin of the defects, many are regarded as donors in the n-type conductivity of ZnO. Since a relatively high number of these defects are present, we wanted to evaluate how these defects affect the band gap of our new samples.

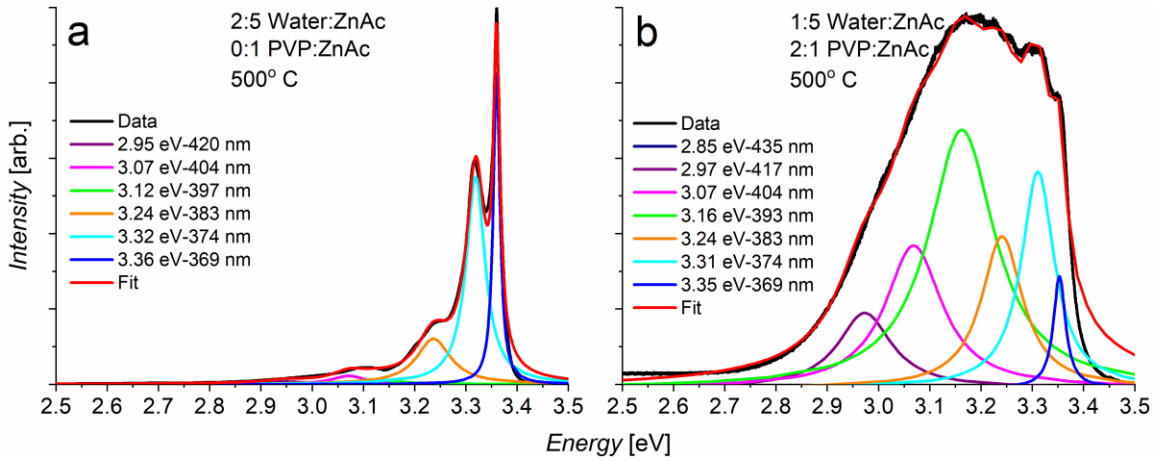


**Figure 4.4 Deconvolution of the low temperature photoluminescence spectra of nZnO synthesized with (a) no PVP and (b) a 2:1 (w/w) PVP to zinc acetate ratio. (a) The NPs with low defect states and well-defined peaks were first deconvoluted to assign positions and acquire reasonable peak widths for the near band edge related emissions. (b) The nZnO sample with a relatively high number of defects shows multiple peaks related to various defects formed during the new synthesis procedure.**

UV-Vis diffuse reflectance spectra were recorded to determine the influence these defects have on the optical band gap of the material. For reference, nZnO produced using the most similar reported method was plotted against some of the new samples. As can be seen in Figure 4.5, the samples produced using different ratios of PVP and annealed at 500˚ C induce a significant shift of the band gap. The non-annealed sample that utilizes the most similar synthesis procedure produced nZnO with a band gap estimated at ~3.31 eV, which is close to the commonly excepted value of 3.37 eV. However, the samples

produced with the new method that have relatively high concentrations of defects, created a dramatic shift of the band gap to as low as 3.08 eV. This change of nearly 0.3 eV from the commonly accepted value of the band gap is usually obtained through doping of other elements into the crystal lattice.

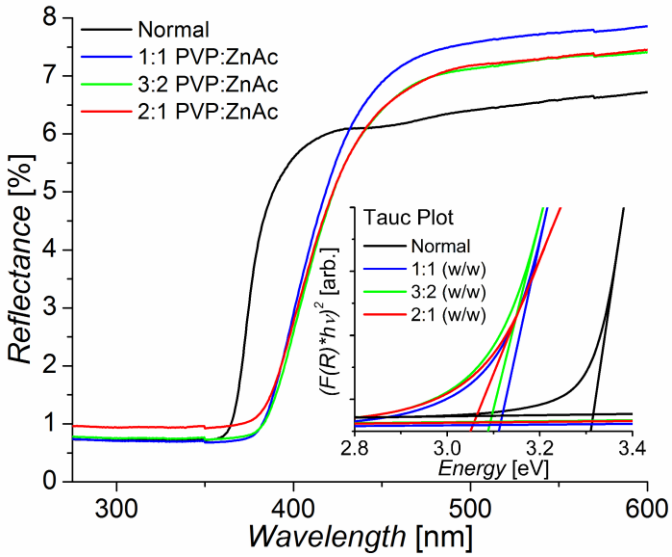


**Figure 4.5 UV-Vis spectra of the new nZnO synthesized with various amounts of PVP compared to the most similar reported method using DEG as a solvent. The UV-Vis spectra was converted into a Tauc Plot (inset) to determine the optical band gap of each sample. The DEG method produced nZnO with an optical band gap of ~3.31 eV whereas the new method shifted the optical band gap to below 3.1 eV.**

To verify the lack of metal impurities, ICP-MS measurements were performed. When compared to the ~2700 ppb of zinc ions from the nZnO, less than 1 ppb of metal contamination was detected (Table S4.1). Taken together, these evaluations on the new nZnO led us to conclude that the alterations in the properties of the NPs are due to defects induced by this synthesis method and are not related to changes in the crystal size, retained chemical species or impurities. Since the optical band gap had such a dramatic shift due to these defects and a relatively narrow emission was created in the visible region, studies were performed using these new nZnO for bio-imaging applications.

Fluorescence Imaging

Fluorescence microscopy was employed to assess whether the new nZnO could be imaged based on their changes in optical properties and the observed shift of the optical bandgap to ~3.1 eV (400 nm). Confocal microscopy is commonly used in biological imaging and the instrument is generally configured with a 405 nm laser to image fluorescent dyes such as DAPI or Hoechst that stain the nuclei of cells. Since the band gap of the new nZnO is near 400 nm, a 405 nm laser was used as an excitation source. Figure 4.6a shows the emission spectra recorded using the confocal microscope. When compared to the broad green emission spectra of nZnO, a relatively narrow emission peak was recorded for this new nZnO and is easily distinguishable from other commonly used fluorescent stains. To demonstrate that the fluorescence stems from the NPs, fluorescence and bright field images were collected by individual detectors and overlaid (Figure 4.6b-d). Additional images that were acquired with higher magnification and resolution show the large agglomerates are comprised of the smaller individual aggregates that are seen in the TEM images (SI Figure S4.3).

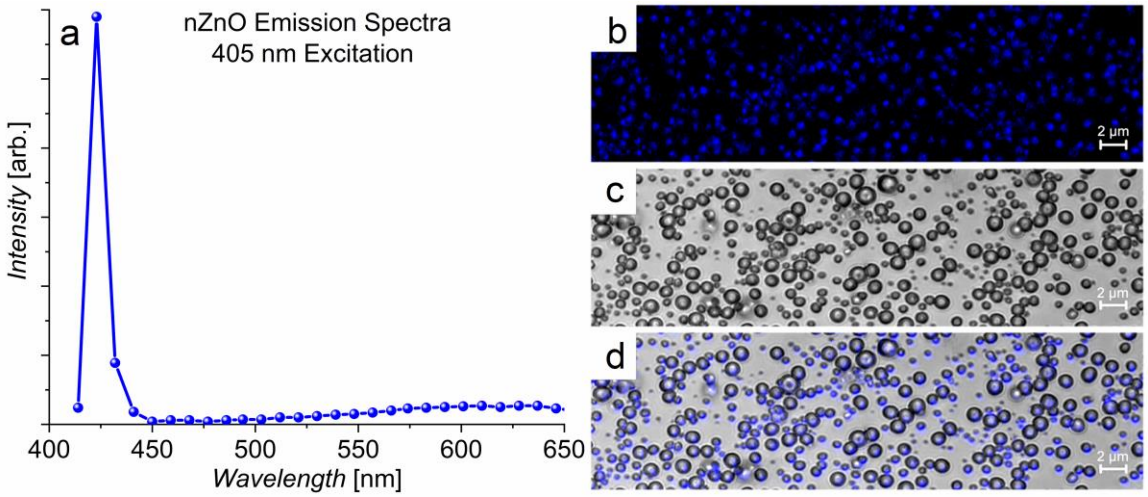


**Figure 4.6 (a) The emission spectra of the nZnO recorded with a confocal microscope using a 405 nm laser as an excitation source. Using a 100x objective, the**

**fluorescence image (b) of the nZnO and bright field (c) images were collected and overlaid (d) to demonstrate that the fluorescence is from the new nZnO.**

Another obstacle to the development of new imaging modalities is photobleaching. Photobleaching is the irreversible alteration of a dye or fluorophore leaving it unable to fluoresce and is a common issue in immunofluorescent imaging. The emergence of fluorescent quantum dots, such as CdSe, demonstrate that NMs hold certain advantages over other more traditionally used fluorescent stains, such as their narrow emission spectra, longer fluorescence decay time and their ability to resist photobleaching.[5] In order to assess the ability of our new nZnO to resist photobleaching, their fluorescent signal was monitored over time during continuous exposer to laser light. Specifically, nZnO were excited with a 405 nm laser for twenty minutes and single plane images were acquired every minute. Time series were collected utilizing different objectives, and regardless of the magnification, no changes in fluorescence were detected (Figure 4.7). Since the images might appear to be replicates, each time series was exported into a video format to further demonstrate the stability of the NPs over time (See SI Video).

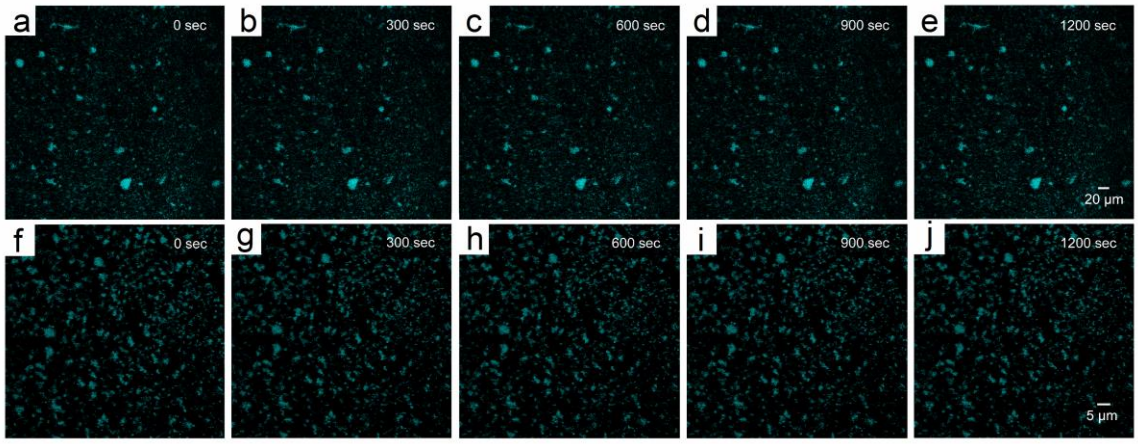


**Figure 4.7 Times series fluorescent images of the nZnO over a 20 minute period with a (a-e) 20x objective and a (f-j) 40x objective. The NPs were subjected to 20**

**minutes of laser exposure and no apparent decrease in fluorescence intensity was noted, demonstrating their resistance to photobleaching. Like quantum dots, the fluorescence stems from the physical properties of the NPs and is proposed to stem from transitions between energy levels due to the defects present in the samples.**

Many of the problems associated with using nZnO in bio-imaging are due to the broad green emission peak associated with surface defects. When introduced into biological media, various components such as carbonates and phosphates react with the surface of nZnO[10-12, 43, 44] and can potentially reduce or completely remove the fluorescence associated with surface defects. In our new nZnO, the defects in this system can persist throughout the crystal lattice, such as zinc interstitials, and perhaps stabilize their ability to fluoresce even in cellular media. Having a pure, unmodified and naturally fluorescent nZnO sample that is excitable with a laser source commonly available in fluorescent microscope systems can expand the use of nZnO in fluorescence imaging. In addition, a stably fluorescent nZnO will also facilitate research focused on understanding nZnO interactions with living systems.

In order to demonstrate the ability to image nZnO in cellular media conditions, live-cell imaging was performed using T47D breast cancer cells. The cells were treated with 30 μg/mL of nZnO and incubated for either 2 or 24 hours. Cells were then stained with CellMask Orange Plasma Membrane for 30 minutes prior to imaging. For a control, untreated T47D cells were stained with CellMask Orange only and imaged using the same configuration and laser settings to rule out any auto-fluorescence generated by the cells in the nZnO channel. As seen in Figure 4.8, the untreated cells have little to no apparent fluorescence in the nZnO channel. After 2 hours of incubation, a few nZnO are seen in the same plane as the cells and appear to randomly settle down and associate with the membrane of the cells. No apparent changes in cellular morphology were noted at this

time point. Surprisingly, after 24 hours of nZnO exposure, no particles were found around the exterior of the cells, and in stark contrast to the fluorescence observed at 2 hours, the only fluorescence detected appears to be from nZnO that have been internalized within the plasma membrane. It is unlikely that every NP was internalized by the cells, yet no particles could be found in the exterior. It is possible that the non-internalized nZnO underwent dissolution or transformed into zinc carbonate or hydroxide species and were no longer fluorescent. However, many NPs were still detectable in the interior of the cells after 24 hours and may resist degradation upon cellular internalization. Another noteworthy feature from this experiment was that the morphology of the T47D cells changed dramatically. The cells rounded up and appear to be detaching from the culture plate. Furthermore, cells showed evidence of blebbing; the bulging of the cell membrane, characteristic of cytoskeletal breakdown that accompanies apoptosis.

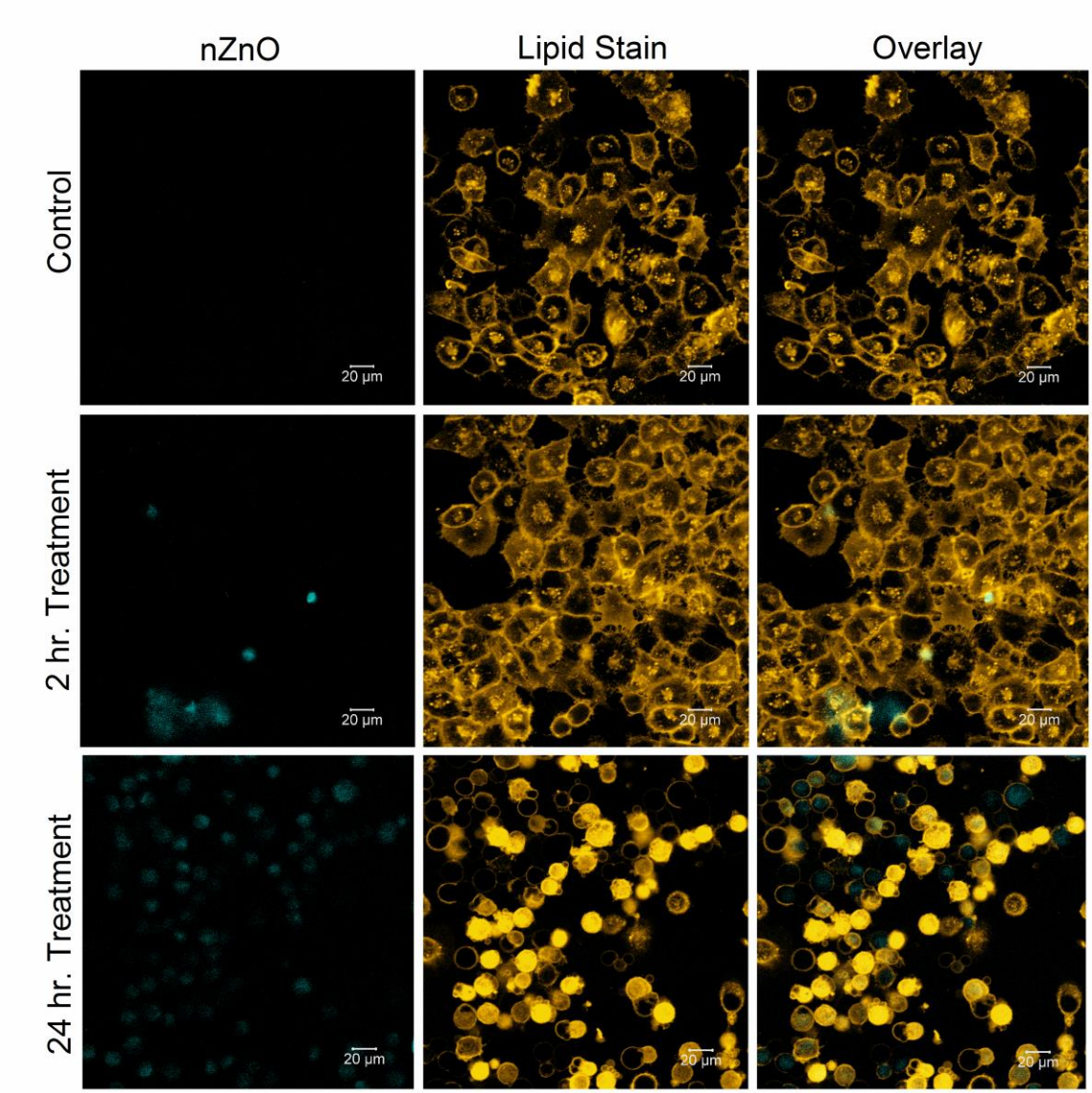


**Figure 4.8 Confocal images of T47D (breast cancer) cells stained with CellMask Orange. The top row depicts untreated T47D cells to assess any auto-fluorescence generated using the same laser settings in the 405 nm laser channel. The second row depicts the T47D cells after 2 hours of nZnO treatment. Little to no change in cell morphology is noted. The bottom row depicts T47D cells after 24 hours of nZnO treatment. The cellular morphology is drastically changed, many blebs are noted, and essentially all NPs that are detectable appear to have been internalized.**

Despite the number of studies that investigate nZnO, many questions remain regarding toxicity mechanisms and their inherent selectivity towards cancer cell destruction. Some of the more commonly cited mechanisms of nZnO toxicity has been

attributed to ROS generation, particle dissolution, and to a lesser extent, membrane damage.[1, 45-48] Since there is still controversy on the primary source of toxicity, the unmodified fluorescent nZnO described here may help elucidate the various toxicity mechanism(s) and give insight into why reports demonstrate cell type selective toxicity. After 24 hours post treatment, a nZnO fluorescence signal was still detectable in the interior of the cells and may suggest NP internalization is key to asserting the NPs toxic effects. Even though these interesting observations were made, the source(s) of the changes in cellular morphology were not deciphered and is the goal of future projects. Utilization of zinc ion specific dyes may allow for simultaneous tracking of both nZnO and the release of zinc ions from nZnO dissolution to help elucidate the complex nature of these interactions. Other specific labels, such as fluorophores specific to various endocytic processes and ROS sensitive dyes, would be keys to understanding the interactions of the nZnO with cells, but is beyond the scope of this paper. Other future work will look into reducing the size of the aggregates, stabilizing the particles in solution and conjugating antibodies to the surface of the NPs to facilitate their use as a potential bio-label for targeting specific cellular compartments.

## Conclusion

Achieving systematic control of native defects in ZnO NPs can often be challenging, especially in wet chemical methods. This work demonstrates the ability to control specific defect states of nZnO through modifications to the synthesis that modulate key properties of the material. The reduction of the band gap to ~3.1 eV and the shift of the emission spectra to the visible region allowed for imaging of the NPs using traditional fluorescence microscopy techniques. The ability to perform live cell imaging

with essentially pure nZnO may help in deciphering their complex interactions with various cells types and understanding their cancer cell selective toxicity. The relatively low toxicity of nZnO compared to other quantum dots such as cadmium chalcogenides may also make them more suitable as a bio-label in fluorescence imaging. Additionally, the alterations to the physical properties discussed in this report may also be exploited in other applications such as optoelectronic devices. Further research is needed to fully investigate their utilization in these various fields but, based on these studies, there is promise for them to be used in a variety of applications.

## Experimental Section

### ZnO Nanoparticle Synthesis

The new synthesis procedure for producing nZnO was adapted from previous procedures with various modifications.[41] Zinc acetate dihydrate was used as the zinc source and diethylene glycol (DEG) as the solvent. Three parameters were varied to control the defects in the wet chemical synthesis; the amount of polyvinylpyrrolidine (PVP), water, and annealing temperature. The solution was created first by the simultaneous addition of PVP (molecular weight 58k) and zinc acetate, followed by the addition of DEG and initially heated to 80˚ C. Various amounts of water were then added, the temperature brought up to 150˚ C, and then held for 75 minutes. Once the solution cooled to room temperature, the samples were centrifuged at 41,410 X g to remove the DEG and subsequently washed with absolute ethanol. The pellet was dried overnight at 60˚ C and then annealed in air at the various temperatures indicated.

Characterization

The nZnO samples were characterized using several techniques. X-ray diffraction (XRD) spectra were collected using a Rigaku Miniflex 600 X-ray diffractometer and used to determine the crystal phase, lattice parameters and to estimate the average crystal size using Rigaku PDXL software version 1.8.0.3. Thermal gravimetric analysis (TGA) was performed using a Netzsch STA449F1 TGA-DSC to define the ideal temperature and time to remove retained chemical species from the synthesis procedure. Transmission electron microscopy (TEM) was utilized to obtain both average crystal size distributions and determine the NP morphology using a JEOL JEM-2100 HR analytical transmission electron microscope. To obtain atomic concentrations and evaluate sample purity, both X-ray photoelectron spectroscopy (XPS) and Fourier transform infrared spectroscopy (FTIR) were utilized. A Physical Electronics Versaprobe system with a monochromated Al $K_{\alpha}$ X-ray source was used to obtain the XPS spectra and a Bruker Tensor 27 spectrometer was used for FTIR spectra collection. FTIR pellets were prepared by grinding 1.5 mg of the NP sample with 0.200 g of spectroscopic grade KBr and subsequently pressed for 4 minutes with 8 tons of pressure. A Malvern Zetasizer NanoZS was used to collect dynamic light scattering (DLS) measurements by using a concentration of ZnO NPs of 0.5 mg/mL in nanopure water. For inductively coupled plasma mass spectrometry (ICP-MS) experiments, the nZnO were dissolved in 25 mL of highly pure 2% nitric acid solution and analyzed by a Thermo-electron X-series II quadrupole ICP-MS. The samples were analyzed for various metal contaminations such as iron, cobalt and nickel against the total zinc content. Raman and photoluminescence (PL) spectra were measured in backscattering geometry using a Jobin Yvon T64000

0.64m triple spectrometer equipped with a liquid nitrogen cooled multichannel CCD detector. Spectra were recorded at 10 K using a variable temperature closed cycle helium cryostat. Ultraviolet light (325 nm line of He-Cd laser) was used for excitation.

ZnO Nanoparticle and Live Cell Imaging

Confocal microscopy was utilized to image both the nZnO and T47D cells treated with nZnO. Because this new method of nZnO synthesis achieves a lower band gap of ~3.1 eV, a 405 nm laser was able to be used as an excitation source and nZnO fluorescence monitored. For live cell imaging experiments, T47D (ATCC HTB-133), a cell line derived from ductal breast carcinoma (ATCC; Manassas, VA) was maintained in log phase and cultured in RPMI 1640 media following ATCC recommendations. Prior to imaging experiments, the cells were washed and resuspended in a custom made RPMI 1640 media free of HEPES, phenol red and phosphate (PPH free RPMI 1640; Thermo Fisher Scientific; Grand Island, NY) to prevent increased NP dissolution, remove fluorescent background signal and reduce the chemical transformation of the NPs, respectively.[10, 49] The cells were then transferred to Nunc Lab-Tek II Chambered cell culture slides (ThermoFisher; Waltham, MA). Following an overnight incubation to ensure cell adhesion, nZnO were added at a final concentration of 30 μg/mL and further incubated to allow for nZnO-cell interactions. Control (nZnO-free) cells were cultured in the same manner to assess auto-fluorescence generated using the 405 nm laser to excite the nZnO. Prior to imaging, live cells were stained with the plasma membrane stain Cell Mask Orange (Invitrogen; Carlsbad, CA). In brief, stain was added to culture media for at a final concentration of 5 μg/ml. All confocal images were acquired with a Zeiss 510 LSM system with the Zeiss Axiovert Observer Z1 inverted microscope and ZEN 2009

Imaging software (Carl Zeiss, Inc.; Thornwood, NY) utilizing Diode (405 nm) and HeNe (543) lasers as excitation sources; a Plan-Apochromat 20x/NA 0.8, Fluar 40x/NA 1.3 oil, or α-Plan Fluar 100x/NA 1.44 oil objective; and band-pass BP filters of 420-480 nm and 550-647 nm to image the nZnO particles and lipid layer, respectively.

**Supporting Information**

Supporting Information is available from the Wiley Online Library (upon acceptance) or from the author.

**Acknowledgements**

This research was supported in part by NSF-MRI awards (#032,233, #0722699, #0521315), and NIH (1R15CA141358-01). We also acknowledge support from the Biomolecular Research Center at Boise State University, COBRE, and INBRE with funding from the NIH Grant Nos. P20GM103408 and P20GM109095, NSF (Nos. 0619793, 0923535), the Idaho State Board of Education and the M. J. Murdock Charitable Trust- Instrumentation and Partners in Science programs. The content is solely the responsibility of the authors and does not necessarily represent the official views of the National Institutes of Health.

**Supporting Information**

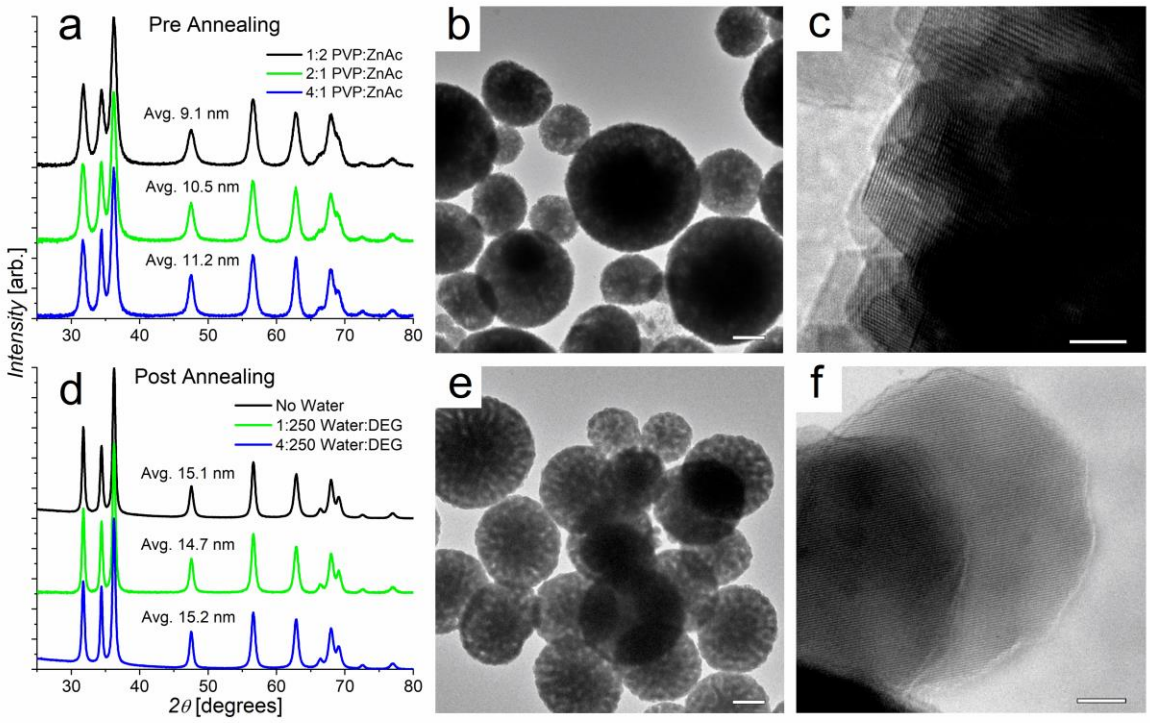


**Figure S4.1 (a) XRD patterns of as prepared nZnO produced with various amounts of PVP to zinc acetate (ZnAc). (b-c) TEM images of the as prepared nZnO produced with the 2:1 PVP to ZnAc ratio. (b) Aggregates are formed from the smaller (c) individual nZnO crystals. (d) XRD patters of nZnO synthesized with a 2:1 PVP:ZnAc ratio and various amounts of water added. This demonstrates that the amount of water added in this synthesis procedure does not affect the size of the crystals. (e-f) TEM images of the nZnO produced with the 1:250 water:DEG ratio show the size of the aggregates and verifying the average crystal sizes obtained from XRD. Scale bars = (b) 200 nm, (c) 5 nm, (e) 200 nm, and (f) 5 nm.**

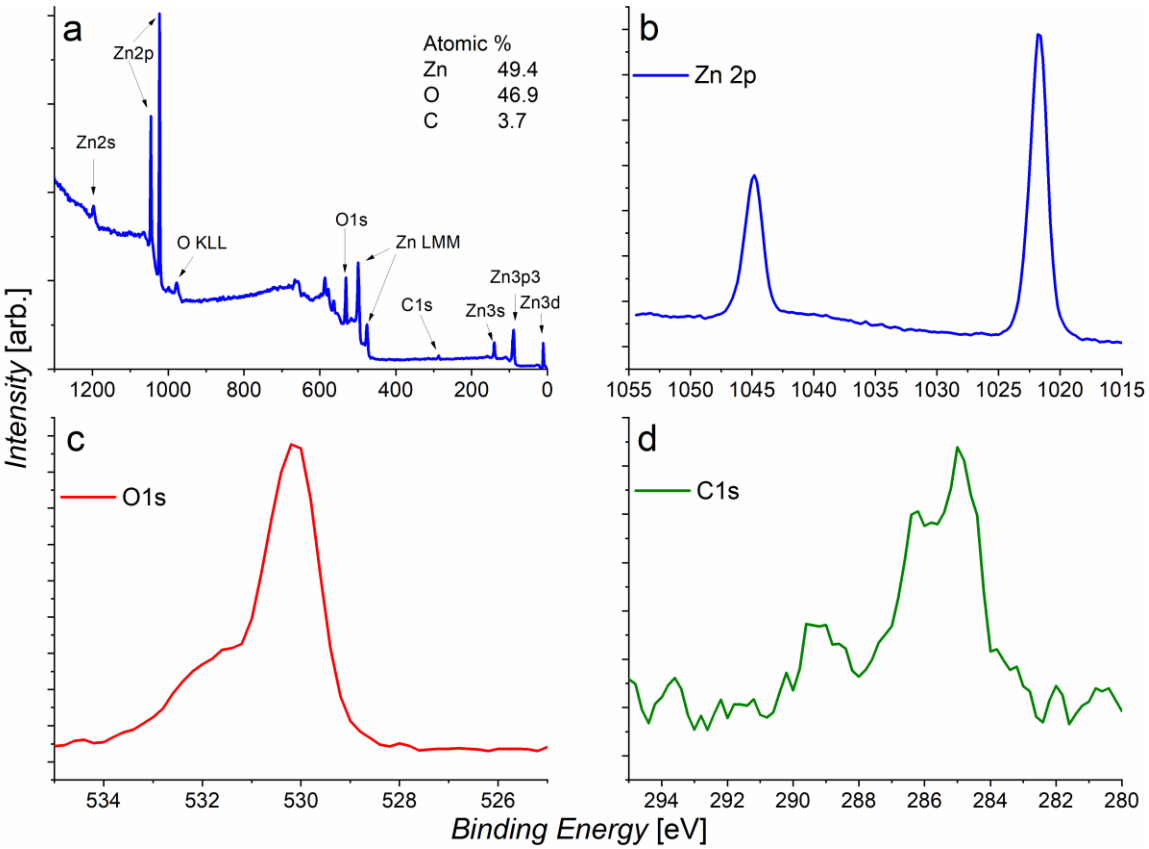


**Figure S4.2 (a-d) XPS scans of nZnO produced with a 2:1 PVP:ZnAc and annealed at 450º C for 10 minutes. (a) Survey scan of the nanoparticles demonstrates only the elements Zinc, Oxygen and Carbon were detected. (b-d) Core level scans of the Zn2P, O1s and C1s regions. The core level scans demonstrate a high purity of nZnO produced with the only contamination stemming from adventitious carbon due to atmospheric exposure.**

| ICP-MS | Chromium | Manganese | Iron | Cobalt | Nickel | Zinc |
|---|---|---|---|---|---|---|
| ppb | 0.027 | -0.009 | 0.24 | -0.006 | -0.022 | 2727 |
| ppb | 0.024 | -0.008 | 0.311 | -0.005 | -0.02 | 2719 |
| ppb | 0.019 | -0.008 | 0.057 | -0.006 | -0.022 | 2715 |
| Avg. | 0.023 | -0.009 | 0.203 | -0.006 | -0.021 | 2720 |
| Std. Dev. | 0.004 | 0.001 | 0.131 | 0 | 0.001 | 5.813 |

**Table S4.1 Table of ICP-MS measurements of various metals from the nZnO dissolved in high purity nitric acid. Not even 1 ppb of any other metal was found to be present in the nZnO demonstrating high purity of the nanoparticles.**

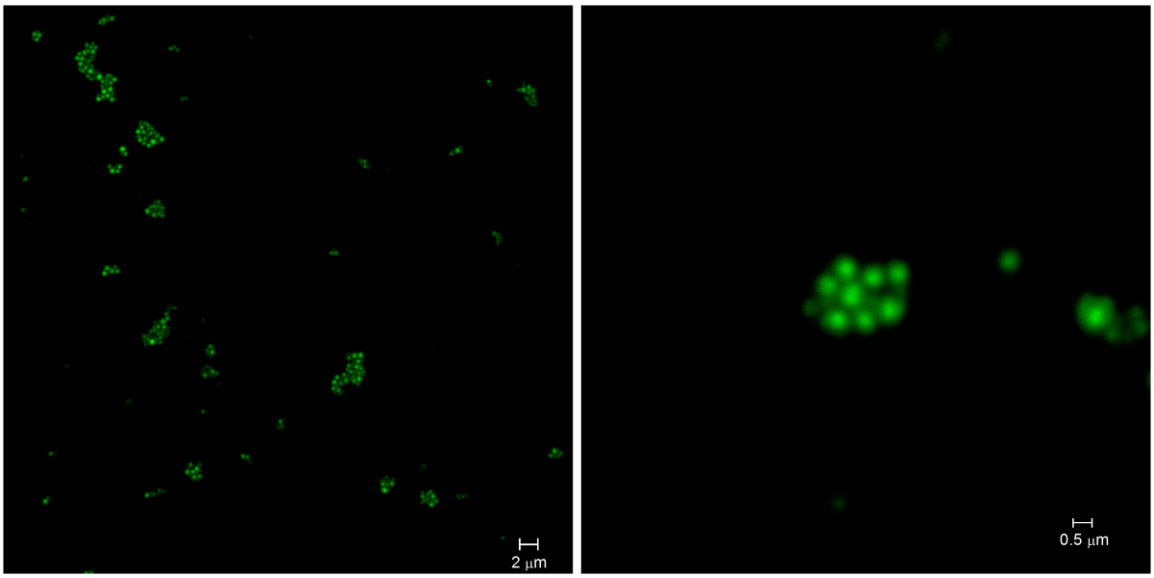


**Figure S4.3 Images of the nZnO acquired with a Zeiss LSM 880 with Airyscan using a 405 nm laser for excitation. Images acquired with higher magnification and resolution demonstrate the larger fluorescent agglomerates are comprised of the smaller nZnO aggregates (50-500 nm) as seen in the TEM images.**

## References

1. Rasmussen, J. W.; Martinez, E.; Louka, P.; Wingettt, D. G., Zinc oxide nanoparticles for selective destruction of tumor cells and potential for drug delivery applications. *Expert Opinion on Drug Delivery* **2010,** *7* (9), 1063-1077.

2. Bora, T.; Sathe, P.; Laxman, K.; Dobretsov, S.; Dutta, J., Defect engineered visible light active ZnO nanorods for photocatalytic treatment of water. *Catalysis Today* **2017,** *284*, 11-18.

3. Djurisic, A. B.; Ng, A. M. C.; Chen, X. Y., ZnO nanostructures for optoelectronics: Material properties and device applications. *Progress in Quantum Electronics* **2010,** *34* (4), 191-259.

4. Hanley, C.; Layne, J.; Punnoose, A.; Reddy, K. M.; Coombs, I.; Coombs, A.; Feris, K.; Wingett, D., Preferential killing of cancer cells and activated human T cells using ZnO nanoparticles. *Nanotechnology* **2008,** *19* (29), 10.

5. Resch-Genger, U.; Grabolle, M.; Cavaliere-Jaricot, S.; Nitschke, R.; Nann, T., Quantum dots versus organic dyes as fluorescent labels. *Nature Methods* **2008,** *5* (9), 763-775.

6. Chan, W. C. W.; Maxwell, D. J.; Gao, X. H.; Bailey, R. E.; Han, M. Y.; Nie, S. M., Luminescent quantum dots for multiplexed biological detection and imaging. *Current Opinion in Biotechnology* **2002,** *13* (1), 40-46.

7. Chen, N.; He, Y.; Su, Y. Y.; Li, X. M.; Huang, Q.; Wang, H. F.; Zhang, X. Z.; Tai, R. Z.; Fan, C. H., The cytotoxicity of cadmium-based quantum dots. *Biomaterials* **2012,** *33* (5), 1238-1244.

8. Punnoose, A.; Dodge, K.; Rasmussen, J. W.; Chess, J.; Wingett, D.; Anders, C., Cytotoxicity of ZnO Nanoparticles Can Be Tailored by Modifying Their Surface Structure: A Green Chemistry Approach for Safer Nanomaterials. *Acs Sustainable Chemistry & Engineering* **2014,** *2* (7), 1666-1673.

9. Xia, T.; Kovochich, M.; Liong, M.; Madler, L.; Gilbert, B.; Shi, H. B.; Yeh, J. I.; Zink, J. I.; Nel, A. E., Comparison of the Mechanism of Toxicity of Zinc Oxide and

Cerium Oxide Nanoparticles Based on Dissolution and Oxidative Stress Properties. *Acs Nano* **2008,** *2* (10), 2121-2134.

10. Lv, J. T.; Zhang, S. Z.; Luo, L.; Han, W.; Zhang, J.; Yang, K.; Christie, P., Dissolution and Microstructural Transformation of ZnO Nanoparticles under the Influence of Phosphate. *Environmental Science & Technology* **2012,** *46* (13), 7215-7221.

11. Herrmann, R.; Garcia-Garcia, F. J.; Reller, A., Rapid degradation of zinc oxide nanoparticles by phosphate ions. *Beilstein Journal of Nanotechnology* **2014,** *5*, 2007-2015.

12. Mu, Q. S.; David, C. A.; Galceran, J.; Rey-Castro, C.; Krzeminski, L.; Wallace, R.; Bamiduro, F.; Milne, S. J.; Hondow, N. S.; Brydson, R.; Vizcay-Barrena, G.; Routledge, M. N.; Jeuken, L. J. C.; Brown, A. P., Systematic Investigation of the Physicochemical Factors That Contribute to the Toxicity of ZnO Nanoparticles. *Chemical Research in Toxicology* **2014,** *27* (4), 558-567.

13. Xiong, H. M., Photoluminescent ZnO nanoparticles modified by polymers. *Journal of Materials Chemistry* **2010,** *20* (21), 4251-4262.

14. Wang, H.; Wingett, D.; Engelhard, M. H.; Feris, K.; Reddy, K. M.; Turner, P.; Layne, J.; Hanley, C.; Bell, J.; Tenne, D.; Wang, C.; Punnoose, A., Fluorescent dye encapsulated ZnO particles with cell-specific toxicity for potential use in biomedical applications. *Journal of Materials Science-Materials in Medicine* **2009,** *20* (1), 11-22.

15. Liu, Y. L.; Ai, K. L.; Yuan, Q. H.; Lu, L. H., Fluorescence-enhanced gadolinium-doped zinc oxide quantum dots for magnetic resonance and fluorescence imaging. *Biomaterials* **2011,** *32* (4), 1185-1192.

16. Rotella, H.; Mazel, Y.; Brochen, S.; Valla, A.; Pautrat, A.; Licitra, C.; Rochat, N.; Sabbione, C.; Rodriguez, G.; Nolot, E., Role of vacancy defects in Al doped ZnO thin films for optoelectronic devices. *Journal of Physics D-Applied Physics* **2017,** *50* (48), 7.

17. Ahmad, M.; Zhao, J.; Iqbal, J.; Miao, W.; Xie, L.; Mo, R.; Zhu, J., Conductivity enhancement by slight indium doping in ZnO nanowires for optoelectronic applications. *Journal of Physics D-Applied Physics* **2009,** *42* (16), 7.

18. Gu, F. B.; You, D.; Wang, Z. H.; Han, D. M.; Guo, G. S., Improvement of gas-sensing property by defect engineering in microwave-assisted synthesized 3D ZnO nanostructures. *Sensors and Actuators B-Chemical* **2014,** *204,* 342-350.

19. Weber, M. H.; Selim, F. A.; Solodovnikov, D.; Lynn, K. G., Defect engineering of ZnO. *Applied Surface Science* **2008,** *255* (1), 68-70.

20. Shi, W. S.; Agyeman, O.; Xu, C. N., Enhancement of the light emissions from zinc oxide films by controlling the post-treatment ambient. *Journal of Applied Physics* **2002,** *91* (9), 5640-5644.

21. Das, D.; Mondal, P., Photoluminescence phenomena prevailing in c-axis oriented intrinsic ZnO thin films prepared by RF magnetron sputtering. *Rsc Advances* **2014,** *4* (67), 35735-35743.

22. Janotti, A.; Van de Walle, C. G., Native point defects in ZnO. *Physical Review B* **2007,** *76* (16), 22.

23. McCluskey, M. D.; Jokela, S. J., Defects in ZnO. *Journal of Applied Physics* **2009,** *106* (7), 13.

24. Alkauskas, A.; Pasquarello, A., Band-edge problem in the theoretical determination of defect energy levels: The O vacancy in ZnO as a benchmark case. *Physical Review B* **2011,** *84* (12), 11.

25. Koczkur, K. M.; Mourdikoudis, S.; Polavarapu, L.; Skrabalak, S. E., Polyvinylpyrrolidone (PVP) in nanoparticle synthesis. *Dalton Transactions* **2015,** *44* (41), 17883-17905.

26. Scott, J. F., UV RESONANT RAMAN SCATTERING IN ZNO. *Physical Review B* **1970,** *2* (4), 1209-&.

27. Cheng, H. M.; Lin, K. F.; Hsu, H. C.; Hsieh, W. F., Size dependence of photoluminescence and resonant Raman scattering from ZnO quantum dots. *Applied Physics Letters* **2006,** *88* (26), 3.

28. Kumar, B.; Gong, H.; Chow, S. Y.; Tripathy, S.; Hua, Y., Photoluminescence and multiphonon resonant Raman scattering in low-temperature grown ZnO nanostructures. *Applied Physics Letters* **2006,** *89* (7), 3.

29. Samuel, M. S.; Koshy, J.; Chandran, A.; George, K. C., Optical phonon confinement in ZnO nanorods and nanotubes. *Indian Journal of Pure & Applied Physics* **2010,** *48* (10), 703-708.

30. Rajalakshmi, M.; Arora, A. K.; Bendre, B. S.; Mahamuni, S., Optical phonon confinement in zinc oxide nanoparticles. *Journal of Applied Physics* **2000,** *87* (5), 2445-2448.

31. Lin, K. F.; Cheng, H. M.; Hsu, H. C.; Hsieh, W. F., Band gap engineering and spatial confinement of optical phonon in ZnO quantum dots. *Applied Physics Letters* **2006,** *88* (26), 3.

32. Ahn, C. H.; Kim, Y. Y.; Kim, D. C.; Mohanta, S. K.; Cho, H. K., A comparative analysis of deep level emission in ZnO layers deposited by various methods. *Journal of Applied Physics* **2009,** *105* (1), 5.

33. Richter, H.; Wang, Z. P.; Ley, L., THE ONE PHONON RAMAN-SPECTRUM IN MICROCRYSTALLINE SILICON. *Solid State Communications* **1981,** *39* (5), 625-629.

34. Jeong, S. H.; Kim, B. S.; Lee, B. T., Photoluminescence dependence of ZnO films grown on Si(100) by radio-frequency magnetron sputtering on the growth ambient. *Applied Physics Letters* **2003,** *82* (16), 2625-2627.

35. Cao, B. Q.; Cai, W. P.; Zeng, H. B., Temperature-dependent shifts of three emission bands for ZnO nanoneedle arrays. *Applied Physics Letters* **2006,** *88* (16), 3.

36. Vempati, S.; Mitra, J.; Dawson, P., One-step synthesis of ZnO nanosheets: a blue-white fluorophore. *Nanoscale Research Letters* **2012,** *7*, 10.

37. Tam, K. H.; Cheung, C. K.; Leung, Y. H.; Djurisic, A. B.; Ling, C. C.; Beling, C. D.; Fung, S.; Kwok, W. M.; Chan, W. K.; Phillips, D. L.; Ding, L.; Ge, W. K., Defects in ZnO nanorods prepared by a hydrothermal method. *Journal of Physical Chemistry B* **2006,** *110* (42), 20865-20871.

38. Vanheusden, K.; Seager, C. H.; Warren, W. L.; Tallant, D. R.; Voigt, J. A., Correlation between photoluminescence and oxygen vacancies in ZnO phosphors. *Applied Physics Letters* **1996,** *68* (3), 403-405.

39. Rodnyi, P. A.; Khodyuk, I. V., Optical and luminescence properties of zinc oxide (Review). *Optics and Spectroscopy* **2011,** *111* (5), 776-785.

40. Vanheusden, K.; Warren, W. L.; Seager, C. H.; Tallant, D. R.; Voigt, J. A.; Gnade, B. E., Mechanisms behind green photoluminescence in ZnO phosphor powders. *Journal of Applied Physics* **1996,** *79* (10), 7983-7990.

41. Hanley, C.; Thurber, A.; Hanna, C.; Punnoose, A.; Zhang, J. H.; Wingett, D. G., The Influences of Cell Type and ZnO Nanoparticle Size on Immune Cell Cytotoxicity and Cytokine Induction. *Nanoscale Research Letters* **2009,** *4* (12), 1409-1420.

42. Lim, K.; Hamid, M. A. A.; Shamsudin, R.; Al-Hardan, N. H.; Mansor, I.; Chiu, W., Temperature-Driven Structural and Morphological Evolution of Zinc Oxide Nano-Coalesced Microstructures and Its Defect-Related Photoluminescence Properties. *Materials* **2016,** *9* (4), 15.

43. Rathnayake, S.; Unrine, J. M.; Judy, J.; Miller, A. F.; Rao, W.; Bertsch, P. M., Multitechnique Investigation of the pH Dependence of Phosphate Induced Transformations of ZnO Nanoparticles. *Environmental Science & Technology* **2014,** *48* (9), 4757-4764.

44. Reed, R. B.; Ladner, D. A.; Higgins, C. P.; Westerhoff, P.; Ranville, J. F., Solubility of nano-zinc oxide in environmentally and biologically important matrices. *Environmental Toxicology and Chemistry* **2012,** *31* (1), 93-99.

45. Kao, Y. Y.; Chen, Y. C.; Cheng, T. J.; Chiung, Y. M.; Liu, P. S., Zinc Oxide Nanoparticles Interfere With Zinc Ion Homeostasis to Cause Cytotoxicity. *Toxicological Sciences* **2012,** *125* (2), 462-472.

46. Buerki-Thurnherr, T.; Xiao, L. S.; Diener, L.; Arslan, O.; Hirsch, C.; Maeder-Althaus, X.; Grieder, K.; Wampfler, B.; Mathur, S.; Wick, P.; Krug, H. F., In vitro mechanistic study towards a better understanding of ZnO nanoparticle toxicity. *Nanotoxicology* **2013,** *7* (4), 402-416.

47. Xie, Y. P.; He, Y. P.; Irwin, P. L.; Jin, T.; Shi, X. M., Antibacterial Activity and Mechanism of Action of Zinc Oxide Nanoparticles against Campylobacter jejuni. *Applied and Environmental Microbiology* **2011,** *77* (7), 2325-2331.

48. Anders, C. B.; Eixenberger, J. E.; Franco, N. A.; Hermann, R. J.; Rainey, K. D.; Chess, J. J.; Punnoose, A.; Wingett, D. G., ZnO nanoparticle preparation route influences surface reactivity, dissolution and cytotoxicity. *Environmental Science-Nano* **2018,** *5* (2), 572-588.

49. Eixenberger, J. E.; Anders, C. B.; Hermann, R. J.; Brown, R. J.; Reddy, K. M.; Punnoose, A.; Wingett, D. G., Rapid Dissolution of ZnO Nanoparticles Induced by Biological Buffers Significantly Impacts Cytotoxicity. *Chemical Research in Toxicology* **2017,** *30* (8), 1641-1651.

# CHAPTER FIVE: TRIGGERED RELEASE OF ENCAPSULATED ZNO NANOPARTICLES AND CHEMOTHERAPEUTICS FOR DRUG DELIVERY APPLICATIONS

*Josh E. Eixenberger†‡, Katelyn Wada‡, Catherine B. Anders¥, Kongara M. Reddy‡, Raquel J. Brown┴, Daniel Fologea‡† and Denise G. Wingett†£*

†Biomolecular Sciences Graduate Program, ‡Department of Physics, ┴Biomolecular Research Center, £Department of Biological Sciences, Boise State University, Boise, ID 83725, USA, ¥Idaho Veterans Research & Education Foundation – Boise VA Medical Center, 500 W Fort St, Boise, ID 83702, USA

**KEYWORDS**: ZnO Nanoparticles, Drug Delivery, Triggered Release, Cancer, therapeutic

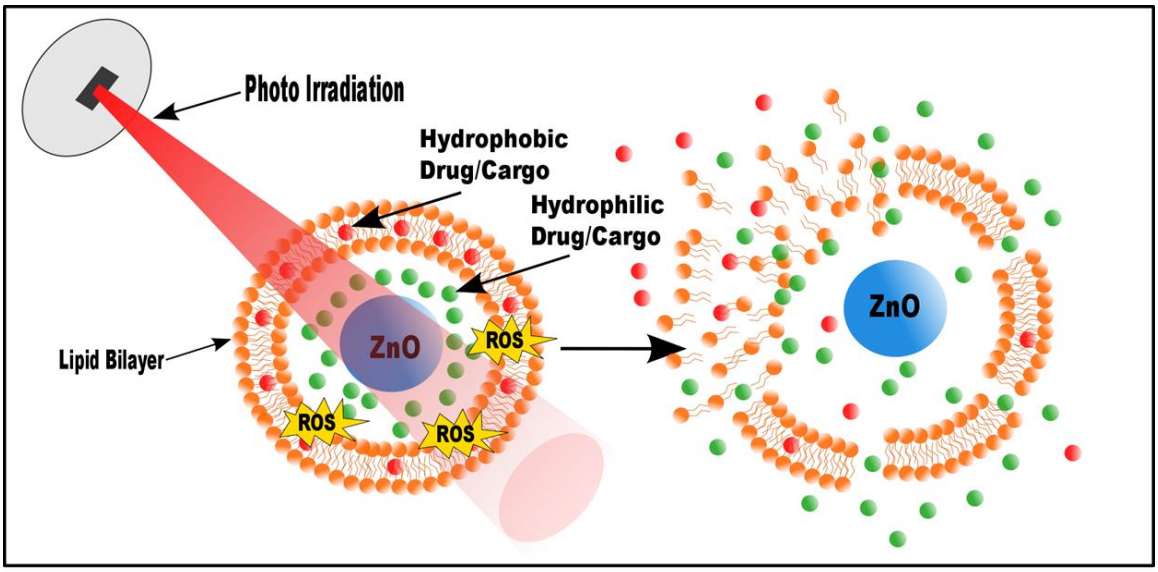



## Abstract

Nanomedicine offers high promise for the treatment of diseases and numerous novel approaches using nanomaterials have been developed over the years. In this report, we demonstrate a new strategy utilizing ZnO nanoparticles (nZnO) to trigger the rapid release of lipid encapsulated contents upon photo irradiation. In vitro studies demonstrate that encapsulation of nZnO effectively eliminates the toxicity of nZnO but is re-established upon the triggered release from the lipid coating. Using 5(6)-carboxyfluoroscein as a model for hydrophilic drugs, we show the ability to co-load drugs with nZnO into the liposome. Kinetics studies demonstrate the ability to release the majority of the dye within 60 minutes post photo irradiation. To further expand upon this, Jurkat T cell leukemia and T47D breast cancer cells were treated with co-encapsulated nZnO and the hydrophobic cancer drug Paclitaxel. These studies demonstrate increased toxicity of the triggered release groups with an extreme difference noted in the T47D breast cancer cell model. Taken together, these studies demonstrate that this system has

promise to potentially minimize systemic toxicity while allowing for the localized selective destruction of cancer.

## Introduction

The field of nanobiotechnology is rapidly growing and numerous applications have been developed utilizing nanomaterials. In particular, researchers have pursued the use of nanomedicine for the diagnosis and treatment of diseases such as cancer, and many novel nanostructures offer considerable promise in these areas. Currently, there are already over 50 FDA approved nanomedicines and numerous others in clinical trials.[1] The goal of many of these new technologies is to offer new therapeutic treatment options or to improve upon already existing technologies through increased efficacy or by minimizing off-target side effects. In this regard, ZnO nanoparticles (nZnO) have been utilized in various potential drug delivery devices,[2] and have many features that make it a good candidate for therapeutic applications.

One of the well-known physical properties and proposed toxicity mechanisms of nZnO is particle dissolution. This feature is enhanced in lower pH environments, such as in certain tumors or intracellular compartments, and has been exploited as a means to control drug escape. An example of utilizing the dissolution potential of ZnO is to encapsulate doxorubicin loaded $SiO_2$ NPs with a layer of ZnO.[3] The ZnO layer prevents premature drug leakage, but when exposed to a lower pH, the quick dissolution of ZnO induces the release of the drug.

In addition to high dissolution potential, nZnO and numerous other metal oxide NPs have another property that can be exploited for use as a potential therapeutic. Many metal oxide NPs show strong photocatalytic activity and reports have demonstrated the

generation of reactive oxygen species (ROS) from various photocatalytic semiconductors.[4, 5] ZnO nanoparticles, in particular, have been shown to have increased toxicity towards cancer cells when exposed to UV light.[6, 7] Phototherapy treatment experiments with nZnO have demonstrated increased ROS generation that can lead to extensive lipid peroxidation of cellular membranes.[8-10] Since the peroxidation of lipids can lead to lipid radicals that propagate throughout the bilayer, this process has been shown to lead to the rupture of cellular membranes.[11, 12] Collectively, the various physical properties of nZnO have led to the development of novel strategies to combat diseases and highlight why numerous researchers are pursuing its use as a therapeutic.

In addition to these physical properties, nZnO show inherent selective toxicity towards various cancer types when compared with the normal non-malignant cell types of identical lineage.[12-14] Reports have shown up to a 33-fold selectivity towards cancerous cells, which is a higher therapeutic index than reported for many traditionally used chemotherapeutics using similar assays.[15] Importantly, the selective nature of nZnO for cancers such as squamous cell lung cancer and pancreatic adenocarcinoma has recently been demonstrated in mouse models and is not just a novelty of *in vitro* experiments.[16, 17] Additional reports have used nZnO structures for both MRI and bio-imaging purposes, thereby suggesting that nZnO have the potential to be used in both therapeutic and diagnostic applications as well.[17-19]

Even though there have been numerous strategies that utilize nZnO for therapeutic applications, there do exist some limitations to its use. With the high dissolution potential of nZnO, introduction into biological fluids can induce the dissolution of the particles before they reach their target site. Additionally, nZnO is prone

to aggregation, especially in environments with high ionic concentrations such as in biological fluids. This may also impede their effectiveness as a therapeutic and thus many reports have looked at ways to achieve stable nZnO suspensions. A common strategy to stabilize nZnO in solution is to coat the particles with polymers or biomolecules. Lipids vesicles are already extensively used for drug delivery and may help increase the stability of nZnO while simultaneously preventing premature dissolution.

Hybrid liposome-inorganic NPs offer an interesting avenue for drug delivery and due to many of the key attributes of lipids, liposomal formulations make up a large fraction of the currently FDA approved nanomedicines. Some of the attributes that make lipids attractive for drug delivery include high biocompatibility, ease of synthesis, various means of controlling drug release, and targeting by both active and passive processes.[1, 20, 21] Since lipids are amphipathic, both hydrophobic and hydrophilic drugs can be loaded within liposomes. This feature has allowed for their use in both approved nanomedicines and ongoing clinical trials for both hydrophobic and hydrophilic drugs.[1, 20, 21] Many formulations of liposomes have demonstrated high encapsulation efficiency of both hydrophobic and hydrophilic drugs which can improve their stability and pharmacokinetics. However, unmodified liposomes themselves are recognized by the immune system and are quickly cleared from circulation.[22] This drawback has been overcome by the creation of "stealth" liposomes. For example, the conjugation of polyethylene glycol (PEG) to the head group of lipids prevents the reticuloendothelial system from rapidly clearing the stealth liposomes and leads to improved circulation time.[1, 22, 23]

In addition to the conjugation of PEG to lipids, conjugating ligands or antibodies to liposomes specific for individual cell surface receptors allows for active targeting and can improve their localization in tissues that over express these surface features. Additionally, passive targeting has been another avenue that researchers have pursued. Nanoparticles (NPs) in the size range of 4-200 nm have been shown to accumulate in tumor environments that have a "leaky" vasculature and avoid clearance due to reduced lymphatic drainage. This feature is termed the enhanced permeability and retention (EPR) effect and is present in certain tumor morphologies.[24, 25] Targeting capabilities offer the promise of improved efficacy by high concentrations of the drug being released in the target area. This can simultaneously reduce the amount of overall drug concentration needed in hopes of reducing or eliminating unwanted side effects.

The controlled release of liposomal contents has been demonstrated through various mechanisms. For example, pH sensitive lipids such as dioleoylphosphatidylethanolamine (DOPE) allow for increased membrane permeability when incorporated into the bilayer and subsequently exposed to a lower pH environment.[26, 27] As many tumor microenvironments have a relatively acidic pH, this approach has been pursued as a means to release high payloads of drugs in a localized area.

With all of the different nanotechnologies that are currently under development, the promise of improved drug delivery and diagnostic options may allow for increased patient survival while minimizing side effects commonly associated with current chemotherapeutics. Since nZnO have numerous promising attributes and lipid carriers are proven efficient drug carriers, we sought to combine the benefits of both systems. Here

we report on the first foray, to our knowledge, in utilizing the ROS generating capabilities of nZnO to trigger the rapid release of cargo contained within a lipid carrier as a potential new drug delivery strategy.

## Materials and Methods

### ZnO Nanoparticle Synthesis and Characterization

All ZnO NPs in this study were produced by a forced hydrolysis method that has been previously reported (see Chapter 4). Zinc acetate dihydrate and polyvinylpyrrolidine (PVP) were added to diethylene glycol and brought to 80˚ C. Then nanopure water was added, the solution heated to 150˚ C, and held for 75 minutes. After cooling to room temperature, the mixture was centrifuged at 41,140 x g and repeatedly washed with absolute ethanol. The pellet was dried overnight at 60˚ C and pulverized with a mortar and pestle. The powder was subsequently annealed at 500˚ C for 10 minutes.

NPs were characterized by a variety of techniques including: X-ray diffraction (XRD), Transmission Electron Microscopy (TEM), Fourier Transform Infrared Spectroscopy (FTIR), X-ray Photoelectron Spectroscopy (XPS), Inductively Coupled Plasma Mass Spectrometry (ICP-MS), and Energy Dispersive X-ray Spectroscopy (EDX). A Rigaku Miniflex 600 X-ray diffractometer was used for XRD measurements to verify the crystal phase and estimate the crystal size of the NPs. A JEOL JEM-2100 HR analytical transmission electron microscope was used to acquire TEM images of the nZnO to verify the crystal size and obtain the NP morphology. To evaluate the sample purity, a Physical Electronics Versaprobe XPS system and a Bruker Tensor 27 spectrometer FTIR system were utilized. For FTIR experiments, the pellet method was used where 1.5 mg of the nZnO sample was ground with 0.200 g of spectroscopic grade

KBr and subsequently pressed with 8 tons of pressure for 4 minutes. For dynamic light scattering and zeta potential measurements, a Malvern Zetasizer NanoZS was utilized by suspending 0.25 mg/mL of the nZnO in nanopure water and in 130 mM NaCl. For gadolinium doped nZnO, the same synthesis procedure was used except that PVP was excluded and gadolinium acetate was added at the appropriate molar ratio with the zinc acetate dihydrate. To further evaluate the nZnO purity and to evaluate the doping concentration of gadolinium in the appropriate samples, ICP-MS was utilized. Additionally, XRD and electron diffraction patterns were collected using the same instruments to verify crystal phase purity of the gadolinium doped samples and EDX measurements were obtained to further verify the gadolinium content.

Encapsulation of nZnO and Cargo

ZnO NPs were encapsulated in soy phosphatidylcholine (Avanti Polar Lipids Inc., Alabaster, AL) and cholesterol with a 3 to 1 (w/w) ratio. The lipids and cholesterol (chol) were dissolved in chloroform with a final concentration of 13.33 mg/mL (lipid + chol). The lipid/chol solution was then put under vacuum overnight to remove all solvent. To encapsulate the NPs, nZnO was suspended in 130 mM NaCl and sonicated for 45 minutes. Simultaneously, 130 mM NaCl was added to the lipid cake for hydration and heated in a water bath to 60$^{o}$ C. Upon reaching 60$^{o}$ C, the lipids were briefly sonicated and then the nZnO solution was added for a final nZnO concentration of 4.07 mg/mL (50 mM) with various nZnO to lipid ratios. The NP/lipid/chol solution was then sonicated in a bath sonicator for 1 hour at 60$^{o}$ C and stored at 4$^{o}$ C until use. To encapsulate the fluorescent dye 5(6)-carboxyfluoroscein (CF) with the nZnO, the same procedure was carried out except the solution was comprised of 30 mM CF and 100 mM NaCl to

prevent osmotic pressure artifacts when resuspending the lipid coated particles in 130 mM NaCl. The CF/NaCl solution was pH adjusted to 7.4 and 9.85 by adding the appropriate amounts of NaOH. For paclitaxel (PTX) loading, a 2 mM stock solution was first prepared by dissolving PTX (Alfa Aesar, Haverhill, MA) in DMSO. To co-encapsulate PTX with the nZnO, an appropriate amount of the PTX stock solution was added to the lipid/chol mixture while in the chloroform solution and then all subsequent procedures were carried out as described above.

Simulated Drug Release

The fluorescent dye, CF, was utilized as a model for hydrophilic drug release and was co-loaded with nZnO as described above. The dye was loaded at 30 mM, well above the self-quenching concentration through the passive loading process. To remove the CF from the exterior solution, the encapsulated nZnO/CF was centrifuged at 296 xg for 2 minutes and the solution was exchanged with 130 mM NaCl repeatedly until the solution was clear. Fluorescent measurements were performed using a FluoroMax-4 spectrofluorometer with a working range of 285-750 nm. An excitation of 480 nm was used and emission spectra were collected from 490-600 nm. A self-quenching curve of CF was generated by collecting fluorescent measurements with a various concentration of free CF in 130 mM NaCl to verify that the working concentrations were within the linear fluorescent region (Figure S5.1). Baseline measurements were first collected ($F_{baseline}$) and then a 30 W, 365 nm LED lamp was used as a UV source to cause photoexcitation of nZnO and induce the triggered release of the fluorescent dye (F). To induce full release of the encapsulated dye ($F_{total}$), 20 uL of 5% Triton-X stock was then added to the solution. The percentage of released CF was determined by:

$$\%\, released = (F - F_{baseline}) / (F_{total} - F_{baseline})\ x\ 100$$

Cell Culture

To assess the effect that the triggered release of encapsulated nZnO (Enc-nZnO) and encapsulated nZnO with PTX (Enc-nZnO/PTX) had on the cytotoxicity of cancer cells, two human cell lines were utilized; Jurkat (ATCC TIB-152), a suspension cell line derived from acute T cell leukemia and T47D (ATCC HTB-133), an adherent cell line derived from ductal breast carcinoma (ATCC; Manassas, VA). Both cell lines were cultured in log phase using RPMI 1640 media supplemented with 10% FBS (fetal bovine serum), 1% penicillin/streptomycin, 2 mM L-glutamine, and for T47D cells, 0.2 Units/mL of bovine insulin per ATCC (American Type Culture Collection) recommendations.

ZnO NP and Live Cell Imaging

To evaluate the encapsulation of nZnO within a lipid membrane, imaging experiments were performed. The Enc-nZnO sample was transferred into a Nunc Lab-Tek II Chambered Coverglass 2 that contained 130 mM NaCl. The lipids were then stained utilizing the plasma membrane stain Cell Mask Orange (Invitrogen; Carlsbad, CA) at a final concentration of 5 μg/mL, 30 minutes prior to imaging. For live cell imaging of T47D breast cancer cells, the cells were transferred to a Nunc Lab Tek II chamber in RPMI 1640 two days prior to imaging at a concentration of 100,000 cells/well and allowed to attach to the cover slip. After 24 hours, the media was gently aspirated and then replaced with HEPES-free, phenol-free, and phosphate-free RPMI 1640 (PPH free RPMI 1640) (custom order Thermo Fisher Scientific; Grand Island, NY). The media exchange was carried out to prevent the transformation and dissolution of

nZnO induced by phosphate and HEPES, respectively.[28-30] Phenol red was excluded to prevent fluorescence emissions during the imaging experiments. The cells were treated with Enc-nZnO 24 hour before imaging at a final concentration of 81.4 μg/mL (1 mM) for the non-triggered released experiments. In the triggered release group, the T47D cells were treated with a final nZnO concentration of 20.3 μg/mL (250 μM). Cell Mask Orange was added to the media and cultures incubated an additional 30 minutes prior to imaging.

Confocal microscopy was used to image both the Enc-nZnO and T47D cells treated with Enc-nZnO. Images were acquired using a Zeiss 510 LSM system with the Zeiss Axiovert Observer Z1 inverted microscope and ZEN 2009 Imaging software (Carl Zeiss, Inc., Thornwood, NY) utilizing different objectives and band-pass filters. We recently reported on a new synthesis procedure to produce essentially pure nZnO that lowers the band gap to ~3.1 eV allowing for the 405 nm laser to be used as an excitation source to produce a narrow fluorescence emission band from nZnO (410-430 nm; see Chapter 4). Using a configuration specific for the excitation and emission of the synthesized nZnO and the plasma membrane stain, images were collected with either a Plan-Apochromat 20x/NA 0.8 or Plan-Apochromat oil 63x/NA 1.4 objective. The diode (405 nm) and HeNe (543 nm) lasers were used as excitation sources, and band-pass filters of 420-480 nm and 550-647 nm were used to image the nZnO and lipid layer, respectively.

Viability Studies

For viability assessments, both Jurkat and T47D cells were cultured following ATCC recommendations noted above. For the Jurkat T cell line, the cells were first washed with PPH free RPMI 1640 and then seeded at a concentration of $2.5 \times 10^5$

cells/mL using the same media in a 96 well plate. For T47D cells, the cells were first seeded in the culture media at 1.0 x $10^5$ cells/well in a 24 well plate the day prior to treatment to allow for cell attachment. The media was then gently aspirated and replaced with the PPH free RPMI 1640 media prior to NP treatment.

The Enc-nZnO and Enc-nZnO/PTX stocks were prepared, as indicated above, at a nZnO concentration of 4.07 mg/mL (50 mM) and pH=7.2 to avoid potential effects to cellular viability using a higher pH. For the free nZnO (non-encapsulated) controls, a fresh stock was prepared for each viability experiment by first suspending the nZnO in nanopure water at a concentration of 4.07 mg/mL (50 mM) and sonicated for 20 minutes. The 2 mM PTX-DMSO solution was used to assess free PTX effects on the cells as a control. Prior to treatment, PTX-DMSO solution was added to fresh cellular media at the desired PTX concentration making the final DMSO concentration ≤ 0.2 %. In the case of free nZnO, Enc-nZnO and Enc-nZnO/PTX, the appropriate amount of the stock solution was added to fresh cellular media to achieve a final nZnO concentration of 1.63 mg/mL (20 mM) prior to addition.

Once treated with NPs, the cells were then cultured for 48 hours at 37 $^oC$ and 5% $CO_2$. For samples receiving UV irradiation, cultures were subjected to photo-irradiation 1.5 hours post NP treatment using the same 30 W, 365 nm LED lamp as in the simulated drug release studies. After optimizing the UV irradiation protocol, we determined the required UV exposure to be 3 minutes for Jurkat cells and 2 minutes for T47D cells to re-establish the toxicity of the nZnO while minimizing effects to the cells viability. Cell viability was assessed using the Alamar Blue metabolic assay. Alamar blue was added to the wells at a final concentration of 10% 44 hours post treatment and incubated for an

additional 4 hours. The fluorescence intensity measurements were performed using a Biotek Synergy MX plate reader using an excitation/emission of 530/590 nm.

## Results

ZnO NP Synthesis and Characterization

ZnO nanoparticles (nZnO) were synthesized using a previously reported wet chemical method utilizing DEG as a solvent (see Chapter 4). This particular synthesis method was chosen as it produces nZnO with a narrow visible fluorescence band that allows for fluorescent imaging using traditional fluorescent microscopy techniques. XRD measurements verified the hexagonal wurzite crystal structure, with no other phases detected and an average crystal size of 15.1 ± X nm. TEM images (Figure 5.1), demonstrate that the nZnO form larger aggregates of 50-400 nm comprised of smaller nZnO crystals of ~15 nm, thereby confirming the XRD analysis. Dynamic light scattering measurements in nanopure water and 130 mM NaCl give the average hydrodynamic size (HDS) of the aggregated nZnO as 317 ± 2.87/2092±149.4 (Z-avg.; d.nm) with a polydispersity index (PDI) of 0.122/0.4, respectively (Figure S5.2 for size distributions). FTIR, XPS and ICP-MS measurements were used to confirm sample purity. With the exception of small amounts of carbon dioxide impurities and hydroxide formation, the nZnO are essentially pure (Figure S5.3). A more extensive characterization of this nZnO formulation has already been reported (see Chapter 4).

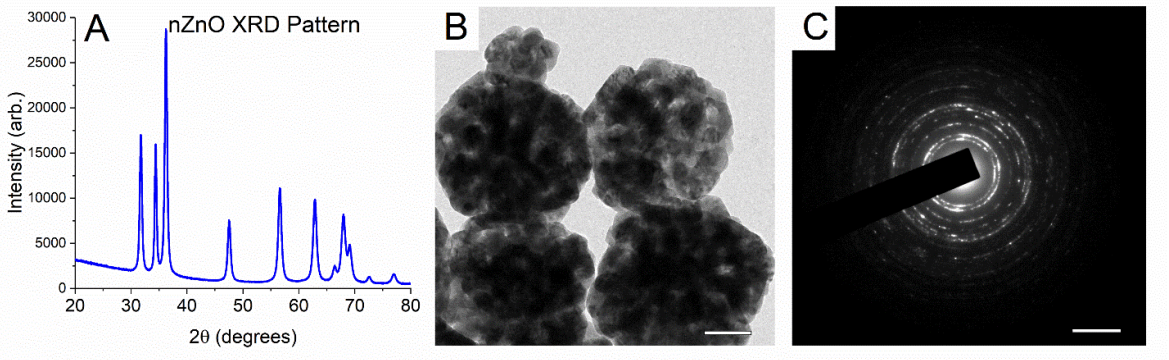


**Figure 5.8 (A) XRD pattern of the nZnO synthesized with calculated average crystal size of 15 nm. (B) TEM image of the aggregates composed of the smaller ZnO NP crystals (scale bar- 50 nm). (C) Electron diffraction pattern of the nZnO (scale bar 5/2 nm).**

Encapsulation, Imaging and Viability Assessments of Enc-nZnO.

Sonication of lipids above their transition temperature has been used to produce single bilayer lipid vesicles and is a common method employed for producing small liposomes.[31, 32] In order to encapsulate nZnO, we followed this same strategy but included the nZnO during the sonication procedure. To demonstrate good encapsulation of the nZnO, confocal microscopy was employed. As seen in Figure 5.2, the fluorescent signal from the lipid membrane stain overlays with the fluorescent nZnO, demonstrating good encapsulation of the nZnO. Dynamic light scattering measurements were subsequently performed on the encapsulated ZnO NPs (Enc-nZnO). Interestingly, a drastic decrease of the hydrodynamic size (HDS; Z-avg.; d.nm) was observed (739.5±15.5) when compared to the salt solution control and the size distribution is more similar to the free nZnO in nanopure water (Figure S5.2). This feature is attributed to the stabilization of the nZnO in the solution. We believe the hydrophilic surface of the lipid encapsulation helps prevent agglomeration of the nZnO, which is generally observed in higher ionic concentrations.[33] This stabilization was consistent over many months,

preventing the particles from agglomerating and allowing for the Enc-nZnO to be stored and used for subsequent experiments.

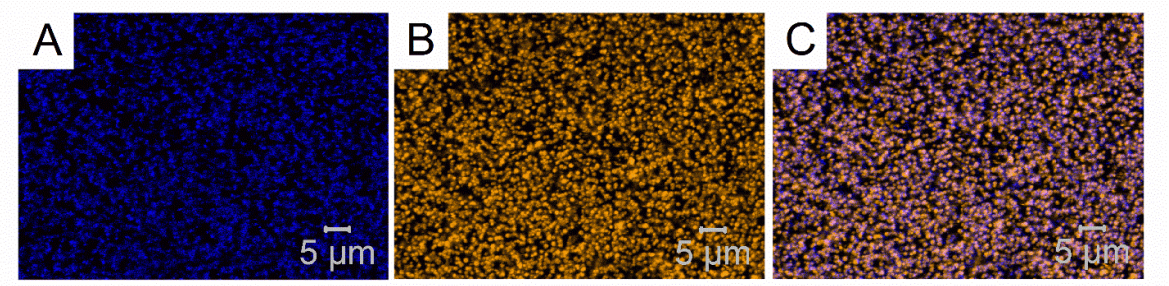


**Figure 5.2 Confocal microscopy image of the (A) fluorescent nZnO, excited by a 405 nm laser, (B) the lipid membrane stained with CellMask Orange, and (C) an overlay of A and B, demonstrating efficient encapsulation of the nZnO.**

To determine the impact encapsulating nZnO has on toxicity, both Jurkat T cell leukemia (suspension) and T47D breast cancer (adherent) cells were treated with Enc-nZnO for 48 hours. NPs sedimentation and, more specifically, the tendency for nZnO to agglomerate and become an unstable suspension in cellular media, has been shown to result in both decreased viability of adherent cells and increased viability of suspension cells.[34, 35] As our Enc-nZnO have a decreased HDS and the lipid coating prevents their agglomeration in salt solutions, their toxicity profile could conceivably be impacted and may increase the uptake of the NPs as seen in other reports.[36] However, the lipid encapsulation could also reduce interactions of the highly reactive surface of nZnO with cells or reduce/eliminate its dissolution in cellular media which could significantly affect nZnO interactions with cells and influence their toxicity.

As can be seen in Figure 5.3, coating nZnO with lipids effectively removes the toxicity for both Jurkat and T47D cancer cell types (No UV group: compare blue bars across the 3 panels). Treatments were conducted with concentrations up to 10 times the $IC_{50}$ of the bare nZnO samples (~12.2 µg/mL), and no appreciable toxicity was observed

with treatment as high as 122.21 μg/mL. Further studies demonstrated the ability to trigger the release of the Enc-nZnO using phototherapy by irradiation with a 365 nm LED UV lamp. Only a few minutes of UV exposure was required to effectively restore the toxic effects of the NPs to the cancer cells (Figure 5.3).

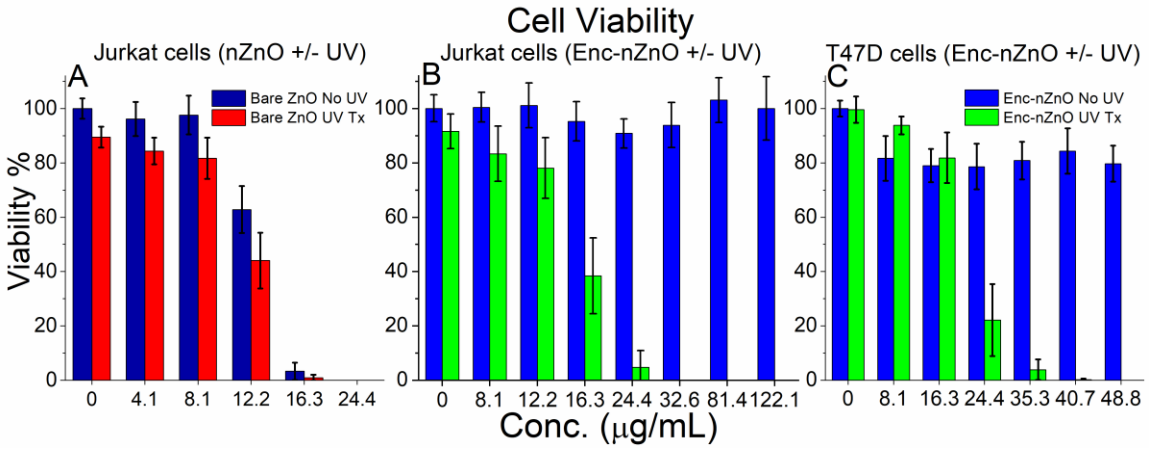


**Figure 5.3 Viability profiles of (A) Jurkat T cell leukemia treated with free nZnO (non-encapsulated), (B) Jurkat cells treated with Enc-nZnO and (C) T47D breast cancer cells treated with Enc-nZnO for 48 hours. (B & C) The non-UV groups (blue bars) show that the membrane encapsulation of nZnO protects the cells from the toxic effects of the NPs. The UV treatment groups (green bars) demonstrates that the toxic effects of nZnO are reestablished by the triggered release of the particles, most likely due to ROS generated from the nZnO and subsequent shedding of the lipid coating. UV exposure= 3 minutes for Jurkat T cells; 2 minutes for T47D cells.**

To further demonstrate both the protective nature of encapsulating nZnO and the re-establishment of the toxicity upon triggered release, confocal microscopy was utilized to image the T47D cells with Enc-nZnO after 24 hours of treatment. As can be seen in Figure 5.4 (middle row), even at concentrations of Enc-nZnO that are higher than those used in the T47D viability experiments (80.1 ug/mL; 1 mM), the lipid coating appears to protect the cells from the toxic effects of the nZnO. Even in areas with extremely high concentrations of Enc-nZnO associated with the exterior of the cells (middle row), the cell confluency is unaffected with little to no particles seen within the interior of the cell.

This is in stark contrast to photo-irradiated cells treated with relatively low concentrations of the Enc-nZnO (20.3 ug/mL; 250 μM; bottom row). In many of these cells, the morphology of the membrane changes and appears to be compromised. Additionally, the membrane stain doesn't overlay with the particles as it does in Figure 5.2 or in the high concentration Enc-nZnO /no UV treatment images (Figure 5.4, middle row). This observation suggests that the particles shed the lipid coating upon photo-irradiation. In addition, in localized areas of nZnO (bottom row), cell density is reduced and nZnO appear to have internalized into the cells. These results confirm the viability profiles and demonstrate the protective nature that the lipid coating has on the toxicity of nZnO.

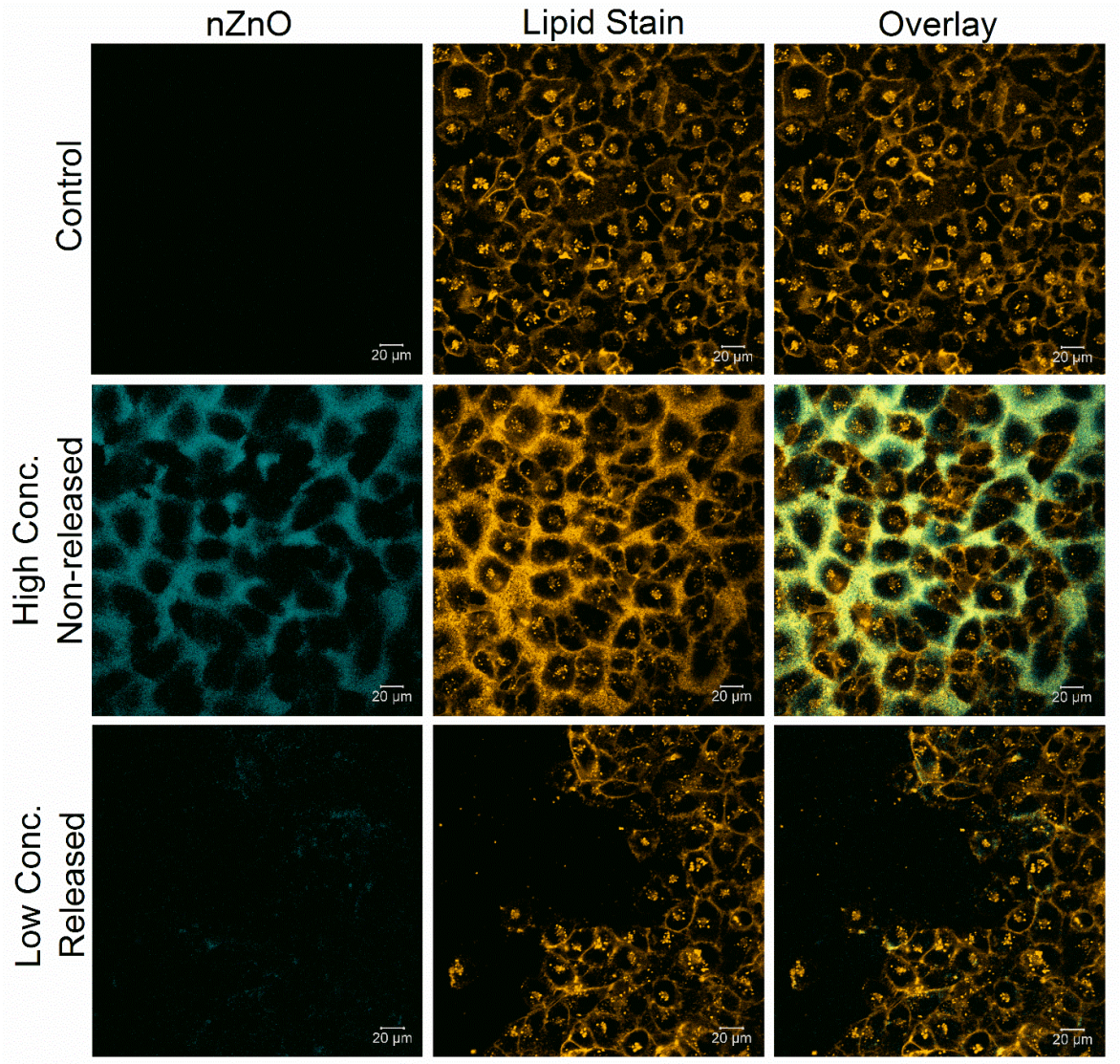


**Figure 5.4 Confocal images of T47D breast cancer cells after 48 hours of incubation in the imaging chambers and 24 hours post nZnO treatment. (Top Row) T47D cells incubated in the absence of nZnO (negative control) to show lack of auto-fluorescence from the cells in the nZnO channel. The lipid membrane stain, CellMask Orange was utilized to demonstrate the normal morphology of the cells (top-middle panel). (Middle Row) T47D cells treated with 81.4 µg/mL (1 mM) of the encapsulated nZnO (Enc-nZnO) 24 hours prior to imaging. These images demonstrate that even at relatively high concentrations of the Enc-nZnO, the cells morphology doesn't appear to be affected suggesting that the toxicity of the NPs is negligible. (Bottom Row) T47D cells treated with 20.3 µg/mL (250 µM) of Enc-nZnO and irradiated for 2 minutes shows changes in the confluency of the cells and an apparent loss of cell membrane integrity.**

Simulated and *In Vitro* Drug Release Experiments

Irradiation of nZnO with energy higher than the band gap of ZnO has been shown to generate ROS.[37] The ROS generating capabilities of nZnO have been proposed to be produced from excited electrons in the conduction band reacting with adsorbed $O_2$ molecules and locally adsorbed $OH^-$ interacting with valence band holes.[37] We hypothesized that irradiating the Enc-nZnO causes the nZnO to generate ROS which leads to rapid and propagating lipid peroxidation and subsequently releases both nZnO and any other cargo contained within the lipid carrier. To validate the triggered release upon photo-irradiation, the fluorescent dye 5(6)-carboxyfluoroscein (CF) was used as a hydrophilic drug model and co-encapsulated with the nZnO.

Fluorescent dyes are often used as a drug model by encapsulating high concentrations of the dye within liposomes. High concentrations of fluorescent dyes lead to a significant reduction of the fluorescent signal termed self-quenching. Upon release of the dye into the suspending solution, the fluorescence is restored and this feature has been extensively used as a model for drug loading. This approach allows for assessments of drug release kinetics and entrapment efficiency.[38-41] Using this model we demonstrated the effect that the lipid to nZnO ratio has on the release kinetics and premature drug release. As seen in Figure 5.5, lower lipid to nZnO ratios caused a much higher premature drug leakage (Figure 5.5A, No UV). However, the triggered release of the dye was drastically faster with low lipid to NP ratios (Figure 5.5B-C; 3:4 w/w) but the fluorescent signal may be impacted by the premature release. The higher ratios of lipid to nZnO almost entirely eliminated the premature release of the dye and reduced their release kinetics. However, after only about 1 hour post irradiation, nearly the same amount of

dye was released for the 5 minute exposure (Fig. 5.5 panel B), and nearly the same levels of release were obtained for the 15 minute UV exposure groups (panel C).

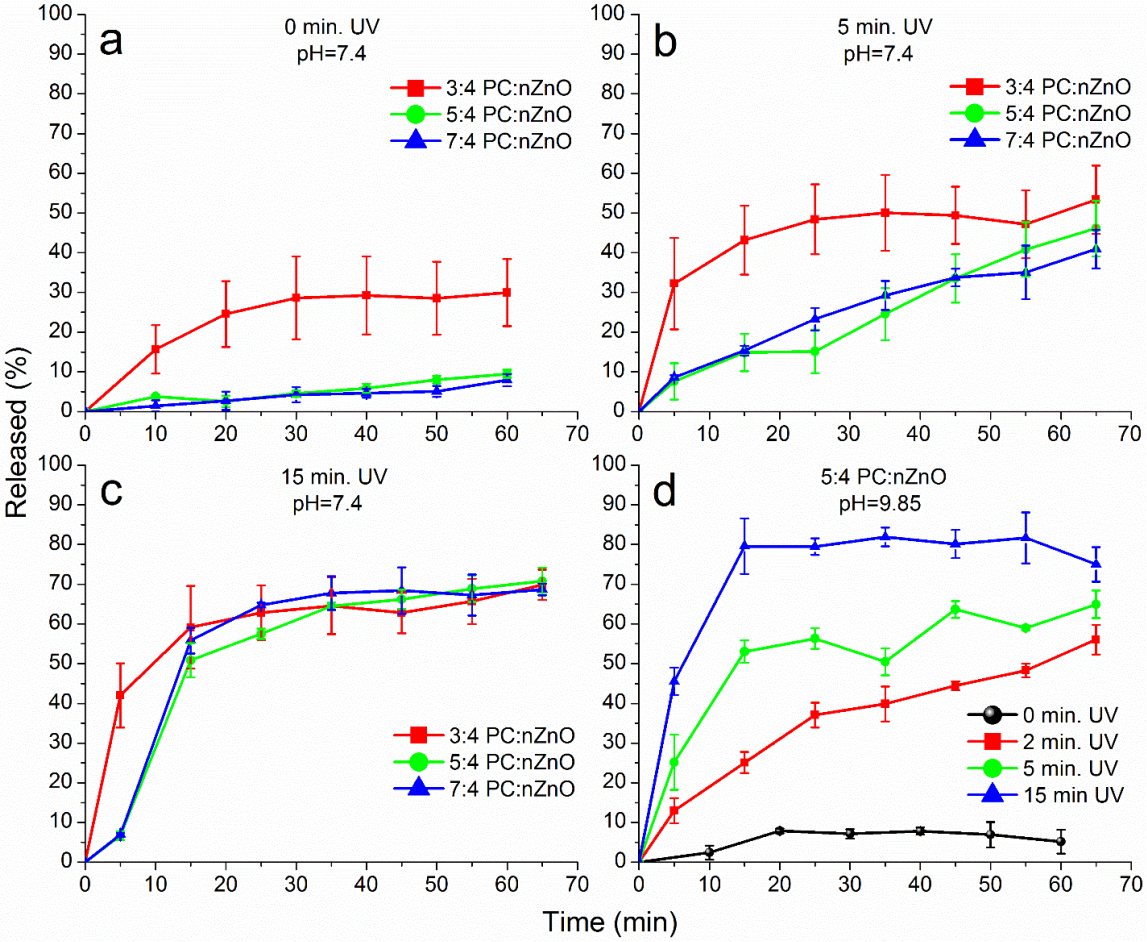


**Figure 5.5 (A-C) Release kinetics of encapsulated 5(6)-carboxyfluoroscein (pH=7.4) and nZnO with various lipid to nZnO ratios (w/w). (A) Non-triggered release (No UV) group, showing premature drug leakage from the different lipid to nZnO ratios. (B) Release kinetics after 5 minutes of UV exposure. (C) Release kinetics after 15 minutes of UV exposure. These release profiles demonstrate the majority of the contents can be rapidly released within 60 minutes and provides insights into the optimal lipid to NPs ratio. (D) nZnO encapsulated with a 5:4 lipid to NP ratio with an internal pH=9.85. The higher pH is believed to allow the nZnO to produce more ROS, thus allowing for a faster release of the dye with less irradiation time.**

To try to improve upon the release kinetics, experiments were performed using a higher pH (pH= 9.85) in the interior of the encapsulated nZnO/CF. The pH of the environment has been shown to impact the ROS generating capabilities of irradiated

nZnO.[37] With a high pH, more hydroxides are present and it is believed that the valence band holes left from the excited electron convert the locally adsorbed hydroxides to hydroxyl radicals. Since we believe that the ROS generated from the irradiated nZnO is responsible for the triggered release of the lipid coating, this strategy could increase the overall release kinetics. Figure 5.5D utilized the 5:4 PC to nZnO (w/w) ratio and the higher pH dramatically increased the release of the CF. Two minutes of UV exposure generated similar but faster release kinetics than the 5 minutes of UV exposure when using a pH of 7.4. Similarly, the release after 5 minutes of UV exposure was similar to that of the 15 minute groups using a lower pH and 15 minutes of exposure induced a faster and higher release than was achieved for any lipid to NP ratio previously.

Using CF as a drug model gave valuable insights into the release kinetics and how both the lipid to nZnO ratio and pH altered the release profiles. However, we sought to demonstrate the ability to co-encapsulate and release chemotherapy drugs using this system. Since the fluorescent dye was an excellent model for hydrophilic drugs, we chose to investigate the use of the hydrophobic drug Paclitaxel. Paclitaxel (PTX) is commonly used in the treatment of various cancers such as non-small cell lung cancer and breast cancer.[42, 43] Due to its high hydrophobicity, the most widely used formulation of PTX contains polyoxyethylated castor oil, which leads to numerous side effects including hypersensitivity reactions.[44, 45] This drawback has led to the development of new formulations that include protein and lipid-based nanocarriers. Since lipid peroxidation is proposed as the key to the triggered release mechanism in this system, the hydrophobic lipid tails would become much more soluble in aqueous environments once peroxidation occurs. This, in theory, would allow for a much faster release of PTX than in traditional

lipid carriers since the drug would not be bound by the hydrophobic environment found within the lipid bilayer. In pursuit of trying to develop a new carrier system and demonstrate that both classes of drugs can be loaded, we treated both the Jurkat and T47D cell lines with nZnO and Paclitaxel co-encapsulated (Enc-nZnO/PTX).

Figure 5.6 demonstrates that Paclitaxel and nZnO can be simultaneously delivered within the lipid carrier. In the non-triggered release viability experiments (blue), the Jurkat T cell viability profile was similar to the free PTX treatment (Figure 5.6A). While this is consistent with reports that demonstrate that lipid carriers for PTX have similar cellular viability profiles as using "free" PTX,[46, 47] the triggered release groups (green) showed a trend towards improvement in efficacy. Figure 5.6A used a higher ratio of nZnO to PTX. The drop in viability could be due to a combined PTX and nZnO effect at concentrations of nZnO that were previously shown to effect the viability of cells (>12.2 μg/mL; Figure 5.3). While simultaneous exposure to both nZnO and PTX could be beneficial in the treatment of cancer, we also wanted to assess the efficacy when only PTX effects are evident. To accomplish this, PTX was loaded with a lower nZnO to PTX ratio (Figure 5.6B) to mitigate direct toxicity effects from nZnO. Even with concentrations of nZnO that don't impact the viability of the cells, an increase in toxicity of the triggered release group was still achieved (Figure 5.6B). These findings demonstrate that the triggered release of PTX from the lipid carrier improves the efficacy of the drug (see Figure 5.6C for controls and comparison of the two ratios).

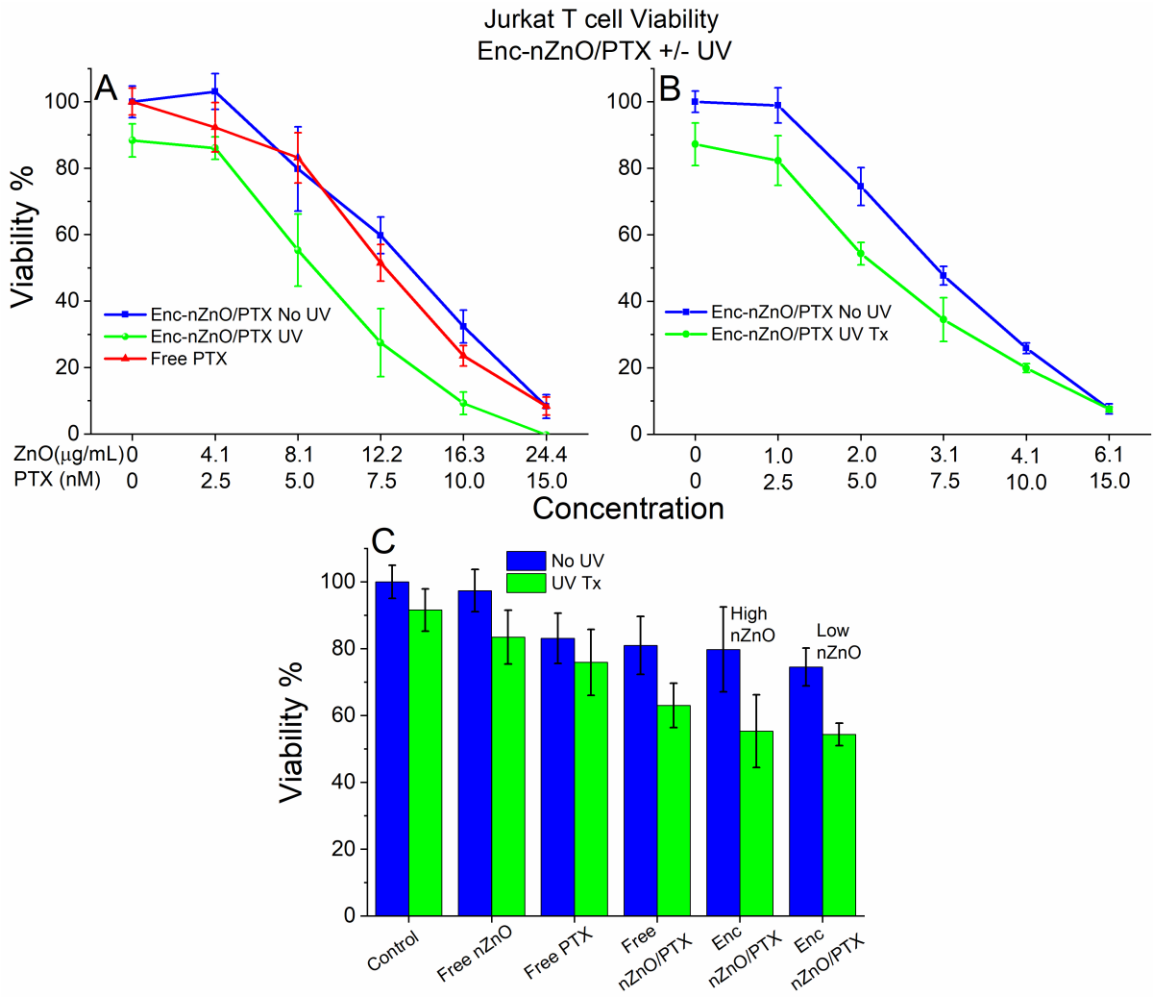


**Figure 5.6 Viability of Jurkat T cells after 48 hours of treatment with Paclitaxel (PTX) co-loaded with the Enc-nZnO (Enc-nZnO/PTX) and various controls. (A) The viability profile of the Jurkat cells when treated with free Paclitaxel and relatively higher nZnO to PTX ratios. Comparing the released (UV Tx) vs. the non-released (No UV) an increase in toxicity is noted for every concentration tested. (B) Relatively lower nZnO to PTX ratios were utilized to demonstrate that increased toxicity is still observed in the triggered release group at concentrations of nZnO that don't impact cell viability when used alone. (C) Treatments with the free drug PTX (5.0 nM), free nZnO (8.1 µg/mL) and free nZnO/PTX (8.1 µg/mL-5.0 nM) compared with the Enc-nZnO/PTX (High nZnO 8.1 µg/mL; Low nZnO 2.0 µg/mL; PTX 5.0 nM) with and without UV exposure.**

To validate these findings, experiments were repeated in another cell type. Surprisingly, T47D breast cancer cells demonstrated an even larger separation in viability than Jurkat cells (Figure 5.7). Interestingly, at or above the 40 nM PTX concentration,

there was an extreme difference in the viability of the T47D cells when comparing the UV vs. No UV groups. As this cell line behaved differently than the Jurkat cells, we sought out to explain why there was such a striking difference in the viability profiles. Our previous experiments with Enc-nZnO (no PTX; Figure 5.3C) showed no appreciable difference in toxicity between the control and the irradiated groups at concentrations of nZnO up to 16.3 μg/mL (200 μM). However, a ~40% difference was noted in the Enc-nZnO/PTX groups at this nZnO concentration (Figure 5.7A). It is possible that there could be enhanced effects from co-treatment with both nZnO and PTX. As seen with the controls in Figure 5.7B, the free nZnO had no effect on the viability profile, and the treatment with free 40 nM PTX had a somewhat similar effect as the non-triggered release Enc-nZnO/PTX group. Also, co-treatment with both the free nZnO and PTX had no appreciable increase in toxicity, when compared to the PTX treatment alone. Thus, we ruled out the possibility of additive or synergistic effects from nZnO and PTX at these concentrations.

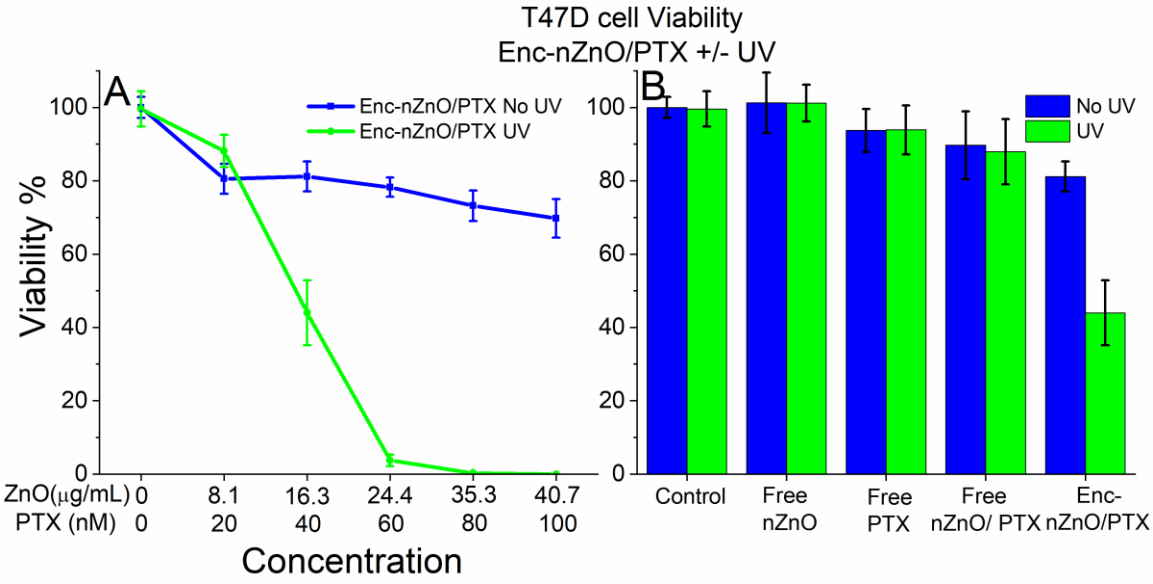


**Figure 5.7 Viability profile of T47D breast cancer cells after 48 hours of treatment of Enc-nZnO/PTX with and without UV irradiation. (A) The viability profile of the**

**triggered release group (green) vs. the non-irradiated group (blue) shows striking differences in toxicity. (B) Treatments with free nZnO (16.3 µg/mL), free PTX (40 nM) and free nZnO/PTX (16.3 µg/mL- 40 nM) compared to the Enc-nZnO/PTX (16.3 µg/mL- 40 nM). These controls demonstrate that at the 16.3 µg/mL concentration of nZnO, the NPs/PTX have no added or synergistic effects when the T47D cells are challenged with both the particles and PTX. Interestingly, a drastic improvement in the drug's efficacy is noted in the triggered release group, most likely due to localized release of the drug in the vicinity of the cells.**

Therefore, we believe this dramatic reduction in the viability is due to the fact that the T47D cell line is adherent whereas the Jurkat cells are a suspension cell line. The dispersion stability of the NPs most likely plays a role between these two cancer cell model systems. Previous reports on nZnO and other NPs have demonstrated that overtime the particles settle to the bottom of the culture wells, affecting the dosimetry which can impact cell viability.[34, 35] However, this alone cannot explain the differences in toxicity because the same nZnO were used in the control groups. Since the phototherapy was conducted 1.5 hours after the nZnO treatment, many of the particles likely settled to the bottom of the well before the irradiation occurred. Indeed, the confocal images of the Enc-nZnO treated T47D cells (Figure 5.4) demonstrate a high accumulation of the encapsulated NPs in the local vicinity of the cells, further strengthening this argument. When the PTX was rapidly released from the carrier due to photo-irradiation, this created a much higher local concentration of the free drug near the cells that, in turn, created a much higher cytotoxic response. These results also support the concept that the triggered release of the same overall drug concentration near cancer cells can improve the efficacy of the drug in the treatment of cancer.

## Discussion

Lipid encapsulation of nZnO is an effective approach to stabilize them in ionic solutions and effectively eliminate their toxicity. Using the inherent ability of nZnO to

induce ROS when irradiated and thus releasing them to reassert their toxic effects, to our knowledge, has never been demonstrated before. This strategy may further their potential to be used as a therapeutic and the ability to co-load both hydrophilic and hydrophobic drugs make this a promising delivery platform for the treatment of various diseases. The extreme differences noted in the viability profiles of the T47D breast cancers cells where surprising, yet offer much promise for this system to selectively target cancerous cells. While we showed how some factors, such as the lipid ratio and the pH can improve the release kinetics, other parameters may further enhance this approach.

The findings in this report utilizing UV to trigger the release of the liposomal contents may find value in photodynamic therapy (PDT) treatment options such as in the treatment of cancer.[48] Further, the cargo of the lipid carrier is not limited to only chemotherapeutic drugs, but could be used with drugs more traditionally used in PDT that cause cell sensitivity to phototherapy. This may increase the uptake of the drug to the targeted cells and reduce the patient's overall sensitivity to light that is often reported when treated with the free drug.[49] Although using UV light as a source to induce ROS generation from nZnO and induce the release of the cargo from the lipid carrier may be appropriate in instances like these, it may not be practical in clinical settings for the treatment of certain tumors found in deep tissue.

The depth penetration of UV light in tissue is in the high micrometer to low millimeter range and therefore wouldn't be able to penetrate large tumors. Many researchers have therefore sought ways to use near-infared (NIR) light as a trigger release mechanism as it has a higher depth penetration approaching the centimeter range.[50]

While this avenue could be more effective than UV light, NIR light still lacks the depth penetration needed for many tumors found in deep tissue areas.

Radiation therapy is extensively used in the treatment of tumors in all areas of the body and high precision machines are now able to specifically target tumors with relatively minimal radiation exposure to other tissues. Using X-ray or gamma rays as the triggering mechanism would be an ideal method for the triggered release of the encapsulated contents and may allow for simultaneous use of both radiation therapy and the chemotherapy that is not advisable in certain situations. This mode of treatment may also help combat drug resistant cells, as this would allow for simultaneous exposure of radiation, the chemotherapy drug and nZnO. Other researchers have demonstrated irradiating similar lanthanide doped nZnO with X-rays produces ROS, similar to UV irradiation of pure nZnO.[18] In addition to utilizing X-rays as a means to generate ROS from gadolinium doped nZnO, other researchers have demonstrated the ability to use these NPs as contrast agents for MRI and CT scans.[18, 51] Utilizing this new drug delivery system in combination with radiation therapy and potentially expanding its use for imaging purposes would create a novel theranostic platform that would allow for evaluations on tumor regression/progression during each therapy session.

In addition, reports have demonstrated with iron oxide NPs that the lipid carriers can improve its negative contrast in MRI imaging,[52] and may similarly improve the contrast capabilities in this system. Since we have already demonstrated that encapsulation of nZnO significantly reduces the toxicity of the NPs and with the recent concerns about side effects using traditional gadolinium-based contrast agents, this

system may potentially offer an alternative that has similar or improved imaging capabilities but reduces the possible side effects associated with traditional contrast dyes.

Other future work will look into using monoclonal antibodies or targeting ligands conjugated to the surface of the lipid carrier and could create a higher localized concentration of the encapsulated NPs and drugs while simultaneously further enhancing the contrast of the targeted tissue. Other encapsulating materials such as ROS sensitive polymers and various other lipid compositions will be evaluated to optimize this drug delivery platform. Since co-treatment with more than one chemotherapeutic drug is often utilized in the treatment of cancer, loading more than one drug into the carrier would be easily achievable and may provide a new way of co-administering multiple drugs. Using ultra-sound is another feasible means to trigger the release of the carrier, as sonoexcitation of nZnO has been shown to create ROS,[53] and could extend the use of this system to treat various diseases where irradiation may be a unadvisable. Lastly, other synthesis methods that produce different nZnO structures could further enhance this system, as hollow nZnO spheres have the capability of increasing the drug loading potential.[54] Collectively, there are many avenues to pursue using this technology and may extend its use to the treatment of various diseases beyond cancer.

## Conclusion

ZnO nanomaterials have received considerable attention due to many promising attributes and increasing applications in the treatment of diseases. This paper demonstrates a new approach to utilizing the ROS generating properties of nZnO and potentially other metal oxide NPs for drug delivery and possible imaging applications. The lack of apparent toxicity of the encapsulated nZnO and re-establishment of its anti-

cancer activity in the triggered release group is a step towards the goal of selectively treating cancer while preventing harm to normal cells. The extreme differences noted in the viability profiles of the T47D breast cancer cells treated with the co-encapsulated nZnO and Paclitaxel demonstrate the potential this system has for the co-delivery of multiple chemotherapeutics with on-demand release. Extending this system to utilizing X-rays to trigger the release is promising but much work is still required to optimize this platform before moving on to animal models and clinical studies. Many parameters such as the encapsulation composition, conjugation of ligands and making the particles stealth to the immune system are just of few of the key features that need to be addressed. However, with the foundation laid, the aim of utilizing this system for the treatment of various diseases and specifically cancer appears achievable.

**Supporting Information**

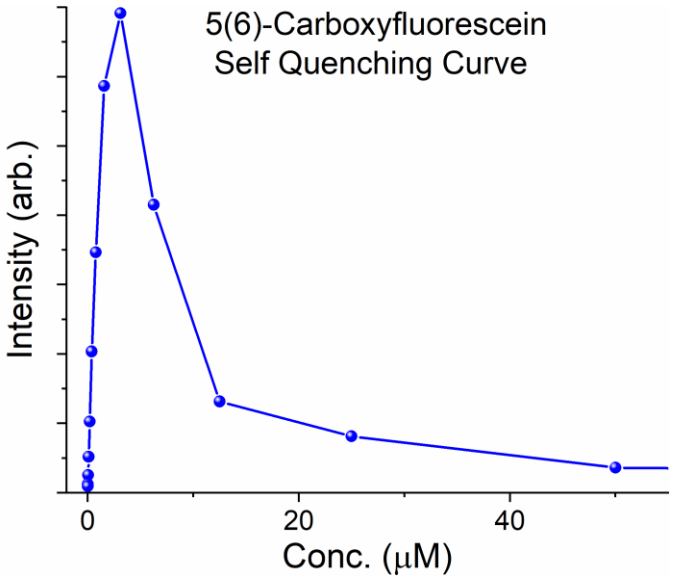


**Figure S5.1 Self quenching curve of 5(6)-Carboxyfluorescein in 130 mM NaCl. Concentrations below 1.5 μM show a linear increase in intensity vs. concentration. Working below this concentration allowed for evaluations on the release kinetics of the dye that was co-encapsulated with nZnO.**

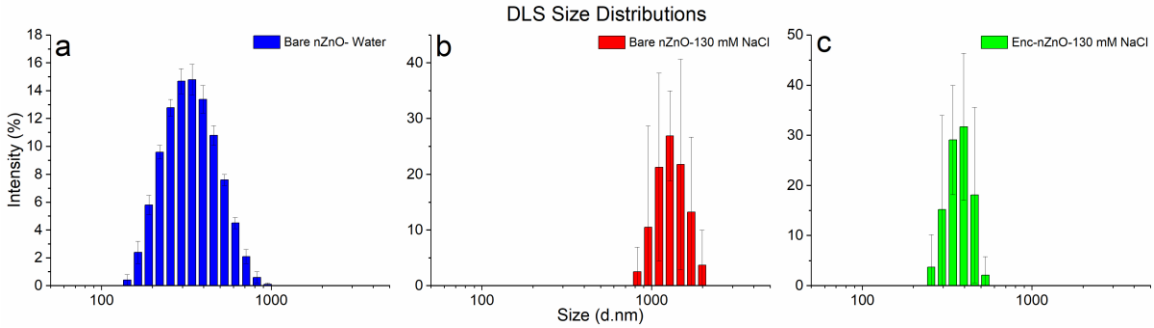


**Figure S5.2 NPs size distributions from DLS measurements. (a) Bare nZnO suspended in nanopore water. (b) Bare nZnO suspended in 130 mM NaCl. (c) Lipid encapsulated nZnO suspended in 130 mM NaCl. nZnO suspended in nanopore water shows a broad distribution between 100 and 1000 nm. In the salt solution the bare NPs agglomerate into much larger sizes in the micrometer range. Encapsulating the nZnO in lipids prevents the NPs from agglomerating into the large particles even in the 130 mM NaCl solution with their size distribution similar to that of bare nZnO in nanopore water.**

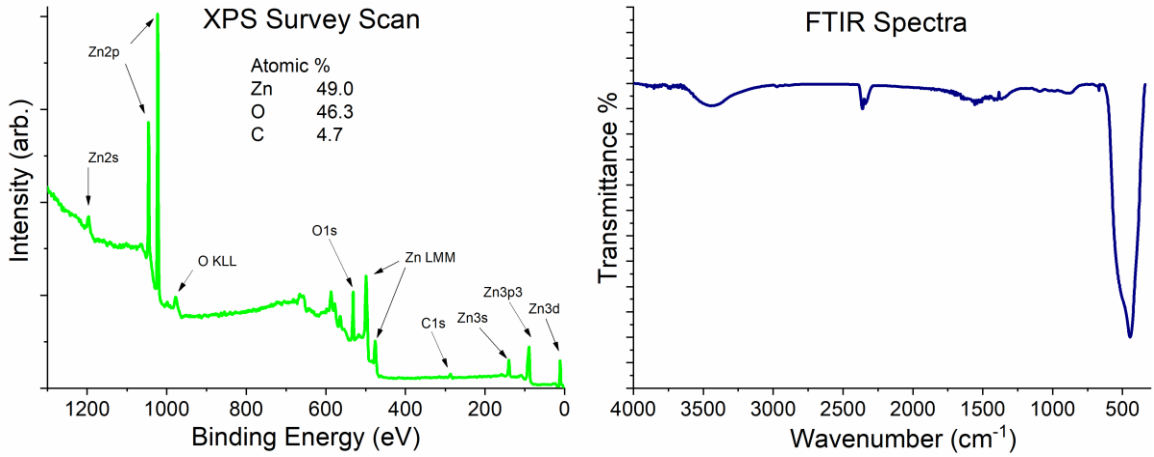


**Figure S5.3 XPS scan of the NPs before encapsulation showing no other elements besides zinc, oxygen and carbon are present. FTIR spectra confirms the sample purity seen with XPS measurements. The main peak near 500 $cm^{-1}$ is from the Zn-O modes. The other broad peak near 3400 $cm^{-1}$ is from O-H and the other minor peaks are attributed to carbon dioxide.**

## References

1. Bobo, D.; Robinson, K. J.; Islam, J.; Thurecht, K. J.; Corrie, S. R., Nanoparticle-Based Medicines: A Review of FDA-Approved Materials and Clinical Trials to Date. Pharmaceutical Research 2016, 33 (10), 2373-2387.

2. Martinez-Carmona, M.; Gun'ko, Y.; Vallet-Regi, M., ZnO Nanostructures for Drug Delivery and Theranostic Applications. *Nanomaterials* **2018,** *8* (4), 27.

3. Muharnmad, F.; Guo, M. Y.; Qi, W. X.; Sun, F. X.; Wang, A. F.; Guo, Y. J.; Zhu, G. S., pH-Triggered Controlled Drug Release from Mesoporous Silica Nanoparticles via Intracelluar Dissolution of ZnO Nanolids. Journal of the American Chemical Society 2011, 133 (23), 8778-8781.

4. Khan, M. M.; Adil, S. F.; Al-Mayouf, A., Metal oxides as photocatalysts. Journal of Saudi Chemical Society 2015, 19 (5), 462-464.

5. Djurisic, A. B.; Leung, Y. H.; Ng, A. M. C., Strategies for improving the efficiency of semiconductor metal oxide photocatalysis. Materials Horizons 2014, 1 (4), 400-410.

6. Li, J. Y.; Guo, D. D.; Wang, X. M.; Wang, H. P.; Jiang, H.; Chen, B. A., The Photodynamic Effect of Different Size ZnO Nanoparticles on Cancer Cell Proliferation In Vitro. Nanoscale Research Letters 2010, 5 (6), 1063-1071.

7. Zhang, H. J.; Shan, Y. F.; Dong, L. J., A Comparison of TiO2 and ZnO Nanoparticles as Photosensitizers in Photodynamic Therapy for Cancer. Journal of Biomedical Nanotechnology 2014, 10 (8), 1450-1457.

8. Leung, Y. H.; Xu, X. Y.; Ma, A. P. Y.; Liu, F. Z.; Ng, A. M. C.; Shen, Z. Y.; Gethings, L. A.; Guo, M. Y.; Djurisic, A. B.; Lee, P. K. H.; Lee, H. K.; Chan, W. K.; Leung, F. C. C., Toxicity of ZnO and TiO2 to Escherichia coli cells. Scientific Reports 2016, 6, 13.

9. Li, Y.; Niu, J. F.; Zhang, W.; Zhang, L. L.; Shang, E. X., Influence of Aqueous Media on the ROS-Mediated Toxicity of ZnO Nanoparticles toward Green Fluorescent

Protein-Expressing Escherichia coli under UV-365 Irradiation. Langmuir 2014, 30 (10), 2852-2862.

10. Xie, Y. P.; He, Y. P.; Irwin, P. L.; Jin, T.; Shi, X. M., Antibacterial Activity and Mechanism of Action of Zinc Oxide Nanoparticles against Campylobacter jejuni. Applied and Environmental Microbiology 2011, 77 (7), 2325-2331.

11. Mylonas, C.; Kouretas, D., Lipid peroxidation and tissue damage. In Vivo 1999, 13 (3), 295-309.

12. Premanathan, M.; Karthikeyan, K.; Jeyasubramanian, K.; Manivannan, G., Selective toxicity of ZnO nanoparticles toward Gram-positive bacteria and cancer cells by apoptosis through lipid peroxidation. Nanomedicine-Nanotechnology Biology and Medicine 2011, 7 (2), 184-192.

13. Rasmussen, J. W.; Martinez, E.; Louka, P.; Wingettt, D. G., Zinc oxide nanoparticles for selective destruction of tumor cells and potential for drug delivery applications. Expert Opinion on Drug Delivery 2010, 7 (9), 1063-1077.

14. Akhtar, M. J.; Ahamed, M.; Kumar, S.; Khan, M. A. M.; Ahmad, J.; Alrokayan, S. A., Zinc oxide nanoparticles selectively induce apoptosis in human cancer cells through reactive oxygen species. International Journal of Nanomedicine 2012, 7, 845-857.

15. Hanley, C.; Layne, J.; Punnoose, A.; Reddy, K. M.; Coombs, I.; Coombs, A.; Feris, K.; Wingett, D., Preferential killing of cancer cells and activated human T cells using ZnO nanoparticles. Nanotechnology 2008, 19 (29), 10.

16. Manshian, B. B.; Pokhrel, S.; Himmelreich, U.; Tamm, K.; Sikk, L.; Fernandez, A.; Rallo, R.; Tamm, T.; Madler, L.; Soenen, S. J., In Silico Design of Optimal Dissolution Kinetics of Fe-Doped ZnO Nanoparticles Results in Cancer-Specific Toxicity in a Preclinical Rodent Model. Advanced Healthcare Materials 2017, 6 (9), 11.

17. Ye, D. X.; Ma, Y. Y.; Zhao, W.; Cao, H. M.; Kong, J. L.; Xiong, H. M.; Mohwald, H., ZnO-Based Nanoplatforms for Labeling and Treatment of Mouse Tumors without Detectable Toxic Side Effects. Acs Nano 2016, 10 (4), 4294-4300.

18. Ghaemi, B.; Mashinchian, O.; Mousavi, T.; Karimi, R.; Kharrazi, S.; Amani, A., Harnessing the Cancer Radiation Therapy by Lanthanide-Doped Zinc Oxide Based Theranostic Nanoparticles. Acs Applied Materials & Interfaces 2016, 8 (5), 3123-3134.

19. Zhang, Y.; Nayak, T. R.; Hong, H.; Cai, W., Biomedical Applications of Zinc Oxide Nanomaterials. Current Molecular Medicine 2013, 13 (10), 1633-1645.

20. Sercombe, L.; Veerati, T.; Moheimani, F.; Wu, S. Y.; Sood, A. K.; Hua, S., Advances and Challenges of Liposome Assisted Drug Delivery. Frontiers in Pharmacology 2015, 6, 13.

21. Pattni, B. S.; Chupin, V. V.; Torchilin, V. P., New Developments in Liposomal Drug Delivery. Chemical Reviews 2015, 115 (19), 10938-10966.

22. Zylberberg, C.; Matosevic, S., Pharmaceutical liposomal drug delivery: a review of new delivery systems and a look at the regulatory landscape. Drug Delivery 2016, 23 (9), 3319-3329.

23. Noble, G. T.; Stefanick, J. F.; Ashley, J. D.; Kiziltepe, T.; Bilgicer, B., Ligand-targeted liposome design: challenges and fundamental considerations. Trends in Biotechnology 2014, 32 (1), 32-45.

24. Bertrand, N.; Wu, J.; Xu, X. Y.; Kamaly, N.; Farokhzad, O. C., Cancer nanotechnology: The impact of passive and active targeting in the era of modern cancer biology. Advanced Drug Delivery Reviews 2014, 66, 2-25.

25. Rosenblum, D.; Joshi, N.; Tao, W.; Karp, J. M.; Peer, D., Progress and challenges towards targeted delivery of cancer therapeutics. Nature Communications 2018, 9, 12.

26. Karanth, H.; Murthy, R. S. R., pH-sensitive liposomes - principle and application in cancer therapy. Journal of Pharmacy and Pharmacology 2007, 59 (4), 469-483.

27. Simoes, S.; Moreira, J. N.; Fonseca, C.; Duzgunes, N.; de Lima, M. C. P., On the formulation of pH-sensitive long circulation times. Advanced Drug Delivery Reviews 2004, 56 (7), 947-965.

28. Herrmann, R.; Garcia-Garcia, F. J.; Reller, A., Rapid degradation of zinc oxide nanoparticles by phosphate ions. Beilstein Journal of Nanotechnology 2014, 5, 2007-2015.

29. Lv, J. T.; Zhang, S. Z.; Luo, L.; Han, W.; Zhang, J.; Yang, K.; Christie, P., Dissolution and Microstructural Transformation of ZnO Nanoparticles under the Influence of Phosphate. Environmental Science & Technology 2012, 46 (13), 7215-7221.

30. Eixenberger, J. E.; Anders, C. B.; Hermann, R. J.; Brown, R. J.; Reddy, K. M.; Punnoose, A.; Wingett, D. G., Rapid Dissolution of ZnO Nanoparticles Induced by Biological Buffers Significantly Impacts Cytotoxicity. Chemical Research in Toxicology 2017, 30 (8), 1641-1651.

31. Akbarzadeh, A.; Rezaei-Sadabady, R.; Davaran, S.; Joo, S. W.; Zarghami, N.; Hanifehpour, Y.; Samiei, M.; Kouhi, M.; Nejati-Koshki, K., Liposome: classification, preparation, and applications. Nanoscale Research Letters 2013, 8, 9.

32. Patil, Y. P.; Jadhav, S., Novel methods for liposome preparation. Chemistry and Physics of Lipids 2014, 177, 8-18.

33. Bian, S. W.; Mudunkotuwa, I. A.; Rupasinghe, T.; Grassian, V. H., Aggregation and Dissolution of 4 nm ZnO Nanoparticles in Aqueous Environments: Influence of pH, Ionic Strength, Size, and Adsorption of Humic Acid. Langmuir 2011, 27 (10), 6059-6068.

34. Anders, C. B.; Chess, J. J.; Wingett, D. G.; Punnoose, A., Serum Proteins Enhance Dispersion Stability and Influence the Cytotoxicity and Dosimetry of ZnO Nanoparticles in Suspension and Adherent Cancer Cell Models. Nanoscale Research Letters 2015, 10, 22.

35. Cho, E. C.; Zhang, Q.; Xia, Y. N., The effect of sedimentation and diffusion on cellular uptake of gold nanoparticles. Nature Nanotechnology 2011, 6 (6), 385-391.

36. Dumontel, B.; Canta, M.; Engelke, H.; Chiodoni, A.; Racca, L.; Ancona, A.; Limongi, T.; Canavese, G.; Cauda, V., Enhanced biostability and cellular uptake of zinc oxide nanocrystals shielded with a phospholipid bilayer. *Journal of Materials Chemistry B* **2017,** *5* (44), 8799-8813.

37. Yang, Q. B.; Lin, T. S.; Burton, C.; Park, S. H.; Ma, Y. F., Physicochemical insights of irradiation-enhanced hydroxyl radical generation from ZnO nanoparticles. Toxicology Research 2016, 5 (2), 482-491.

38. Amstad, E.; Kohlbrecher, J.; Muller, E.; Schweizer, T.; Textor, M.; Reimhult, E., Triggered Release from Liposomes through Magnetic Actuation of Iron Oxide Nanoparticle Containing Membranes. Nano Letters 2011, 11 (4), 1664-1670.

39. Huang, S. L.; MacDonald, R. C., Acoustically active liposomes for drug encapsulation and ultrasound-triggered release. Biochimica Et Biophysica Acta-Biomembranes 2004, 1665 (1-2), 134-141.

40. Huang, H. L.; Lu, P. H.; Yang, H. C.; Lee, G. D.; Li, H. R.; Liao, K. C., Fiber-optic triggered release of liposome in vivo: implication of personalized chemotherapy. International Journal of Nanomedicine 2015, 10, 5171-5185.

41. Hegh, D. Y.; Mackay, S. M.; Tan, E. W., CO2-triggered release from switchable surfactant impregnated liposomes. Rsc Advances 2014, 4 (60), 31771-31774.

42. Sandler, A.; Gray, R.; Perry, M. C.; Brahmer, J.; Schiller, J. H.; Dowlati, A.; Lilenbaum, R.; Johnson, D. H., Paclitaxel-carboplatin alone or with bevacizumab for non-small-cell lung cancer. New England Journal of Medicine 2006, 355 (24), 2542-2550.

43. Miller, K.; Wang, M. L.; Gralow, J.; Dickler, M.; Cobleigh, M.; Perez, E. A.; Shenkier, T.; Cella, D.; Davidson, N. E., Paclitaxel plus bevacizumab versus paclitaxel alone for metastatic breast cancer. New England Journal of Medicine 2007, 357 (26), 2666-2676.

44. Koudelka, S.; Turanek, J., Liposomal paclitaxel formulations. Journal of Controlled Release 2012, 163 (3), 322-334.

45. Ma, P.; Mumper, R. J., Paclitaxel Nano-Delivery Systems: A Comprehensive Review. Journal of Nanomedicine & Nanotechnology 2013, 4 (2), 16.

46. Yang, T.; Cui, F. D.; Choi, M. K.; Lin, H. X.; Chung, S. J.; Shim, C. K.; Kim, D. D., Liposome formulation of paclitaxel with enhanced solubility and stability. Drug Delivery 2007, 14 (5), 301-308.

47. Hong, S. S.; Choi, J. Y.; Kim, J. O.; Lee, M. K.; Kim, S. H.; Lim, S. J., Development of paclitaxel-loaded liposomal nanocarrier stabilized by triglyceride incorporation. International Journal of Nanomedicine 2016, 11, 4465-4477.

48. Dolmans, D.; Fukumura, D.; Jain, R. K., Photodynamic therapy for cancer. Nature Reviews Cancer 2003, 3 (5), 380-387.

49. Vrouenraets, M. B.; Visser, G. W. M.; Snow, G. B.; van Dongen, G., Basic principles, applications in oncology and improved selectivity of photodynamic therapy. Anticancer Research 2003, 23 (1B), 505-522.

50. Ruggiero, E.; Alonso-de Castro, S.; Habtemariam, A.; Salassa, L., Upconverting nanoparticles for the near infrared photoactivation of transition metal complexes: new opportunities and challenges in medicinal inorganic photochemistry. Dalton Transactions 2016, 45 (33), 13012-13020.

51. Liu, Y. L.; Ai, K. L.; Yuan, Q. H.; Lu, L. H., Fluorescence-enhanced gadolinium-doped zinc oxide quantum dots for magnetic resonance and fluorescence imaging. Biomaterials 2011, 32 (4), 1185-1192.

52. Martinez-Gonzalez, R.; Estelrich, J.; Busquets, M. A., Liposomes Loaded with Hydrophobic Iron Oxide Nanoparticles: Suitable T-2 Contrast Agents for MRI. International Journal of Molecular Sciences 2016, 17 (8), 14.

53. Jyothi, K. P.; Yesodharan, S.; Yesodharan, E. P., Ultrasound (US), Ultraviolet light (UV) and combination (US plus UV) assisted semiconductor catalysed degradation of organic pollutants in water: Oscillation in the concentration of hydrogen peroxide formed in situ. Ultrasonics Sonochemistry 2014, 21 (5), 1787-1796.

54. Puvvada, N.; Rajput, S.; Kumar, B. N. P.; Sarkar, S.; Konar, S.; Brunt, K. R.; Rao, R. R.; Mazumdar, A.; Das, S. K.; Basu, R.; Fisher, P. B.; Mandal, M.; Pathak, A., Novel ZnO hollow-nanocarriers containing paclitaxel targeting folate-receptors in a malignant pH-microenvironment for effective monitoring and promoting breast tumor regression. Scientific Reports 2015, 5, 15.

# CHAPTER SIX: CONCLUSION

The low cost of production and vast array of potential uses for nZnO make them a promising material in the field of nanobiotechnology. Specifically, their use as a potential therapeutic and diagnostic tool offer much hope as a new nanomedicine. To be able to fully exploit their use, their mechanism of toxicity and how various properties modulate their interactions with cells needs to be clearly understood. This dissertation explored various factors that contribute to the toxicity of nZnO and how their physical properties can be harnessed for their use in imaging and as a therapeutic.

The discovery that biological buffers induce the rapid dissolution of nZnO may help in elucidating the toxicity mechanism of nZnO by eliminating artifacts associated with their use. Additionally, understanding how the use of these buffers impact their transformation into different chemical species and complex precipitants provided a clearer picture of how they behave in various toxicological studies. These results highlight the need for researchers to clearly identify the use of these buffers in their experiments and consider how their inclusion my impact conclusions when performing evaluations on nZnO toxicity.

Use of the pore-forming toxin lysenin demonstrated that using a simplified model system for voltage-gate ion channels is an excellent tool for investigating how nZnO may interact with protein channels and subsequently alter their functionality. The findings that nZnO can significantly inhibit the conductance of lysenin channels suggests that electrostatic interactions between nZnO and transmembrane transporters may impact the

transporters functionality, thus contribute to the toxicity of nZnO. While this finding might be considered another factor that could impede the use of nZnO, these results may find use in nanomedicine and drug delivery applications to regulate the gating of specific ion channels.

The ability to control certain defect states in nZnO was an exciting achievement as it altered the physical properties of the nanoparticles, creating a narrow visible emission and lowered the band gap of the material. These features made it possible to use common fluorescent imaging instruments, such as a confocal microscope, to perform live-cell imaging experiments. These new nZnO provide a new way to track the NPs interactions with cells in real-time as well as potentially develop into a new alternative bio-label. Additional experiments utilizing these nZnO have the potential to help decipher the complex interplay of nZnO with various cell types and expand their use in other nanobiotechnology applications.

The final investigation into using the ROS generating properties of nZnO in a new drug delivery platform showed tremendous potential. The nearly complete elimination of the nZnO toxicity through encapsulation demonstrated a simplistic way to potentially eliminate any off-target effects from nZnO if used as a therapeutic. The additional ability to trigger the release of the nanoparticles and drugs offers the promise to create a site specific and on-demand targeting system for the treatment of various diseases. The dramatic decrease in the viability of the breast cancer cells in the triggered release group exemplified the concept that releasing the payload near cancerous tissue can significantly improve the efficacy of the drug in the treatment of cancer.

Collectively, the different investigations in this dissertation improved the understanding of nZnO toxicity and offer new ways to use different properties of nZnO in biological applications. Further work is required to fully exploit these new findings, but the foundations laid here provide the basis for their use in novel ways. Continued improvement on these new technologies may extend these systems into in vivo experiments, clinical trials and hopefully into a therapeutic.

# APPENDIX

## Copyright Permissions

Rapid Dissolution of ZnO Nanoparticles Induced by Biological Buffers Significantly Impacts Cytotoxicity

Copyright permission for published and submitted material from theses and dissertations: ACS extends blanket permission to students to include in their theses and dissertations their own articles, or portions thereof, that have been published in ACS journals or submitted to ACS journals for publication, provided that the ACS copyright credit line is noted on the appropriate page(s).

ZnO Nanoparticles Modulate the Ionic Transport and Voltage Regulation of Lysenin Nanochannels

**Open Access Articles**

The open access articles published in BMC's journals are made available under the Creative Commons Attribution (CC-BY) license, which means they are accessible online without any restrictions and can be re-used in any way, subject only to proper attribution (which, in an academic context, usually means citation.

Controlled Defect Engineering of ZnO Nanoparticles Modulates Properties for Potential Bio-Imaging and Optoelectronic Applications

Wiley Article Sharing Policy: Submitted Version (the author's version that has not been peer-reviewed, nor had any value added to it by Wiley, such as formatting or copy editing):

Authors may post their submitted manuscript at any time on their personal website, in their company or institutional repository, in not-for-profit subject-based preprint servers or repositories, and on SCNs which have signed up to the STM sharing principles. Authors may wish to add a note about acceptance by the journal and upon publication it is recommended that authors add a Digital Object Identifier (DOI) link back to the final article so that users with access to Wiley Online Library may access the final version of record and make use of the fully networked research environment. The deposited version may not be updated to look like the final version of record. While this is the copyright policy, individual journals may operate different editorial policies with respect to preprints and authors should consult the relevant author guidelines.